

# **Ultra-high energy neutrino simulations**

Front cover: Inspired by Rabelais, Henri Colnard.

Back cover: Detail of a violin in faience, Henri Colnard, Martres Tolosane ©1995.

# Ultra-high energy neutrino simulations

ACADEMISCH PROEFSCHRIFT

TER VERKRIJGING VAN DE GRAAD VAN DOCTOR  
AAN DE UNIVERSITEIT VAN AMSTERDAM  
OP GEZAG VAN DE RECTOR MAGNIFICUS  
PROF. DR. D. C. VAN DEN BOOM  
TEN OVERSTAAN VAN EEN DOOR HET COLLEGE VOOR PROMOTIES  
INGESTELDE COMMISSIE, IN HET OPENBAAR TE VERDEDIGEN  
IN DE AGNIETENKAPEL  
OP DONDERDAG 16 APRIL 2009, TE 10:00 UUR

door

Claudine Marie Marguerite Colnard

geboren te Saint-Gaudens, Frankrijk

Promotor: Prof. Dr. G. van der Steenhoven  
Co-promotor: Dr. E. de Wolf

Faculteit der Natuurwetenschappen, Wiskunde en Informatica



*A mes parents*

A philosopher once asked, "Are we human because we gaze at the stars, or do we gaze at them because we are human?" Pointless, really... "Do the stars gaze back?" Now that's a question.

– Neil Gaiman,  
*Stardust*, 1999.



# Contents

<b>Introduction</b>	<b>1</b>
0.1 Very high energy Cosmic Rays . . . . .	2
0.2 The Greisen-Zatsepin-Kuz'min limit . . . . .	5
0.3 Active galactic nuclei . . . . .	7
0.4 Discussion . . . . .	8
<b>1 The ANTARES telescope</b>	<b>11</b>
1.1 Neutrino detection principle . . . . .	13
1.2 Background signal . . . . .	15
1.3 Detector layout . . . . .	15
1.3.1 Detection lines . . . . .	16
1.3.2 Electronics containers . . . . .	17
1.3.3 Optical modules . . . . .	18
1.3.4 Sea monitoring instrumentation . . . . .	20
1.4 Development and Construction . . . . .	21
1.4.1 Demonstrator Line . . . . .	21
1.4.2 Prototype Sector Line and Mini Instrumentation Line . . . . .	21
1.4.3 Line Zero . . . . .	24
1.4.4 MILOM . . . . .	24
1.4.5 The complete telescope . . . . .	26
<b>2 The ANTARES data acquisition system</b>	<b>29</b>
2.1 Data Acquisition . . . . .	30
2.1.1 Readout of the data . . . . .	30
2.1.2 The ANTARES Trigger . . . . .	31
2.1.3 Data format . . . . .	33
2.1.4 The Clock System . . . . .	33
2.2 Relative time calibration . . . . .	34
2.2.1 The optical beacon system . . . . .	34
2.2.2 Relative time calibration of the MILOM . . . . .	35
2.2.3 The ARS TVC calibration . . . . .	35
2.3 The Data Quality Monitoring System . . . . .	38
2.3.1 Software Modules . . . . .	39

## CONTENTS

2.3.2	The Kolmogorov-Smirnov test . . . . .	41
<b>3</b>	<b>Neutrino event generators</b>	<b>45</b>
3.1	Event Generators and Propagators . . . . .	46
3.1.1	Neutrino Generators . . . . .	46
3.1.2	Lepton propagators . . . . .	51
3.2	GENHEN . . . . .	52
3.2.1	Program summary . . . . .	52
3.2.2	Generation method . . . . .	54
3.2.3	Lepton propagator . . . . .	59
3.3	ANIS: All Neutrino Interaction Simulation . . . . .	59
3.3.1	Program summary . . . . .	60
3.3.2	Generation method . . . . .	61
3.3.3	The Muon Propagator MMC . . . . .	65
3.4	Comparison between ANIS and GENHEN . . . . .	66
3.4.1	General differences . . . . .	66
3.4.2	CPU time Comparison . . . . .	69
3.4.3	Event rate comparison . . . . .	70
<b>4</b>	<b>Detector simulation and Track reconstruction</b>	<b>73</b>
4.1	SIRENE . . . . .	74
4.1.1	Tracking secondary particles . . . . .	74
4.1.2	Photon field simulation . . . . .	78
4.2	Signal digitisation and triggering . . . . .	90
4.3	Comparison with the ANTARES detector simulations . . . . .	92
4.3.1	KM3 and GEASIM . . . . .	92
4.3.2	Simulation results . . . . .	93
4.4	Reconstruction . . . . .	95
4.4.1	Probability Density Functions . . . . .	96
4.4.2	Linear least square methods . . . . .	97
4.4.3	Track reconstruction with AartStrategy . . . . .	98
4.4.4	Track reconstruction with ScanFit . . . . .	100
4.4.5	Energy Reconstruction . . . . .	101
4.4.6	Performance of the Reconstruction algorithms . . . . .	101
4.5	Future extentions . . . . .	107
<b>5</b>	<b>High Energy Simulations Results</b>	<b>109</b>
5.1	Monte Carlo simulations . . . . .	110
5.1.1	Ultra high energy neutrino simulation . . . . .	110
5.1.2	Atmospheric muon background simulation . . . . .	112
5.2	Data selection and analysis . . . . .	113
5.2.1	Track energy estimate . . . . .	114
5.2.2	Uncorrelated background and triggering . . . . .	116

## CONTENTS

5.2.3	First event selection . . . . .	117
5.2.4	Expected rates and neutrino flux limit . . . . .	118
5.2.5	Model rejection potential . . . . .	122
5.2.6	Average flux upper limits . . . . .	127
5.2.7	Comparison with existing bounds . . . . .	127
5.2.8	Effective detector area . . . . .	129
5.3	Discussion . . . . .	131
<b>Summary and conclusions</b>		<b>133</b>
<b>A Implementation of ANTARES in ANIS</b>		<b>139</b>
<b>B Implementation of ANTARES in MMC</b>		<b>141</b>
<b>C SIRENE software implementation</b>		<b>145</b>
C.0.1	Classes to build the geometry of a telescope . . . . .	145
C.0.2	Classes for the tracking of the particles . . . . .	147
C.0.3	Classes to model the scattering of the particles . . . . .	148
<b>Acknowledgements</b>		<b>151</b>
<b>List of figures</b>		<b>153</b>
<b>List of tables</b>		<b>157</b>
<b>Bibliography</b>		<b>159</b>



# Introduction



stronomy, with several thousand years of history, is one of the oldest of the natural sciences, its roots dating back to antiquity. For all time, mankind has been gazing at the sky, seeking answers to nature's mysteries. While early astronomers watched the regular movements of visible celestial objects with just the naked eye, Galileo could observe the craters on the Moon and even the explosion of a supernova using one of the first built telescopes at the beginning of the 16<sup>th</sup> century. Since this period, astronomy has continued its evolution over time and remarkable

progress has been made thanks to a continuous dialogue between theory and observations. Nowadays, most of our knowledge of the Universe comes from the observation of photons. Beside their stability and electrical neutrality, photons are easy to detect and their spectrum contains detailed information about the chemical and physical properties of their source. Moreover, they are abundantly produced in the Universe as electromagnetic radiation is released in a variety of physical processes and thus constitute a crucial cosmic information carrier. The recent advent of multi-wavelengths telescopes allows the observation of the entire electromagnetic spectrum, with wavelengths well beyond the limited range of visible light used in the past. However, the ultra high energy domain, with energies far beyond the limits set by present day particle accelerators remains largely unexplored by conventional astronomical methods.

Even though gamma ray astronomy has been successful, observations are limited by attenuation of high energy photons from distant sources due to electron-positron pair production in interactions with the omnipresent 2.7 K cosmic microwave radiation [1]

$$\gamma + \gamma_{CMB} \rightarrow e^+ + e^- .$$

As a result, the Universe is opaque to gamma rays from extragalactic sources and photons with energies in excess of  $10^6$  GeV cannot even survive the journey from the Galactic Center to the Earth [2]. In addition, gamma rays cannot penetrate nor escape the hot and dense regions which form the core of stars and other high energy astrophysical sources. It is therefore impossible to investigate the proper-

## CONTENTS

ties of these objects or regions of the Universe by direct observations. In the last decades, a new field of research has emerged to overcome these limitations.

At a crossroad between astronomy, particle physics and cosmology, astroparticle physics studies elementary particles of cosmic origin. Through the design and construction of new types of infrastructure such as underground laboratories or especially designed telescopes, antennas and satellites, astroparticle physics opens a new window on the Universe, searching not only for photons from astrophysical objects, but also for high energy cosmic rays, neutrinos and gravitational waves.

Neutrinos are of particular interest as they are stable particles which interact very weakly with matter. They can cross long distances and penetrate regions which are opaque to photons. Neutrinos are electrically neutral and their trajectory cannot be deflected by the ambient magnetic fields in the Universe. Consequently, the direction of the observed neutrinos at Earth points back directly to their source. Thanks to their particular characteristics, neutrinos constitute an ideal high energy probe to observe distant astrophysical objects and provide information on the dynamics of the most energetic phenomena of the Universe. The study of the detectability of very high energy cosmic neutrinos is the central topic of this thesis. Such neutrinos are expected to be produced in the interactions of high energy cosmic rays with ambient matter and/or photons [2]. Models of cosmic ray production are therefore presented in Section 0.1. The shape of the observed cosmic ray energy spectrum is also discussed. The problem of the Greisen-Zatsepin-Kuz'min limit and its consequences on the possible observation of ultra high energy cosmic rays is described in Section 0.2. The most likely sources of very high energy neutrinos, active galactic nuclei (AGN) are discussed in Section 0.3. Finally, the main questions addressed by this thesis are outlined in Section 0.4.

### 0.1 Very high energy Cosmic Rays

Cosmic rays are atomic nuclei, predominantly protons and electrons which bombard the Earth from beyond the atmosphere with very high energies. The lowest energy cosmic rays are detected directly by experiments on board of satellites or high altitude balloons before they are absorbed in the atmosphere. High energy cosmic rays however are detected indirectly through the extensive air showers they produce which can be observed by an array of particle detectors at ground level. The measured cosmic ray spectrum is shown in Figure 1. As can be seen in the figure, the spectrum steepens at an energy of about  $3 \times 10^{15}$  eV which is referred to as the “knee”, and flattens near  $3 \times 10^{18}$  eV at the “ankle”. The flux of cosmic rays is well described by a broken power law of the form  $\phi(E) \propto E^{-\gamma}$ ,



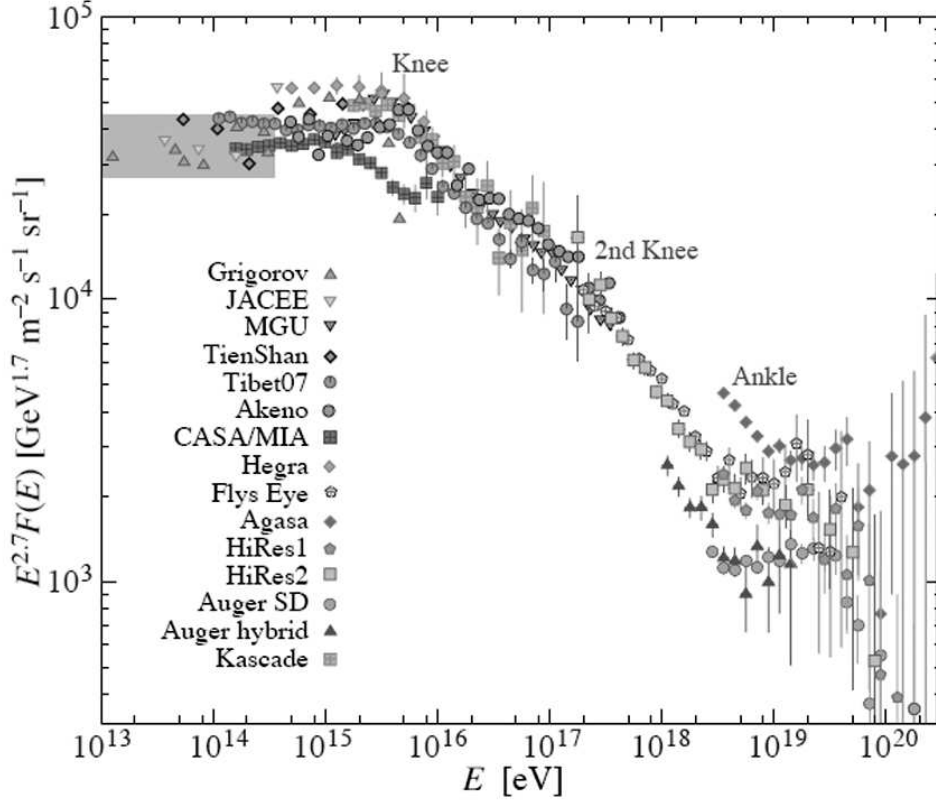


Figure 1: The measured cosmic ray spectrum between  $10^{13}$  and  $10^{21}$  eV. The shaded area shows the range of direct cosmic ray spectrum measurements [3].

with an energy dependent spectral index  $\gamma$  such that

$$\gamma \simeq \begin{cases} 2.7 & \text{if } E \leq 3 \times 10^{15} \text{ eV} \\ 3.0 & \text{if } 10^{15} \text{ eV} \leq E \leq 10^{19} \text{ eV} \\ 2.7 & \text{if } E \geq 10^{19} \text{ eV.} \end{cases}$$

The shape of the measured spectrum constraints possible models of cosmic ray production. It is usually assumed that cosmic rays are produced and accelerated by sources both within and outside the Galaxy. The acceleration mechanism is based on initial suggestions by Enrico Fermi [4]. First order Fermi acceleration, or diffusive shock acceleration occurs when cosmic ray particles are repeatedly reflected by fast-moving magnetic fields in the interstellar medium. By bouncing back and forth in the magnetic field randomly lets some of the cosmic ray particles gain energy. The maximum energy they can possibly obtain depends on the charge of the particle, the shock velocity, the magnetic field at the site and the size of the accelerating source. This is known as the Hillas criterion [5] which is illustrated in figure 2 where acceleration limits for possible high energy cosmic ray sources are shown. Astrophysical objects which can accelerate protons above

## CONTENTS

$10^{20}$  eV are displayed on the top right corner, above the dotted line. The two solid lines represent the proton energies above  $10^{21}$  eV (above) and iron nuclei <sup>1</sup> with energies above  $10^{20}$  eV (below). As can be seen in the figure, only a few objects

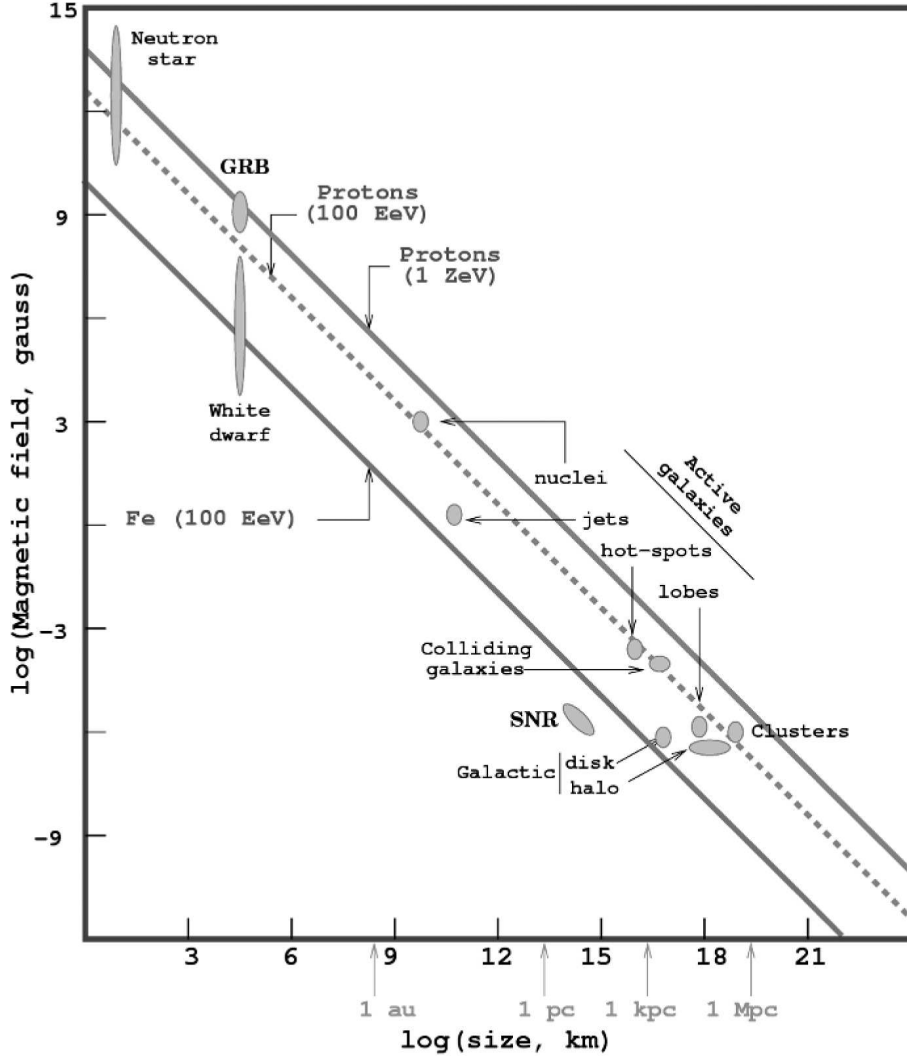


Figure 2: A Hillas plot [5]. The strength of the electromagnetic field is shown as a function of the size of the object in which protons and nuclei are accelerated to become high energy cosmic rays. Objects above the dotted line are able to accelerate protons above  $10^{20}$  eV, assuming an efficient diffuse shock acceleration mechanism.

are able to accelerate cosmic rays up to the highest energies. This is discussed below.

Cosmic rays with energies below the knee are thought to originate inside the Galaxy, most probably from acceleration in the shock waves of supernovae rem-

<sup>1</sup>Iron nuclei are the heaviest abundant nuclei observed in cosmic rays

nants [3]. The knee could thus feature the highest energy that galactic accelerators can reach. Cosmic rays with energies above the knee cannot be confined by the magnetic fields within the Galaxy. They are thus believed to propagate through intergalactic space [6] what induces a steepening in the cosmic ray energy spectrum. In the region around the ankle, the galactic population of cosmic rays is overcome by the extragalactic population of cosmic rays [3]. The ankle is consequently considered to reflect the transition from galactic to extragalactic cosmic rays. Above the ankle, cosmic rays are difficult to detect since they hit the Earth at a rate of less than one per square kilometer per century. Experimental evidence suggests that such high energy cosmic rays are mostly protons accelerated in extragalactic sources [7]. Among the very few likely candidates [8] for these ultra high energy cosmic ray sources are active galactic nuclei (AGN) and gamma ray bursts (GRBs) in which also neutrino production may occur. Moreover, the associated sources should be confined within a few 10 Mpc of the Earth to contribute to the observed cosmic ray spectrum due to the Greisen-Zatsepin-Kuz'min or GZK limit [9] [10].

## 0.2 The Greisen-Zatsepin-Kuz'min limit

In 1965, Kenneth Greisen [9], Vadim Kuzmin and Georgiy Zatsepin [10] independently predicted that high energy cosmic rays traveling through outer space can scatter with the omnipresent photons of the cosmic microwave background [1] to create charged and neutral pions via the  $\Delta^+$  resonance

$$p + \gamma \rightarrow \Delta^+ \rightarrow n + \pi^+ \quad (1a)$$

$$p + \gamma \rightarrow \Delta^+ \rightarrow p + \pi^0 \quad (1b)$$

when the cosmic rays energy crosses the threshold of  $5 \times 10^{19}$  eV. The mean free path associated with the interaction drops considerably above this energy threshold which is referred to as the GZK limit. This results in the prediction that the observed cosmic ray flux at Earth will be strongly suppressed above  $5 \times 10^{19}$  eV. At these extreme energies, only cosmic rays coming from within the local supercluster of galaxies, that is from astrophysical sources within 100 Mpc from Earth can be detected.

With the emergence of large high-sensitivity cosmic ray telescopes, the GZK limit can now be measured. The High Resolution Fly's Eye (HiRes) detector [11], the AGASA surface array detector [12] and the Pierre Auger Observatory (PAO) experiment [13] have studied the cosmic ray flux in this energy domain. Figure 3 presents an expanded view of the cosmic ray spectrum shown in Figure 1. Only the more recent measurements are shown for energies between  $10^{18}$  eV and  $10^{21}$  eV. As can be seen in the figure, both the HiRes and the PAO results show a steepening in the cosmic ray flux beyond  $3 - 5 \times 10^{19}$  eV which is consistent with

## CONTENTS

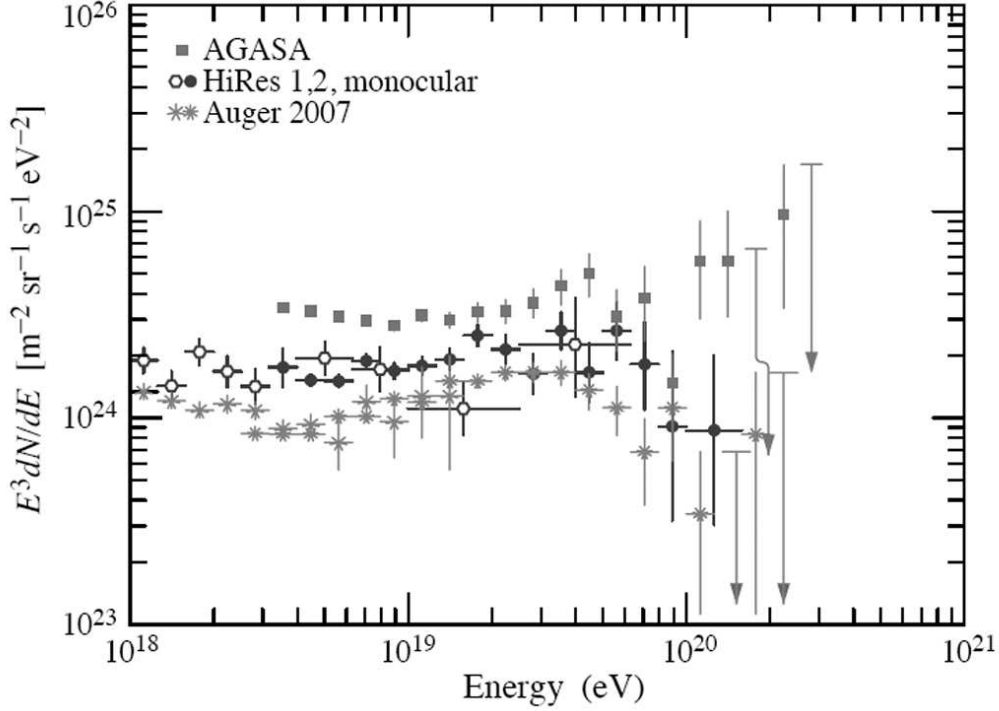


Figure 3: The measured cosmic ray energy spectrum for energies between  $10^{18}$  eV and  $10^{21}$  eV. Recent measurements from AGASA [12], HiRes [11] and Auger [13] are shown. The plot was taken from reference [3].

the existence of the GZK limit. However, the flux measurements by AGASA [12] seem in contradiction with the data of the other two observatories. They are in favor of a non-acceleration scenario for explaining the origins of ultra high energy cosmic rays. This alternative model predicts that the excess of cosmic rays measured above the GZK limit results from the decay of very massive, long-lived particles such as topological defects [14].

The discrepancy between the observed spectra is often attributed to a failing energy calibration of the AGASA detector [15], but this issue remains controversial. Further information on the origin of ultra high energy cosmic rays could be obtained by searching for high energy neutrinos. High fluxes of neutrinos are expected regardless of the cosmic ray production scenario. They are believed to be produced in the acceleration of cosmic rays or by the decay of topological defects. The detection of ultra high energy neutrinos could conclusively close the debate on the existence of the GZK limit and the origin of the very high energy cosmic rays. It would also help understand the physics of extreme astrophysical objects such as active galactic nuclei. In the framework of this thesis, only neutrinos from accelerated cosmic rays will be considered. The predicted mechanism of production for such neutrinos is described below.

While confined by the high magnetic fields at the acceleration site, some fraction of the cosmic rays suffer resonant pion photoproduction with the ambient photons as in equation 1a and 1b. This leads to electron and muon neutrinos through the decay of the produced charged pions

$$\pi^+ \rightarrow \mu^+ + \nu_\mu \rightarrow e^+ + \nu_e + \nu_\mu + \bar{\nu}_\mu \quad (2a)$$

$$\pi^- \rightarrow \mu^- + \bar{\nu}_\mu \rightarrow e^- + \bar{\nu}_e + \nu_\mu + \bar{\nu}_\mu \quad (2b)$$

and the free neutron

$$n \rightarrow p + e^- + \bar{\nu}_e . \quad (2c)$$

According to the equations 2a, 2b and 2c, the flavour ratio of the high energy cosmic neutrino flux is typically  $\phi_{\nu_e} : \phi_{\nu_\mu} : \phi_{\nu_\tau} = 1 : 2 : 0$  at the source, where  $\phi_{\nu_l}$  is the combined flux of neutrinos and anti-neutrinos for the flavour  $l$ . After propagation over cosmological distances, a flavour ratio of  $\phi_{\nu_e} : \phi_{\nu_\mu} : \phi_{\nu_\tau} = 1 : 1 : 1$  is observed at Earth due to the phenomenon of neutrino oscillations [16]. All three flavors of neutrinos are therefore initially of the same importance for detection. However, the probability of detection of muon neutrinos is higher due to the long path length of the muons they produce in interaction with matter.

## 0.3 Active galactic nuclei

The Pierre Auger Observatory has recently reported a direct correlation between the highest energy cosmic rays observed and the presence of nearby active galactic nuclei, lying within 75 Mpc from Earth [13]. Active galaxies are therefore also likely sources of high energy cosmic neutrinos.

The term active galactic nuclei or AGN refers to the existence of very energetic phenomena occurring in the core of some galaxies. The amount of radiation emitted by the central source is at least comparable to the energy radiated by all the stars in the galaxy. Such galaxies are thought to possess a massive black hole at their center as high as  $10^{6-9}$  solar masses that powers their enormous energy output. Several types of AGN can be recognized, based on the mass of their central engine.

The two main subclasses of AGN are Seyfert galaxies and quasars. Both possess very luminous nuclei which appear almost starlike but with strong and broad emission lines from highly ionized gas. These emission lines show evidence for the presence of large amounts of very hot and fast-moving gas, accreting around the galactic center. Seyfert galaxies were the first active galactic nuclei to be identified. They are named after Carl Keenan Seyfert who discovered them in 1943. Seyfert galaxies are thought to be powered by a moderate-mass black hole. Quasi-stellar radio sources or quasars show emission lines in their spectra which are even more prominent than for Seyfert galaxies. They also present very large redshifts, indicating by the Hubble law that they are at great distances.

## CONTENTS

Some of the quasars which have been observed so far are about 10 billion of light-years away. The fact that they are visible at such distances implies that they emit enormous amounts of energy and can not be stars in our Galaxy. Because of these observations, quasars are believed to be active galactic nuclei with a high-mass black hole.

The radiation cannot be produced by the supermassive black hole itself as it is invisible but by the surrounding interstellar gas accreting onto it. Observations show that narrow beams of energetic particles are ejected in opposite directions from this accretion disk. Even though uncertainties remain, the mechanisms involved in the production and acceleration of the jets are most likely due to acceleration in the ambient magnetic fields. The gas is attracted by the black hole and as it slowly spirals towards the center of the galaxy, its gravitational potential energy is converted into thermal energy. The thermal energy can accelerate jets of material from the accretion disk to relativistic speed. Among the radiation products of the jets are protons which can interact with the ambient radiation in the AGN to give neutrinos according to the equations 2a and 2b. With exceptional gravitational forces in the vicinity of their central massive black hole, active galaxies are believed to possess the tremendous amounts of energy needed to accelerate cosmic rays and produce neutrinos up to the highest energies.

## 0.4 Discussion

The main topic of this thesis is to study whether neutrino telescopes can be used to search for ultra high energy neutrinos. These neutrinos are speculated to be produced in the Fermi acceleration of cosmic ray protons in extragalactic sources. The recently reported results on ultra high energy cosmic ray production [7] [13] indicate that active galactic nuclei are likely sources of high energy cosmic neutrinos. Since cosmic rays with energies close to  $10^{20}$  eV have been observed, neutrino beams of similar energy are expected as well [2].

The small interaction probability of neutrinos make them difficult to detect. However, the products of their interactions are observable through the Cherenkov effect in a transparent medium such as water or ice. The predicted fluxes of ultra high energy neutrinos are most likely within reach of the first generation of neutrino telescopes and certainly detectable by future kilometer-scale neutrino observatories. The neutrino telescope ANTARES is constructed to search for high energy neutrinos. Its sensitivity to neutrino events above  $10^{16}$  eV and up to the GZK cut-off has been evaluated in the framework of this thesis. At these ultra high energies, the Earth is opaque to neutrinos and only downward-going and horizontal neutrinos can arrive at the detector. Since neutrino telescopes such as ANTARES are optimized for the detection of upward-going neutrinos in the energy range from  $10^{11}$  eV to  $10^{16}$  eV, it needs to be investigated whether downward-going neutrinos of energy beyond  $10^{16}$  eV can be observed. This is of relevance not

only for the ANTARES telescope but also for the future cubic kilometer-scale detector KM3NeT. It will provide information for the optimisation of the geometry of the telescope and the technologies required.

Rather than searching for neutrinos from a specific source, a non-localised flux of high energy neutrinos has been considered. Such an approach gives an higher probability of detection, in the case the neutrino flux from individual sources would be too small to be detected by a neutrino telescope of the size of ANTARES. As muon neutrinos have an higher detectability, the diffuse flux of muon neutrinos from AGN has been considered. This neutrino flux can be modelled by a generic  $E^{-2}$  spectrum with units of  $10^{-6} \text{GeV cm}^{-2} \text{s}^{-1} \text{sr}^{-1}$  [2].

A description of the ANTARES neutrino telescope and the detection principle involved are given in Chapter 1. A chronological analysis of the development and construction of the telescope is presented in this chapter.

The expected performance of ANTARES in the high energy range relies on a good timing resolution between the signals recorded in the photo-sensors of the telescope and a good functioning of the various mechanical and electronic components of the telescope. A time calibration method and a diagnostic tool to determine whether components are functioning as expected during the operations have been developed in the framework of this thesis. They are presented in Chapter 2. The readout system of the telescope is also described in this chapter.

The sensitivity of ANTARES to ultra high energy cosmic neutrinos has been estimated using Monte Carlo simulations. Three distinct stages of simulation can be distinguished. The first one consists in the generation of neutrino interactions in the water and seabed around the telescope. The propagation of the resulting secondary leptons towards the telescope needs then to be modeled. Finally the simulation of the detector response to the Cherenkov light induced in the photo-sensors of the telescope by the relativistic moving secondary leptons is computed by a specific detector simulation. Since the available simulations accept neutrino events within a limited range of energies only, improvement of existing packages and the development of new programs were required. The implementation of the neutrino generator ANIS and the lepton propagator MMC in the ANTARES Monte Carlo event simulation chain is described in Chapter 3. Both programs were initially designed for use with the AMANDA neutrino telescope but they have been adapted to ANTARES in order to generate ultra high energy neutrino events. A comparison between ANIS and the program GENHEN which is generally used with ANTARES is also presented. A new simulation program, named SIRENE which is capable of modeling the detector response for neutrino events up to the highest energies is presented in Chapter 4. The program allows the implementation of any neutrino telescope geometry. SIRENE has been developed for the KM3NeT detector but it has been tested with the ANTARES telescope for the analysis presented in this thesis. Results of the Monte Carlo simulation study are given in Chapter 5. A dedicated method has been developed to separate the ultra high energy neutrino signal from the large background of atmospheric

## *CONTENTS*

muons, using the characteristics of the simulated ultra high energy events in the ANTARES telescope. Optimized event selection criteria based on the arrival direction of the Cherenkov photons and the total charge deposited in the telescope have been applied. Predictions on the diffuse AGN-like muon neutrino flux limit and the associated neutrino effective area are presented.



# Chapter 1

## The ANTARES telescope

*In this chapter the detection principle and the design of the ANTARES high energy cosmic neutrino telescope are described. The technical development and construction of the detector are also presented.*



The European scientific programme ANTARES or Astronomy with a Neutrino Telescope and Abyss environmental RESearch is dedicated to Neutrino Astronomy. About 150 particle physicists, astrophysicists and engineers from 22 European research institutes and universities contribute to the project. The ANTARES collaboration is assisted by marine environment and technology experts from IFREMER, Institut Français de Recherche pour l'Exploration de la MER to deploy the different components of the telescope in the deep Mediterranean Sea. Seismologists from Géosciences Azur and Guralp System benefit from the ANTARES infrastructure to record in real-time deep-sea seismic activity data, occurring both in the vicinity of the telescope or anywhere else in the world.

ANTARES is an open-water neutrino telescope composed of photo-sensors optimised for the detection of Cherenkov light emitted by upward-going muons resulting from high energy cosmic muon neutrinos interacting with atomic nuclei in the deep water or seabed. Unlike high energy photons that can be absorbed before reaching the Earth, or protons which can be deflected by magnetic fields, neutrinos can travel over very large distances without any disruption, straight from their origin. Neutrinos can provide new knowledge about astrophysical processes, alongside photons and cosmic ray particles. By observing neutrinos, ANTARES is able to explore new features of the Universe over a large range of distances and energies.

A neutrino telescope can study for instance, the processes involved in the most

## The ANTARES telescope

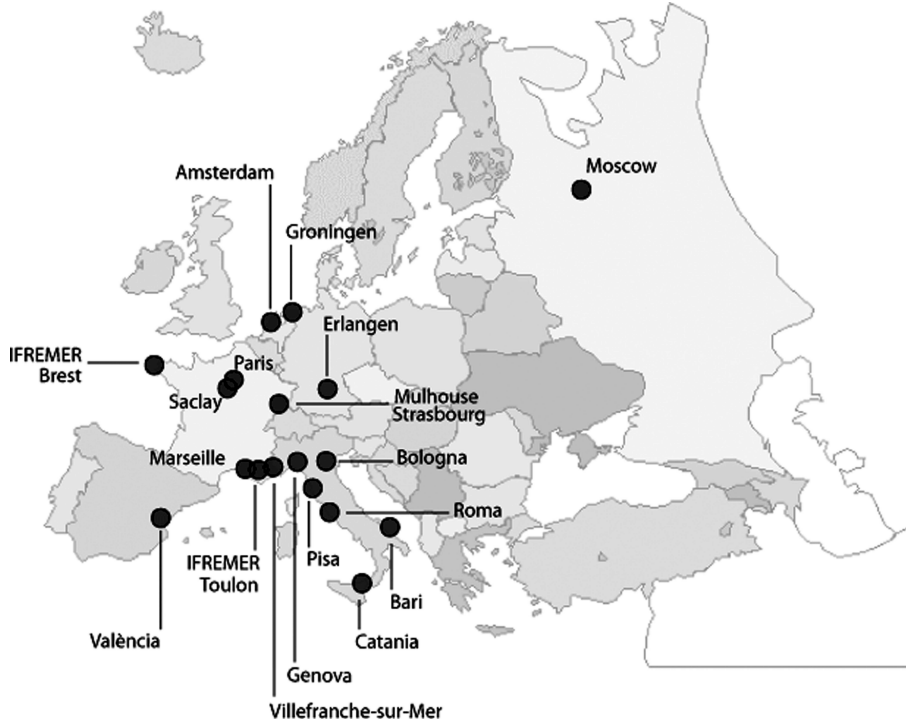


Figure 1.1: The ANTARES collaboration consists of 150 scientists from 23 European institutes in France, Germany, Italy, the Netherlands, Russia and Spain.

energetic astrophysical phenomena of the Universe such as supernovae remnants (SNRs), active galactic nuclei (AGN) and gamma ray bursts (GRBs) or the central parts of stars which are opaque to photons. The ANTARES telescope will open a new window on our Universe and may also shed light on the mysterious nature and origin of dark matter and the cosmic radiation which bombards the Earth's atmosphere at high energies. Catching the weakly interacting neutrinos requires a telescope with a very large detection volume to increase the chance of detection. With an instrumented volume of about  $0.02 \text{ km}^3$  and an aperture of  $0.1 \text{ km}^2$ , ANTARES constitutes a first step towards the future European cubic kilometer-size neutrino telescope KM3NeT. This giant photo-detector array will be large enough to capture and study the neutrinos associated with the rarest and highest energy cosmic rays, up to the Greisen, Zatsepin and Kuz'min (GZK) cutoff [9] [10].

ANTARES is sensitive to the light produced by the secondary particles created in neutrino interactions in the seabed rock and water in and surrounding the detector. In Section 1.1 the detection principle of high energy cosmic neutrinos employed by the ANTARES telescope is described. The various optical backgrounds which have to be taken care of when analysing reconstructed muon trajectories for neutrino source searches are discussed in Section 1.2. The design and architecture of the ANTARES telescope are described in detail in Section 1.3.

The history of the construction of the telescope and its present status are presented in Section 1.4.

### 1.1 Neutrino detection principle

The ANTARES telescope is based on the original idea of Moisei Aleksandrovich Markov [17] who proposed in 1960 the deep sea (or ice) as a suitable site for the construction of a large neutrino telescope. Open-water neutrino telescopes use the Earth as a shield to filter all particles except neutrinos and detect Cherenkov light emitted by neutrino-induced muons or neutrino-induced electromagnetic and hadronic showers. Neutrino charged-current interactions in the water surrounding the detector and in the rock below the detector give rise to upward-going charged secondary particles such as muons and electrons depending on the flavor of the neutrino. The relativistic secondary particles moving through the seawater faster than the speed of light in that medium will emit photons in the blue wavelength range. These photons are known as Cherenkov light, named after the Russian scientist Pavel Alekseyevich Cherenkov, who discovered this phenomenon in 1934. Cherenkov radiation occurs when a charged particle exceeds the speed of light in a dielectric and optically transparent medium through which it passes. The minimum velocity at which this process can occur is defined as the Cherenkov threshold

$$\beta \geq \frac{1}{n}$$

with  $n$  the index of refraction of the transparent medium, and  $\beta = v/c$  the velocity of the particle  $v$  expressed as a fraction of the speed of light in vacuum  $c$ . The energy is released in the form of a coherent electromagnetic wavefront. The number of Cherenkov photons emitted by a particle with unit charge per unit wavelength and per unit track length is

$$\frac{d^2 N_\gamma}{dx d\lambda} = \frac{2\pi\alpha}{\lambda^2} \left(1 - \frac{1}{\beta^2 n^2}\right) \quad (1.1)$$

with  $\alpha$  the fine-structure constant and  $\lambda$  the wavelength of the emitted photon. Cherenkov radiation can be detected by the three-dimensional array of photo-sensors constituting the ANTARES telescope. The detection of Cherenkov photons will make it possible to reconstruct the trajectory of the secondary particle which had emitted them, and subsequently the direction of the neutrino which points back straight to its source. Cherenkov photons are emitted only at a certain fixed angle with respect to the direction of motion of the charged particles, resulting in a cone of blue light. The angle of emission is related to the charged particle velocity and the refractive index of the local medium. This angle is called

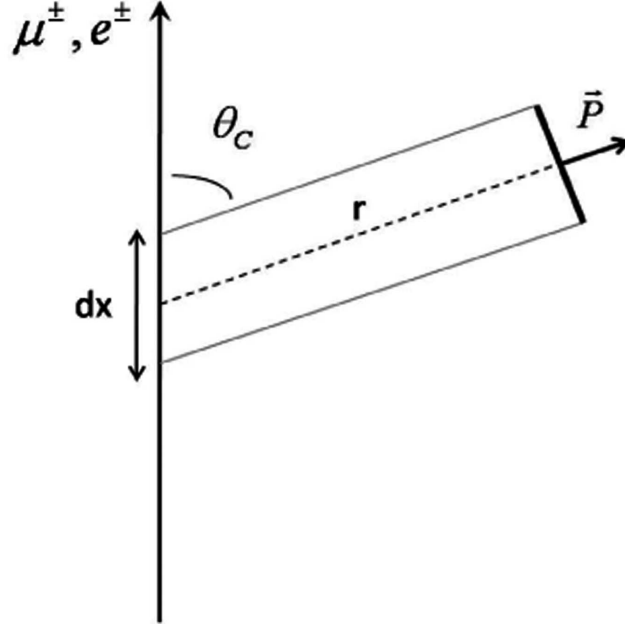


Figure 1.2: Charged particles moving at relativistic speed through a transparent medium are described by a track of length  $dx$ , emitting photons under the Cherenkov angle  $\theta_c$ . The photons travelling on a distance  $r$  create a photon field shockfront  $\vec{P}$ .

the Cherenkov angle  $\theta_c$  and can be expressed by the following equation

$$\cos \theta_c = \frac{1}{n\beta}. \quad (1.2)$$

In the energy range interesting for ANTARES, that is above 10 GeV, particles are ultra-relativistic and  $\beta$  is close to 1. The refractive index of the seawater at the ANTARES site is 1.35. Thus, the Cherenkov angle is approximately  $42.5^\circ$ .

As the Cherenkov photons are emitted in the form of a cone of light, a precise reconstruction of particle trajectories requires the measurement of only a few hits in the various photo-multiplier tubes (PMTs) of ANTARES at different space points. The light emitted by a track of length  $dx$  can be projected upon a surface  $S_C$  defined by

$$S_C = 2\pi r dx \sin^2 \theta_c$$

with  $r$  the distance travelled by the photons. This is illustrated in Figure 1.2. According to Equation 1.1 with  $\beta = 1$ , this last result yields a photon flux observed in the electromagnetic wavefront at a distance  $r$  from the track of length  $dx$

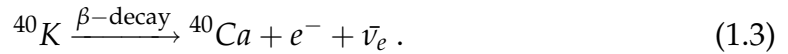
$$dN(r) = \frac{S_C \alpha}{r \lambda^2} d\lambda.$$

In the deep Mediterranean Sea, at the ANTARES site, about  $3.5 \times 10^4$  Cherenkov photons are emitted at wavelengths between 300 and 600 nm per meter of track.

## 1.2 Background signal

Atmospheric muons from hadronic showers are produced at 10 – 20 km height when cosmic ray particles interact with nuclei in the atmosphere. These downward-going muons can be mis-reconstructed as upward-going muons from cosmic muon neutrino interactions in the matter below the telescope and represent a serious background for neutrino astronomy. To simplify the discrimination between up-ward-going muons and the much higher flux of downward-going muons, the large background of atmospheric muons and muon bundles induced by cosmic ray atmospheric showers needs to be minimized. This can be realized by installing the telescope at a deep site where a large layer of seawater will act as a shield. At a depth of 2475 m, the expected background rate in ANTARES from atmospheric cosmic ray muons is about 30 Hz. To improve the filtering of the atmospheric background, the photo-multiplier tubes (PMTs) of the telescope are oriented  $45^\circ$  with respect to the vertical downward direction thus focusing their apperture on the upward-going muons. This specific orientation towards the seabed also prevents bio-fouling to be a serious problem. The signal loss due to bio-deposition and sedimentation has been measured [18] to be less than 2% per year.

The expected rate of atmospheric muons at the ANTARES site is small compared to the effect of the  $\beta$ -decay of potassium  $^{40}\text{K}$  in sea water which contributes 30 kHz to the single rate of each PMT. It is also rather insignificant with respect to the rates due to occasional bio-luminescence, caused by living organisms around the telescope which can peak during short bursts up to MHz rates and is dependent on the strength of the sea current. The  $\beta$ -decay process of  $^{40}\text{K}$  in salty sea water can be expressed as follows:



The produced electron has a maximum energy of 1.3 MeV which is sufficient to give Cherenkov light detectable by ANTARES. To study this environmental background, the ANTARES telescope includes devices to monitor the deep-sea parameters, such as water salinity and water current in order to better understand the  $^{40}\text{K}$  and bio-luminescent backgrounds [19].

## 1.3 Detector layout

The ANTARES telescope is located at a depth of 2475 m on the Mediterranean seabed. The exact location of the telescope is  $42.50' \text{ N}$ ,  $6.10' \text{ E}$  which is approximately 40 km off the coast of Toulon in France. The detector is monitored from an on-shore control room (known as the shore station) in Institut Michel Pacha in La Seyne-sur-mer, a French laboratory dedicated to research of Marine Biology and Physiology. Electrical power to the telescope is transferred from the beach by a

## The ANTARES telescope

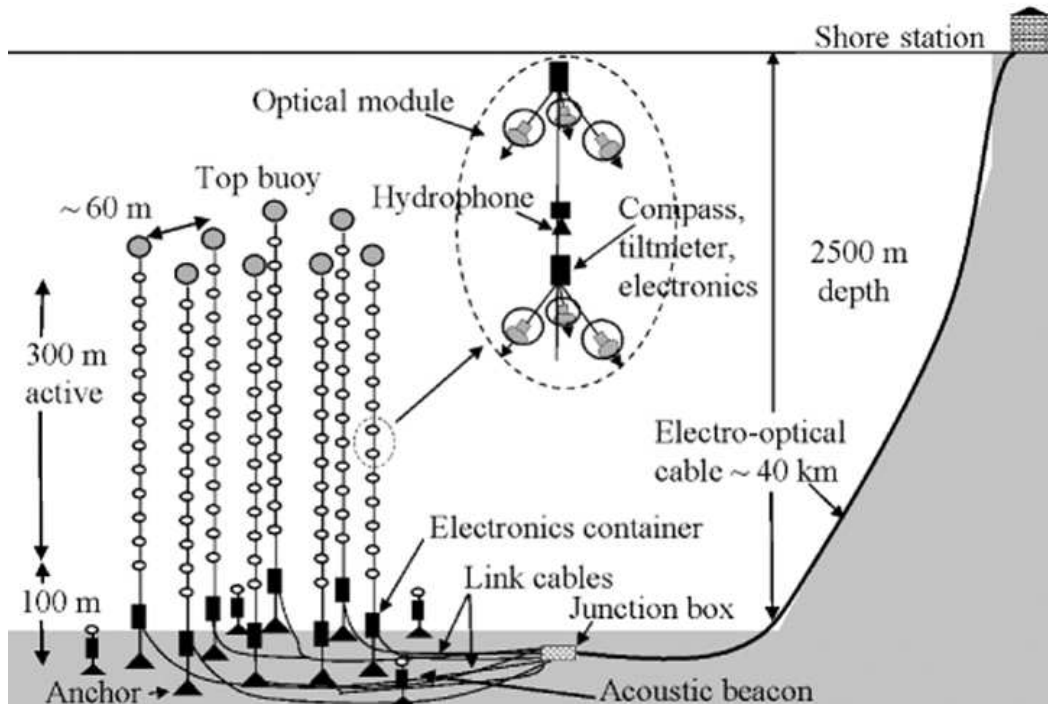


Figure 1.3: *Schematic view of the ANTARES telescope showing the main components of the neutrino detector.*

40 km long deep-sea cable referred to as the main electro-optical cable (MEOC) which also provides data transmission from and to the shore, using optical fibers. At the ANTARES site, on the bottom of the sea, the cable is connected to a junction box (JB) distributing the power to the detection lines which constitute the neutrino telescope. The junction box (JB) was the first object that has been deployed in December 2002. The ANTARES telescope itself consists of a three-dimensional array organised in twelve vertical independent detection lines carrying a total of 900 photo-multiplier tubes operating at depths from 2375 to 2000 m. A schematic overview of the ANTARES telescope is shown in Figure 1.3. As can be seen in the figure, the detection lines are separated from each other by a distance of 60 to 75 m. Each line also supports hydrophones for acoustic positioning and a LED optical beacon for time calibration (cf. Section 1.3.2). A thirteenth line, called the instrumentation line is equipped with specific instruments to monitor the sea environmental parameters at the ANTARES site. A detailed description of the instrumentation used on this line can be found in Section 1.4.4.

### 1.3.1 Detection lines

The detection lines of ANTARES are anchored to the Mediterranean seabed and can be released by means of an acoustic transmitter-receiver system if necessary.

### 1.3 Detector layout

Two syntactic foam buoys placed at the top maintain each line vertically. The anchor is made of a dead weight and a recoverable structure, the bottom string socket (BSS). The recovery of a line is achieved by releasing part of the BSS after issuing an acoustic command from a ship at the sea surface. The BSS is connected with an electro-optical cable, the interconnecting link (IL) to the junction box (JB) which provides electrical power to the lines and allows for the transmission of data.

The backbone of each detector line consists of an electro-optical cable. It provides mechanical strength to the lines, electrical power and an optical data link to the storeys. A full line is approximately 450 m long with an active length of 350 m. It is composed of twenty-five storeys each carrying three optical modules (OMs) mechanically supported by a titanium frame. A storey of the detector is shown in Figure 1.4. The vertical distance between two consecutive storeys is 14.5 m. Together five storeys constitute one sector of a detection line which has its own communication channel to shore. The storey closest to the seabed is placed at a height of 100 m so the bottom part of the line is uninstrumented to provide a larger region for observing Cherenkov cones while they are developing. The three OMs of a storey point downwards at an angle of  $45^\circ$  with respect to the vertical in order to increase the sensitivity to up-going muons. The chosen arrangement of the OMs leads to the detection of light in the lower hemisphere with high efficiency, and has also some acceptance for muon directions above the horizontal plane.

#### 1.3.2 Electronics containers

Each detection line of ANTARES is instrumented with electronics containers and special containers housing acoustic devices and calibration equipment. Every storey is associated with a local control module (LCM) located at the center of the titanium optical module frame (OMF). A string control module (SCM) is placed at the base of each line in a container at the bottom string socket (BSS) which also houses the string power module (SPM). The first LCM on the line is linked to the SCM and the last LCM is connected to the top buoy. The LCM and SCM containers hold the electronic boards for all readout functionalities at the storey level and at the detection line level, respectively. The electronics in the containers host the data acquisition and slow-control systems of the neutrino telescope and constitute a single node of the data transmission network, receiving and transmitting data, slow-control and clock commands from the telescope to the shore station and vice-versa. In each sector of a detection line there are four slave LCMs and one master LCM (MLCM). Each LCM slave controls the data transmission of the three optical modules (OMs) of a storey and sends these data to the MLCM. The MLCM collects all data from the corresponding sector and sends them to shore. It receives orders from the shore station and distributes information to the LCMs through an Ethernet channel.



Figure 1.4: *Schematic view of a complete storey (or floor) of the ANTARES telescope with three optical modules, a cylindrical container housing the electronics in the center of the three optical modules, an optical beacon above this cylinder and a hydrophone below the optical modules.*

### **1.3.3 Optical modules**

The optical module (OM) is the basic detector component of the ANTARES telescope. A high-pressure resistant glass sphere houses a 10-inch Hamamatsu photo-multiplier tube (PMT) and electronics to filter and amplify the signal. The sphere consists of two hemispherical parts with an outer diameter of 17 inches and a wall thickness of 15 mm. The light transmission through the glass is more than 95% for the blue wavelengths corresponding to those of the Cherenkov light emission. The PMT is fixed to the front part of the sphere with a transparent silicon-rubber gel with somewhat different optical properties as compared to the glass envelope and the photo-multiplier window. The refractive index of the gel is 1.404 which results in an additional optical transition between the water (with a refractive index of 1.35) and the glass (with an index of 1.47). Apart from an optical link, the gel is also a mechanical link between the sphere and the PMT magnetic shield.



### 1.3 Detector layout

The PMT is protected by a magnetic shield from the Earth's magnetic field which could degrade the uniformity of its response. The Earth's magnetic field would influence electron trajectories between the photo-cathode and the first dynode of the PMT. The magnetic shield has the form of a metal cage composed of two parts: a hemispherical part which covers the photo-cathode of the PMT, and a flat part with a hole at its center for the neck of the PMT. The hemispherical part of the magnetic shield is positioned in the gel while the flat part is mounted around the neck of the PMT. The hemisphere which supports the PMT constitutes the major part of the aperture of the detector. The other hemisphere is equipped with an electrical penetrator which provides the connection to the power and acquisition system outside the OM. To reduce the sensitivity to photons hitting the back of the OM, the inside of the back hemisphere has been covered with black paint.

The PMT selected for the ANTARES telescope is the hemispherical Hamamatsu R7081-20 tube which has a diameter of 10 inches and a correspondingly large active area of about  $500 \text{ cm}^2$ . This provides the OM with a large angular acceptance, falling to half its maximum at about  $70^\circ$  from the axis. The photo-multiplier is sensitive to single photons in the wavelength range from 300 nm to 600 nm. Its quantum efficiency is largest in the wavelength range from 350 to 450 nm and amounts to about 25%. The timing resolution of ANTARES which is essential for the precise determination of the direction of a muon relies on the transit time spread (TTS) of the PMTs. To measure the TTS of a photo-multiplier tube, a LED system consisting of a blue LED and a pulser are used. The LED is glued onto the rear of the PMT bulb and illuminates the photo-cathode. The

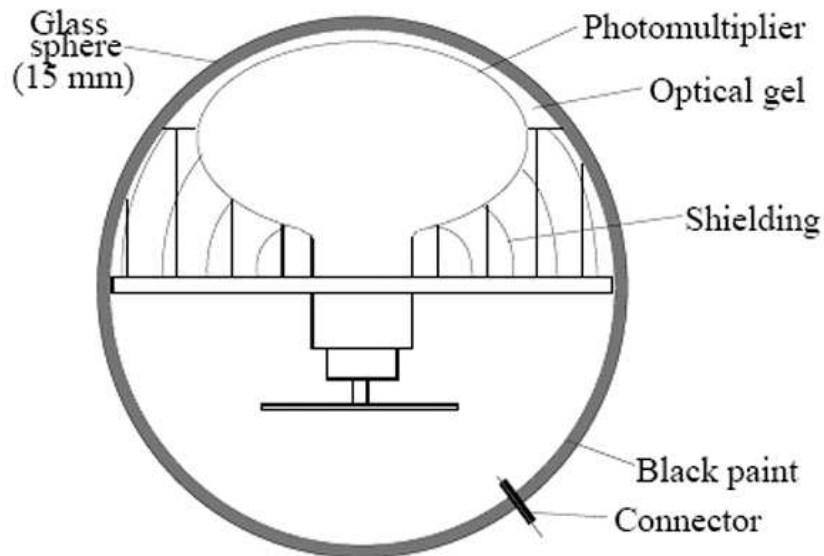


Figure 1.5: Schematic cross section of an optical module (OM) of ANTARES.

pulser card is also glued onto the photo-multiplier tube and is triggered by a clock signal. The measured single photon TTS of the PMT is about 2.6 ns (FWHM).

### **1.3.4 Sea monitoring instrumentation**

The detection lines of ANTARES also contain instruments for the acoustic positioning of the telescope and the monitoring of the deep sea properties. As the detection lines are anchored to the seabed and maintained vertically by buoys, they undergo drifts of a few tens of meters (as measured at the top of the lines) due to the deep-sea underwater currents. The relative positioning of the lines is based on underwater acoustic techniques monitoring these motions. The system consists of a three-dimensional array of transponders and acoustic modules exchanging precisely timed acoustic signals between each other. The acoustic modules are emitter-receivers located on the BSS of each line and receivers distributed along the lines, one receiver being placed in every sector. The receivers are composed of an hydrophone with dedicated electronics.

The method used for determining the relative position is to measure the travel time of acoustic pulses between the receiving hydrophones and the emitter-receivers. Apart from the hydrophones and emitter-receivers on the detector lines, several transponders are located as independent units anchored at different places to the seabed, in the vicinity of the telescope. These transponder units contain their own electronics and are controlled remotely by the emitter-receivers modules on the detection lines of the telescope. While the acoustic system provides the relative positioning, the global positioning of ANTARES is obtained by acoustic triangulation of the emitter-receiver modules and a surface ship equipped with GPS. The acoustic positioning precision strongly depends on the precision by which the sound velocity in water has been measured as it directly determines the relative distance between the hydrophones.

Environmental parameters such as the temperature, the salinity of the sea water and the evolution of the pressure at the telescope's site influence the sound velocity and need to be measured continuously. Sound velocimeters are placed at various places of the telescope along the detection strings. Two of them are also equipped with conductivity, temperature and pressure probes, while conductivity-temperature-depth (CTD) devices also provide an estimate of the salinity and temperature of the deep-sea water. These instruments provide information on environmental properties that are relevant for both the associated sciences (oceanography) and the neutrino telescope data analysis.

Tiltmeters and compasses are placed in each BSS and optical module frame (OMF) of the telescope to give an additional measure of the position of the different OMs as well as their orientation. All these oceanographic instruments are also present on the so-called instrumentation line of ANTARES whose purpose is to monitor the deep sea parameters and to provide calibration parameters of the telescope. This additional line is dedicated entirely to marine property mea-

surements and runs independently of the rest of the telescope. It also contains devices to measure the attenuation of the light absorption in sea water in order to determine the optical water properties at the telescope's site which vary in time. The instrumentation line is equipped with an acoustic Doppler current profiler (ADCP) to monitor the water current flow.

The position of the optical modules is measured with the optical beacon device of ANTARES which consists of a set of LED beacons at four different places along the detection lines and a laser beacon fixed to the BSS of the instrumentation line. A procedure to determine the relative timing calibration that was developed for the prototype instrumentation line MILOM (see Section 1.4.4) in preparation of using it for the entire telescope is detailed in the next chapter.

## 1.4 Development and Construction

### 1.4.1 Demonstrator Line

The ANTARES project was launched in 1996. After a design study period, a first prototype line consisting of seven optical modules (OMs) and several instruments for position monitoring and calibration was deployed in 1999 and connected to the shore at 1100 m depth about 37 km from Marseille. The line used an already existing undersea cable donated by France Telecom. This made it possible to take data in a telephone exchange centre in Marseille with the prototype line. The main purpose of this prototype line, referred to as the Demonstrator Line was to investigate the feasibility of the overall principle of the ANTARES telescope and various specific aspects of the ANTARES design, in particular the acoustic positioning system. The line was in operation until June 2000 and allowed the detection and reconstruction of the first muon signals.

In parallel a detailed programme of in situ measurements has been undertaken since October 1996, in order to find a suitable location for the ANTARES telescope considering several determining parameters such as the depth, the water transparency, the optical background, and the strength of the deep-sea currents. This has led to the selection of a site near Toulon (42.50' N, 6.10' E) at a depth of 2475 m. In October 2001, a new 40 km long electro-optical cable for the power and data transmission was successfully deployed between the telescope site and the shore station in La-Seyne-sur-mer. One year later, in December 2002, the Junction Box was installed on the seabed and connected to the main electro-optical cable.

### 1.4.2 Prototype Sector Line and Mini Instrumentation Line

Between November 2002 and March 2003, the Prototype Sector Line (PSL) and the Mini Instrumentation Line (MIL) were deployed and connected to the Junc-

## *The ANTARES telescope*

tion Box (JB). The two prototype lines allowed to test in deep-sea conditions, the (almost) final design for the ANTARES telescope, using prototype electronics boards. The PSL was a short prototype of a full optical detector line with only 15 (instead of 75) OMs. It consisted of a single sector of five storeys equipped with OMs. A schematic view of the PSL is shown in Figure 1.6. The sector line also contained equipment to test the acoustic positioning system: the standard acoustic receivers and transmitters RtRx at the base of the line, and the receivers Rx on the first and fifth storey. A LED optical beacon was placed at the second storey for calibration purposes.

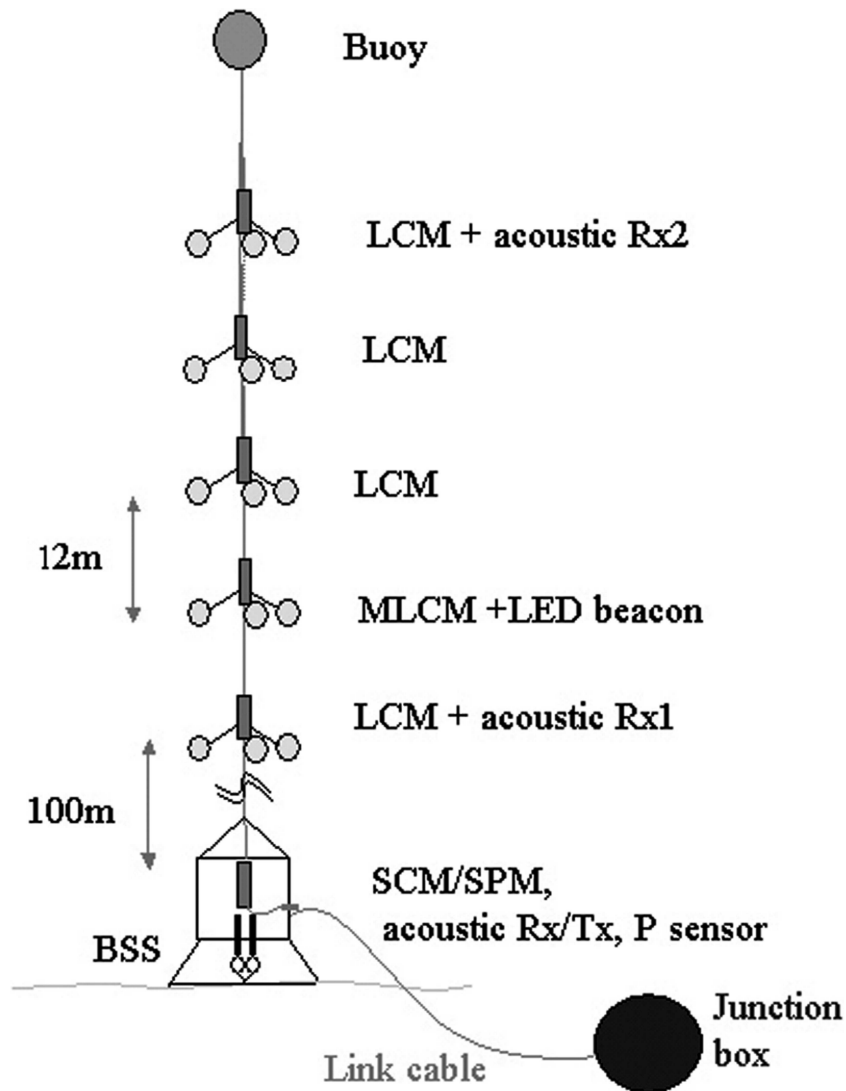


Figure 1.6: *Schematic view of the Prototype Sector Line (or PSL) of ANTARES, deployed in December 2002.*

The PSL allowed to measure the level and variation of single photon counting rates in the OMs which is largely caused by bioluminescence created by deep-sea

## 1.4 Development and Construction

life forms. Unfortunately, a failure in the vertical line prevented the electronics to be synchronised and muons couldn't be reconstructed.

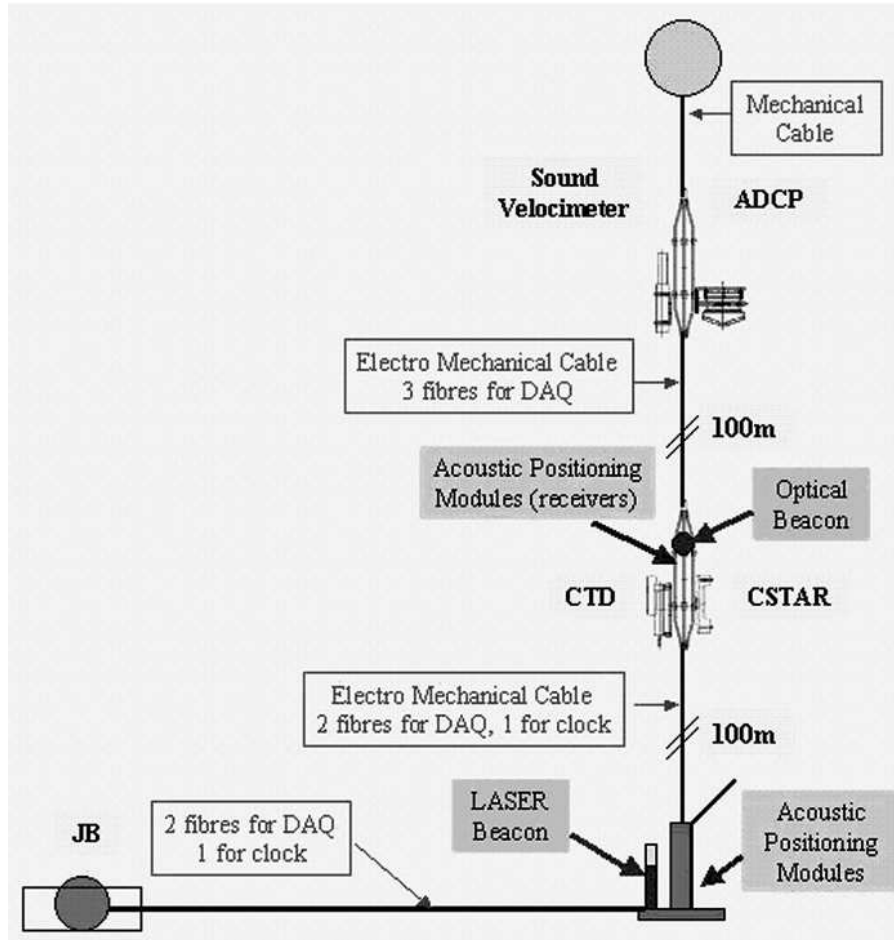


Figure 1.7: Schematic view of the Mini Instrumentation Line (or MIL) of ANTARES, deployed in February 2003.

The MIL was a prototype of the instrumentation line of the ANTARES telescope. There was no OM integrated on this line but several oceanographic probes to monitor the marine environment as well as a seismograph to study the deep-sea seismic activity in the region around the telescope. As can be seen in Figure 1.7 the MIL was also equipped with acoustic positioning modules, sound velocimeters, and instruments to probe the salinity, conductivity and temperature of the deep-sea environment. The MIL also incorporated a laser beacon placed on the Bottom String Socket (BSS) and a LED Optical Beacon on the lower storey used for the relative time calibration of the sector line. This line was operated until July 2003 proving the functionality of the various deep-sea instruments contained in the ANTARES telescope design.

### **1.4.3 Line Zero**

Because of the problems encountered with the PSL, the design of the electro-magnetic cable (EMC) had to be improved. In order to validate the new design, in September 2005 a dedicated complete 25 storey line, known as "Line Zero" [20] was deployed. Line Zero was identical to a full scale ANTARES detector line, except for the absence of photo-multiplier tubes (PMTs) in the glass spheres of the optical modules (OMs). It was equipped with an autonomous monitoring system to check the water tightness of the electronic containers such as the Local Control Modules (LCM) and the String Control Modules (SCM).

The Line Zero also allowed to monitor the attenuation of the optical fibres inside the vertical EMC linking the LCMs of adjacent storeys together. The data collected by Line Zero showed no evidence for water leaks inside the electronic containers but did reveal a sharp increase in optical attenuation in some of the fibres after some time. This could be attributed to the effect of the pressure pushing the fibres into the LCMs. By modifying the design of the connectors between the EMC segments and the LCM, this problem was solved in the final design of the detector lines.

### **1.4.4 MILOM**

The MILOM or "Mini Instrumentation Line with an Optical Module" was an upgraded version of the MIL or Mini Instrumentation Line, based on the final design of all electronics and mechanics of the telescope (except for the improved connectors described in Section 1.4.3). As can be seen in Figure 1.8, the MILOM consisted of a bottom string socket (BSS) and three storeys. In addition to the instruments inherited from the MIL, the MILOM contained four OMs: a full triplet of three OMs on the second storey, and an additional single OM at the top of the line. The OMs were mounted on the MILOM to evaluate the telescope's response, ahead of full production of the twelve detection lines which compose ANTARES. With the MILOM also, the modified electro-magnetic cable (EMC) of the telescope could be tested in-situ. It was also used to monitor the deep-sea environment and test the acoustic positioning and time calibration systems of the telescope.

The line was equipped with three sources of intense light: a laser beacon and two LED beacons attached to the first and top storeys, to illuminate the OMs and determine their relative time calibration. In Figure 1.8, the layout of the MILOM is represented.

Following its deployment in March 2005 data taking started with the MILOM right after the connection of the line to the junction box (JB) on 12 April 2005. The raw data from the OMs could be analysed immediately, thus demonstrating the success of all design changes. The MILOM line was in operation until April 2007.

## 1.4 Development and Construction

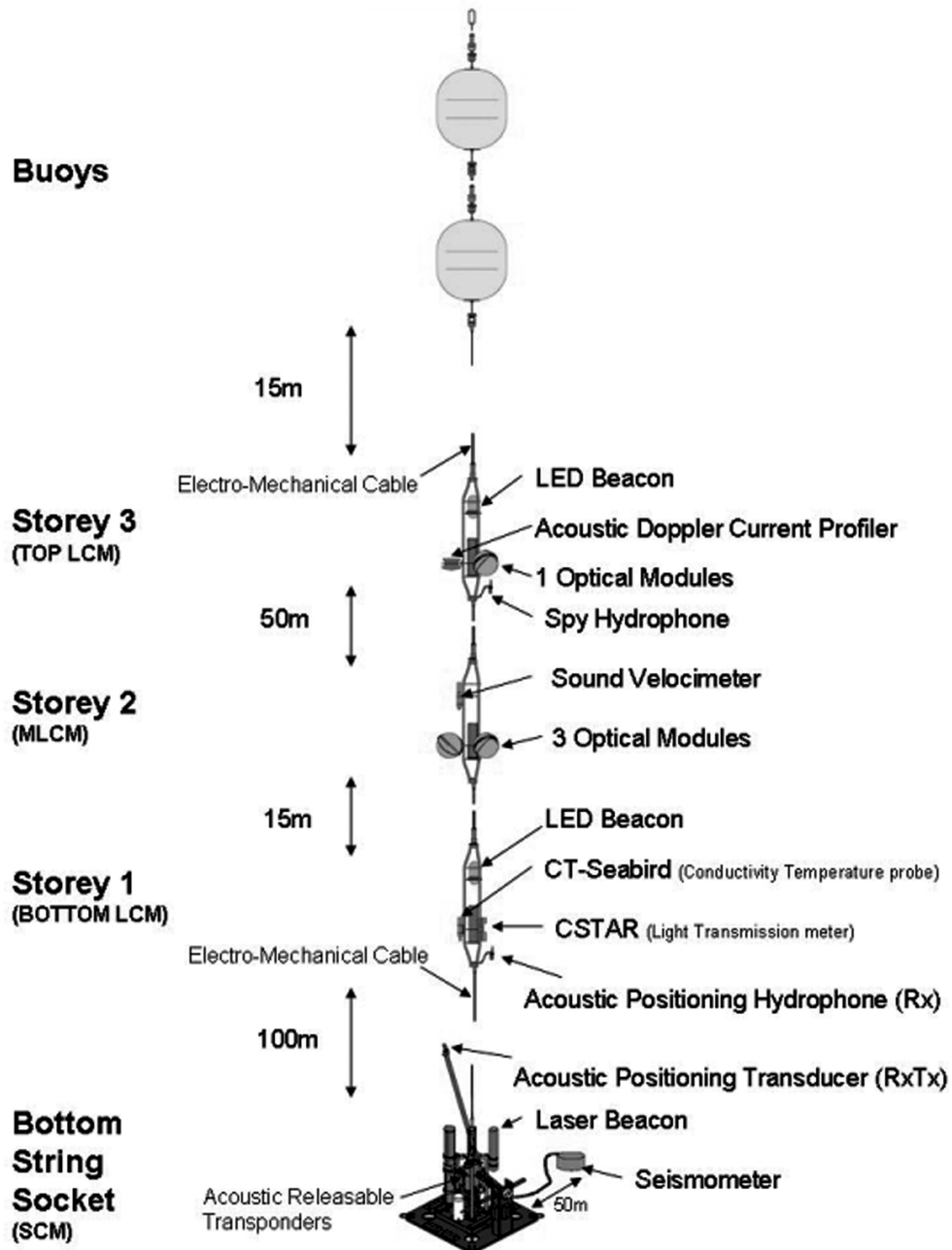


Figure 1.8: Schematic view of the Mini Instrumentation Line with an Optical Module (MILOM) of ANTARES, which was deployed in March 2005, and recovered again in April 2007.

### 1.4.5 The complete telescope

Between March 2006 and May 2008, the twelve detection lines of ANTARES have been deployed and put into operation successfully. Several hours after the connection of Line One, the first muon signals could be detected. In Figure 1.9 the

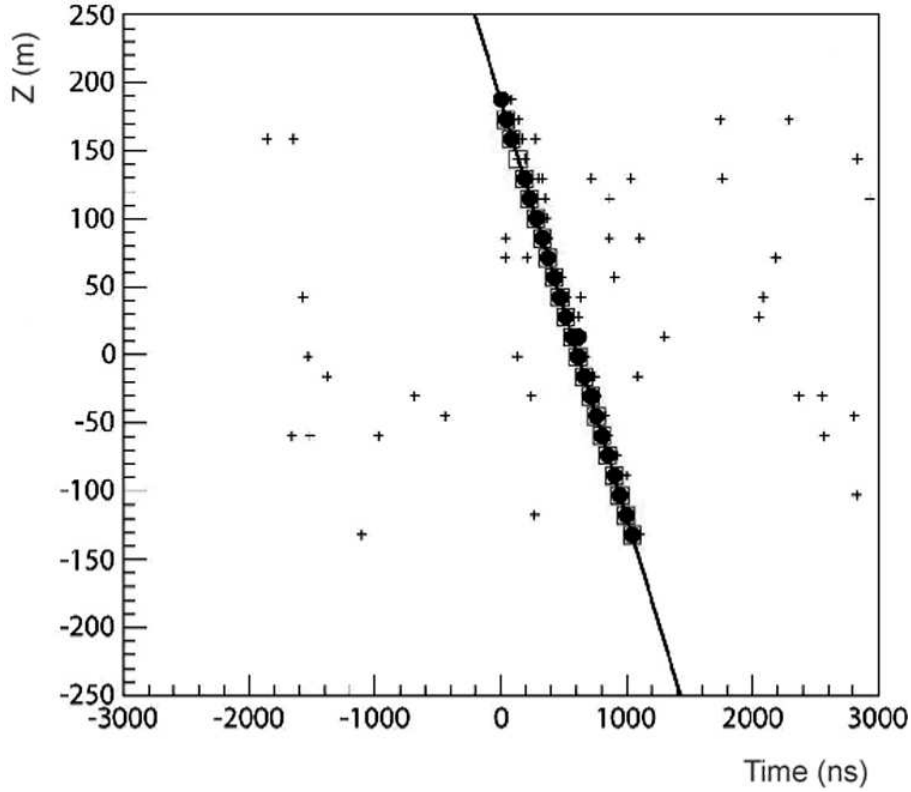


Figure 1.9: *Example of a downward-going muon event reconstructed with hits recorded by the first detection line of ANTARES, Line 1. The abscissa represents the relative time of the hit on the optical module (OM), and the ordinate represents the altitude above the seabed, altitude zero being the centre of the instrumented area of the telescope. The solid circles represent the hits that were used for the fit. The crosses represent other single-photon hits occurring during the same time interval in the telescope. They consist of random background [21] [22].*

result of the reconstruction of an atmospheric downward-going muon is shown. Data have been taken continuously for more than two years now. While the number of detection lines deployed was increasing, the efficiency of the detection was increasing as well. With five lines connected, it was possible to determine the first neutrino event candidates and estimate the performance of the telescope. It can be expressed in terms of sensitivity or upper flux limit that indicates the minimum detectable signal from an astrophysical source. The sensitivity of ANTARES after one year of observation with five detection lines is shown in Figure 1.10. The



full telescope is operational since May 30<sup>th</sup> of 2008. The search for cosmic neutrino sources has now started.

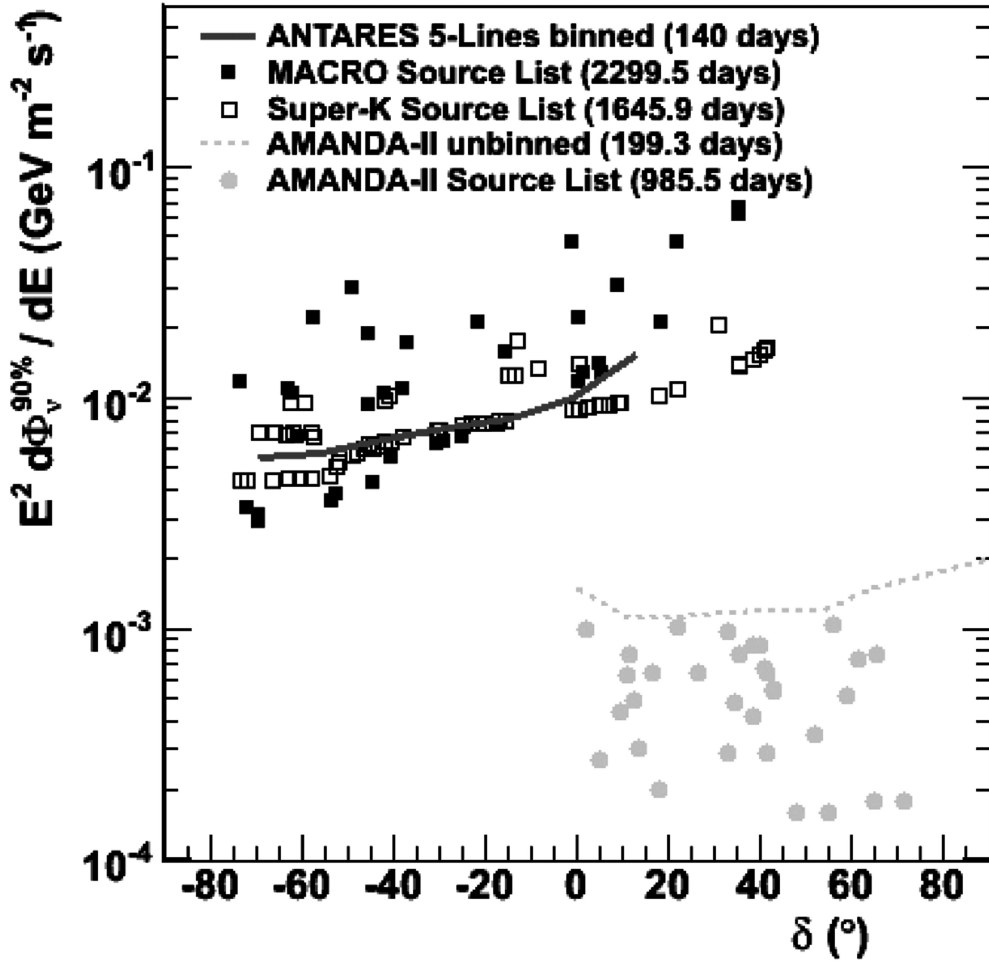


Figure 1.10: Estimated sensitivity to point-like sources with the ANTARES 5-Line data. Background has been estimated from Monte Carlo simulations. Comparison to current experiments is also shown. The sensitivity is given as a differential neutrino flux multiplied with  $E^2$  [23].

*The ANTARES telescope*

## Chapter 2

# The ANTARES data acquisition system

*In this chapter the data acquisition system of the ANTARES telescope is presented. Attention is given to a relative timing calibration procedure using the optical beacon device of the detector and the data quality monitoring system which were both developed in the framework of this thesis.*



muon tracks produced by a high-energy cosmic muon-neutrino interaction in the rock and sea water surrounding ANTARES can be reconstructed by the three-dimensional array of optical modules (OMs) which measures the arrival times of Cherenkov photons hitting the photo-multiplier tubes (PMTs) composing the telescope. The data acquisition (DAQ) system collects the time and amplitude information of the PMTs and converts the data such that they are suitable for the analysis and reconstruction software. A description of the DAQ system is given in Section 2.1. The quality of the reconstruction is expressed in terms of the three dimensional pointing accuracy or, more precisely, the angular resolution of the telescope is determined by the relative timing of each PMT signal with respect to the others. An in-situ calibration system is used to monitor the varying environmental working conditions of the apparatus and the long term variations of the relative time offsets of the PMTs. The optical beacon system of ANTARES that is used for time calibration is described in Section 2.2. The relative time calibration method is based on the determination of the time offsets of the various PMTs in response to a flash of the Optical Beacon device of ANTARES. This procedure has been tested using the MILOM prototype instrumentation line of ANTARES [19].

All critical components of ANTARES have been properly tested and calibrated

before deployment but their performance might change during operation. A diagnostic tool is therefore required to monitor whether components are functioning as expected or if they are degraded in their performance during the operations. This is the purpose of PhAntOM, the data quality monitoring system of ANTARES which is described in Section 2.3.

## **2.1 Data Acquisition**

The purpose of the data acquisition (DAQ) system is to acquire and process the data produced by the photo-multiplier tubes (PMTs). Both the arrival times of the Cherenkov photons on the PMTs and the amount of light deposited is recorded by the DAQ system. The data are digitised and subsequently transmitted to shore for off-line analysis. Contrary to other Cherenkov neutrino detectors (AMANDA, IceCube, Baikal) the data is not filtered by the front-end chips off-shore but on-shore by trigger software running on a set of computers. This is the concept of "all-data-to-shore" (ADTS). It allows the DAQ system to handle the large amount of data created by the telescope without losing information.

### **2.1.1 Readout of the data**

A Cherenkov photon arriving at the photo-cathode inside a photo-multiplier tube (PMT) can liberate an electron with a probability equal to the PMT's quantum efficiency. The electron is referred to as a photon-electron (p.e.). It induces an amplified electrical signal on the anode of the PMT. When the amplitude of the electrical pulse exceeds a threshold, the signal is digitized by the front-end Analogue Ring Sampler (ARS) chip of the PMT readout system. A voltage threshold is applied to exclude small signals due to electric noise in the PMT. Its value is typically equivalent to 30% of the signal induced by a single photon-electron hit. At the moment of threshold crossing, the ARS provides a time stamp (TS) using a local clock, an amplitude to voltage converter (AVC) value and a time to voltage converter (TVC) to interpolate between clock pulses. It also starts the integration of the anode current over a programmable time interval of typically 25 ns, yielding an estimate of the charge. Time reference is provided by the clock distribution system.

After digitisation of the PMT's analogue signal, the ARS is inactive for a period of approximately 250 ns. To reduce the associated dead-time effects on the data taking, each PMT is read out by two ARS chips, which process consecutively analogue pulses. The combined digital information on the time and the charge of the PMT constitute a single photon-electron (SPE) hit. A field programmable gate array (FPGA) buffers the hits from each ARS into so-called data frames. A frame contains all hits produced by a particular ARS within a predefined time interval of typically 13 ms. Time information is provided by the same clock signal as used

for timestamping of the PMT output signals by the ARS. The digitized data produced by the ARS chips are transmitted to shore via the master control module (MLCM) by means of an optical fibre system. Each processor in the DAQ system uses the Ethernet protocol for communication. The local control modules (LCMs) are operating at a data transmission rate of  $100 \text{ Mbit} \cdot \text{s}^{-1}$ . The data of the six ARS chip of each local control module (LCM) is sent via the optical fibres to the master LCM (MLCM) of the corresponding sector. In the MLCM, the Ethernet links from all five LCMs in the sector are merged. At the string control module (SCM), the optical signals from the six MLCMs of each detection line are collected and sent to shore via the junction box (JB) through the main electro-optical cable (MEOC). At the shore, the links are connected to a 1 Gbit Ethernet switch.

All data frames are sent as separate packages to shore, where they are processed by a set of computers which constitute the ANTARES on-line PC farm. The frames from all ARS chips together make up a timeslice which contains all data from the 13 ms period. All data contained in a particular timeslice are processed by one PC in the farm. Subsequent timeslices will go to different computers in order to allow each PC sufficient time for processing. The amount of data produced in the entire detector is too large to be stored for off-line analysis. Hence, the data needs to be filtered before storage on disk. This is the role of the trigger. When a timeslice is completed, it is passed to a fast software algorithm that searches for hits caused by a muon traversing the telescope [24], [25].

### 2.1.2 The ANTARES Trigger

Background light from radioactive  $^{40}\text{K}$  decay and bioluminescence create uncorrelated hits in the telescope whereas atmospheric muons and signal muon induced by charged-current cosmic neutrino interactions in the media surrounding the ANTARES telescope will produce hits related in position and time as a consequence of the properties of Cherenkov light. The purpose of the ANTARES trigger is to select these correlated hits in the Analogue Ring Sampler (ARS) pipeline data streams for digitisation, readout and transfer to the online data processing system on shore. The system can adjust to the variable background conditions in such a way as to retain the maximum of useful data and reject as much background as possible without losing signal. All PMT signals exceeding the low threshold values are transferred to shore. These hits are referred to as L0 hits. A L0 trigger is generated internally within the ARS when the PMT output signal reaches the low amplitude threshold designed to select single photo-electron (SPE) hits (see Section 2.1.1). This causes the charge, the time stamp (TS) and the time to voltage converter (TVC) value of each accepted SPE hit to be temporarily stored in a pipeline memory.

The L1 trigger is based on local coincidences within a storey and corresponds to a local trigger search. This trigger level is used to discriminate between uncorrelated background and muon signals. A local coincidence consists of at least two

hits on two different PMTs of the same storey within a time window of typically 20 ns. As a consequence the L1 trigger is built out of a time coincidence between at least two L0 triggers from the same storey. The time window compensates the internal delays specific to each optical module (OM). The L1 trigger software also searches for single hits with a large charge. These large hits are selected when the PMT output signal exceeds the high voltage threshold of the ARS that is typically equivalent to 3 photon-electrons (p.e.). It is unlikely that these hits are produced by single photons from uncorrelated background light but could correspond to two or more hits on the same PMT created by a muon traversing the telescope. The L1 trigger software sends a readout request to each hit OM of a local storey. This starts the digitization of all the SPE hits corresponding to a L0 trigger that have been memorized in the pipeline cells of the ARS chips.

On shore, the trigger software searches for position and time correlations between all hits that were selected by the L1 trigger. A decoding algorithm converts the raw data of the ARS into calibrated time, charge and geometry information. During data taking, calibration parameters of the detector are obtained from a table in a database where the measured parameter values of the hardware devices are stored (see Section 2.2.3). The geometry of the telescope is described in terms of positions and orientations of the PMTs. The method used to correct the time information is explained in Section 2.2.3. The time and position of hits created by unscattered Cherenkov light from the same muon path are correlated. This is called causality [24]. A group of causally related L1 hits form a so-called cluster. When the trigger algorithm finds a sufficient number of correlated L1 hits within a cluster, in any of the directions it is assumed that a muon signal is present in the data. The data that corresponds to a group of correlated hits found by the trigger algorithm is referred to as an event. Only events are stored on disk for off-line analysis. This reduces the amount of data by a factor of about  $10^4$ . Events are written as simple ASCII files. The basic concept of the used data format is explained in an ANTARES internal note [26]. The trigger software is composed of several algorithms, each with a large number of parameters. Amongst them are the trigger1D, the trigger3D and the triggerOB. The trigger1D is a one dimensional trigger which searches for correlated hits from a muon in a single direction. The trigger3D is a three dimensional trigger which searches for correlated hits from a muon in many directions by applying the trigger1D in each one of them. The triggerOB is the optical beacon trigger [27]. This algorithm searches for time and position correlations between hits generated by the optical beacon device and the rest of the hits. In this thesis we are mostly interested in the optical beacon trigger for time calibration (see 2.2) of the telescope and the trigger3D for the detection of high energy cosmic neutrinos.

### 2.1.3 Data format

The ANTARES DAQ system uses the ROOT [28] framework to write and read data. All event files are stored into a CVS software repository, the antares-daq. The data frames are organised in structures implemented in C++ classes inherited from ROOT TObject. The data is accessible by mean of the standard STL methods. The timeslices which contain all SPE hits are structured in the class `SPE_TimeSlice`. The physics events are structured in the `PhysicsEvent` class. A physics event contains a list of all SPE hits as well as a list of all hits that made up the cluster that caused the trigger. The data are organised according to the ARS identifier and the data type. Each SPE hit contains information such as the IP address of the frame which depends on the identifiers of the ARS and the PMT that has been hit. Using the Histogrammer package of PhAntOM, the online monitoring system of ANTARES, one-dimensional histograms can be made, such as TVC distributions of SPE hits from physics events (see Section 2.3). The data format is described in the ANTARES internal note [26].

### 2.1.4 The Clock System

The purpose of the clock system is to provide a common timing signal to all front-end chips of the telescope in order to synchronise and control the data flow. This is essential since the timing of the Cherenkov photons hits from muon tracks needs to be determined precisely.

The system consists of a main clock generator on-shore, a clock distribution system made of a bidirectional optical fibre network and a clock signal transceiver in each local control module (LCM). The on-shore master clock system drives the slave clock system in the LCMs. It defines a common frequency for all Analogue Ring Sampler (ARS) chips of the telescope. All clocks are locked to the on-shore reference clock frequency of 20 MHz that corresponds to a time period of 50 ns.

On shore, the reference clock sends a sinusoidal electrical signal which is converted to an optical signal and transmitted to the Junction Box (JB) via the main electro-optical cable (MEOC) that connects the shore to the JB at the ANTARES site. A passive splitter inside the JB distributes the signal to the detection lines of the telescope. In each string control module (SCM), the reference clock signal is regenerated to compensate for the optical power losses along the 40 km long MEOC cable. The signal is then distributed to the individual line sectors and finally to each LCM.

The LCM internal clock register can be reset by an external reset time stamp (RTS) signal from the on-shore master clock which defines the period for all ARS chips. In the LCM the received optical signal is converted into an electrical serial data stream which is transmitted to the six ARS chips. The clock signal is decoded so any associated run command is also made available to the LCM and to all associated front-end chips. The ARS counts the LCM clock periods since the last

reset and provides the arrival time of photons on the PMTs by means of a time stamp (TS) with a resolution of 50 ns that corresponds to the master clock period.

A Time to Voltage Converter (TVC) is used to interpolate between clock pulses. It gives an analogue signal proportional to the precise time of arrival inside the LCM clock period, which is the time between two clock stamps measured with a resolution of 8 bits corresponding to  $50\text{ns} \times (256)^{-1} \approx 0.2\text{ ns}$ . The decoding of the TS and TVC raw data is necessary to obtain calibrated time information. Time offsets between the local slave clocks are induced by differences in the optical path lengths involved in the distribution of the reference clock signal. A precise measurement of the arrival times of Cherenkov photons on the PMTs requires the knowledge of these relative time offsets, which are discussed in the next section.

## **2.2 Relative time calibration**

The angular resolution of ANTARES depends on the relative timing resolution of the photo-multiplier tubes (PMTs) of the telescope. A procedure that can be used for the relative time calibration of a single line of ANTARES is presented in this section. This method was applied to time calibrate the prototype instrumentation line MILOM thus providing preliminary information on the relative time calibration of the entire telescope. An internal ANTARES note [29] describes in detail the results of this relative time calibration.

The method consists of the measurements of the time offsets between the responses of the ARS chips of the line to a flash of the optical beacon. These time offsets are required to correct the time information obtained during normal data acquisition. The optical beacon system is described in Section 2.2.1. The dedicated time calibration procedure using this trigger is described in Section 2.2.2. A calibration procedure for the TVC of the ARS chips is presented in Section 2.2.3.

### **2.2.1 The optical beacon system**

The system used for the relative time calibration of the photo-multiplier tubes (PMTs) consists of a number of optical beacons: several LED Beacons and a laser beacon which can emit short and intense light pulses (few nanoseconds) in the part of the spectrum to which ANTARES is sensitive (350 – 550 nm). The LED beacons are fixed onto the optical module frames (OMFs) at four different locations on each detection line of the telescope. They can illuminate up to 10 storeys of each neighbour detection line. The laser beacon is located on the bottom string socket (BSS) of the instrumentation line. It can illuminate a large part of the bottom half of the telescope. This offers an important redundancy for the time calibration of the photo-multiplier tubes (PMTs) located on the first storeys of every string which are less well-illuminated by the LED beacons.



Besides the laser beacon, the prototype instrumentation line MILOM contained two additional LED beacons, attached to its bottom and top storeys (see Chapter 1). This set up was used to evaluate the time calibration of ANTARES ahead of the full production of the twelve detection lines. The beacons are flashed independently with a frequency of a few hertz emitting a light pulse when receiving a signal from the on-shore clock. The time of emission of the generated light pulses is being recorded by an internal PMT in each optical beacon.

### 2.2.2 Relative time calibration of the MILOM

A dedicated optical beacon trigger is used to find correlations between the direct hits generated by the optical beacon and the other hits. The trigger software searches for frames with an identifier equal to six, which corresponds to an ARS of the Optical Beacon. This ARS is taken as a reference. The calibrated hit time is calculated from the calibrated time to voltage converter (TVC) and the corrected time stamp (TS) values. For more information on the trigger software, we refer to [24] and [25]. The method that was applied to calibrate the TVC of the Analogue Ring Sample (ARS) chip is described in Section 2.3. Triggered SPE hits from physics events are selected by the optical beacon trigger and used to make histograms of the time differences between the ARSs of the optical modules and an ARS of the optical beacon. In figure 2.1 an example of a histogram of the time differences between a particular ARS of an optical module and an ARS of the Optical Beacon is shown. As can be seen from the figure, the distribution shows a clear peak centered on a value close to zero. The fit of a Gaussian distribution with mean  $\mu$  and variance  $\sigma^2$  on top of a flat background distribution is shown in each of the three cases. The fit describes the data well. Typically the mean is less than 0.20 ns and the variance is about 0.30 ns. This result meets the requirements of the ANTARES telescope according to which all electronics and calibration systems should contribute less than 0.50 ns to the overall timing resolution in order to reach the estimated angular resolution of  $0.2^\circ$ .

### 2.2.3 The ARS TVC calibration

#### ARS TVC decoding

The Analogue Ring Sampler (ARS) chip provides sub-nanosecond time information as binary data: a 24 bit time stamp (TS) and a 8 bit Time to Voltage Converter (TVC). The Histogrammer module of the package PhAntOM (cf. 2.3) was used to make TVC distributions. An exemple of the TVC spectrum is shown in figure 2.2. The ARS has two TVCs which are used alternately to interpolate between consecutive clock pulses. The TVC response is assumed to be linear. TVCs operate in pairs to correct for the (dead) time the electronics need to come back from the maximum TVC value to the minimum. As can be seen in figure 2.3, the TVC pe-

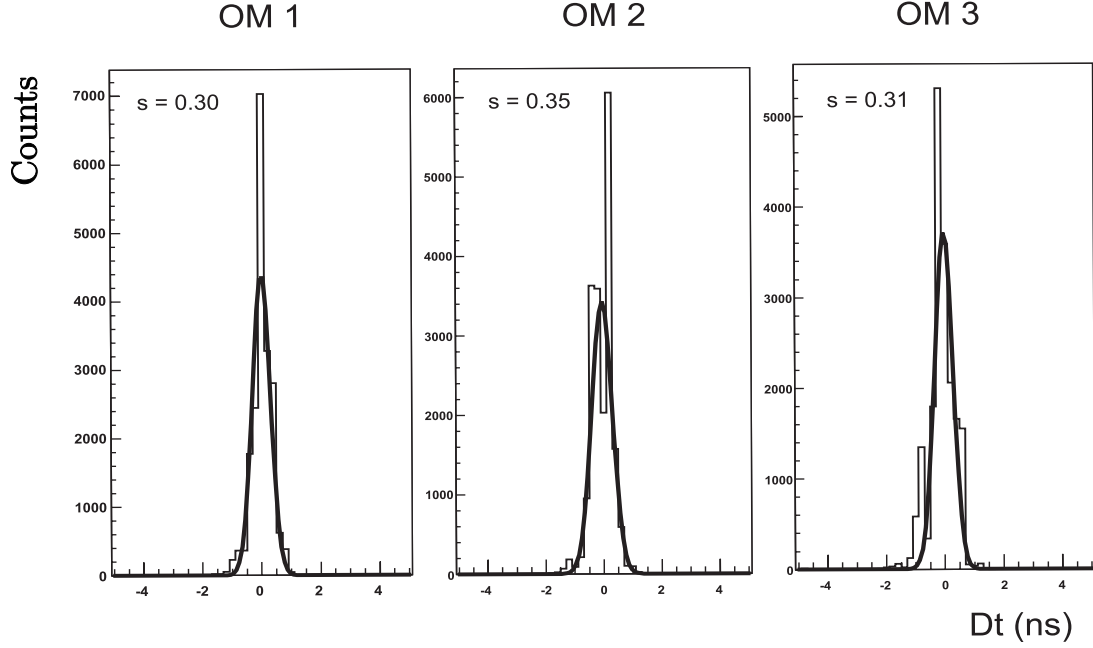


Figure 2.1: Distribution of measured time differences from OMs of the MILOM and the Led Beacon used as reference. The results of a Gaussian fit are shown. Data were taken from the run 13440 with the MILOM.

riod has a positive offset with respect to the clock signal. In order to correct for this offset, both the time stamp and TVC information are needed. Decoding of the time stamp and the TVC values are implemented in the trigger software [25] of ANTARES. For each TVC value, the offset has been determined. Once the time stamp is corrected, the TVC value needs to be calibrated to obtain the hit time. Ideally, the dynamic range of the TVC is 0 to 255. As can be seen in Figure 2.2, in reality the dynamic range is restricted between a lower and an upper bound,  $TVC_{min}$  and  $TVC_{max}$  respectively. A function is needed to translate the TVC binary value into a measure of the time  $t$  in nanoseconds. For TVC values between  $TVC_{min}$  and  $TVC_{max}$ , this function is given as

$$t(\text{ns}) = T_{slope}[0,1](\text{ns/bit}) \times (tvc - TVC_{min}[0,1]) \quad (2.1)$$

with

$$T_{slope}[0,1] = \frac{\text{Clock Period}}{TVC_{max}[0,1] - TVC_{min}[0,1]} \quad (2.2)$$

where  $tvc$  is the value of the TVC. The label 0 or 1 stands for the two TVCs that are part of the ARS. The clock period is set to 50 ns. The two TVC slopes are assumed linear, as is the time transfer function. Hence only the parameter  $T_{slope}[0,1]$  needs to be evaluated for the calibration. The slope can be determined, once we know the dynamic range of the TVC. Between  $TVC_{min}$  and  $TVC_{max}$  there

## 2.2 Relative time calibration

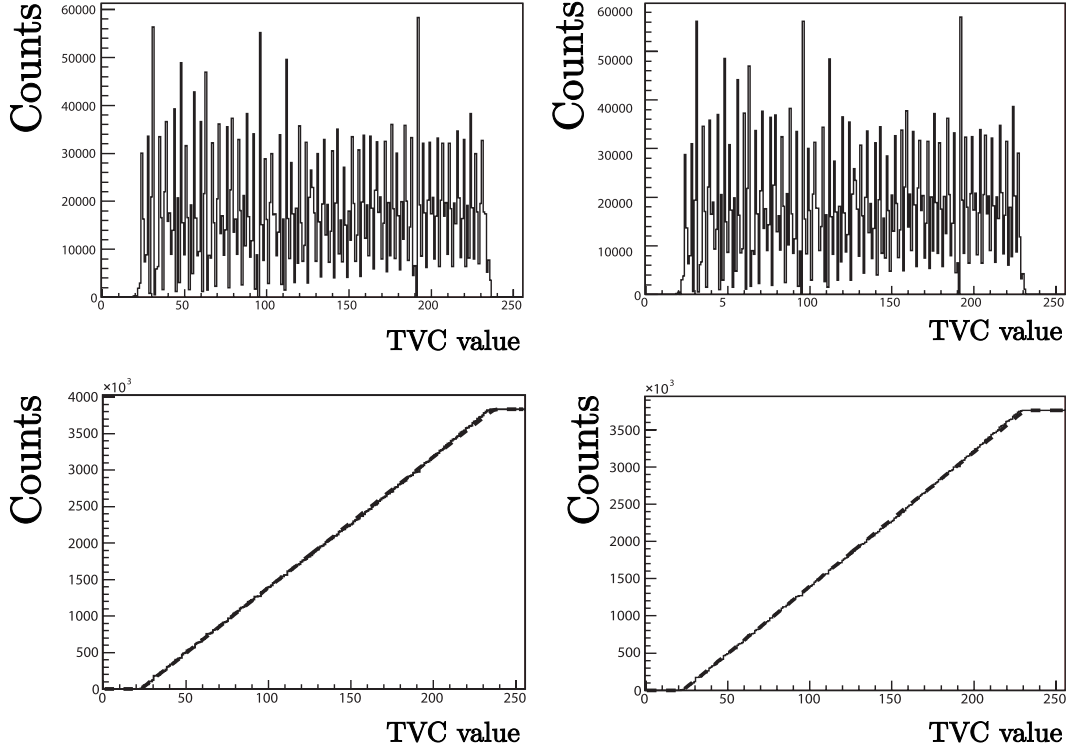


Figure 2.2: Top: raw TVC spectra. Bottom: corresponding integrated TVC spectra and fits, as mentioned in the text. Data were taken with the run 11236 with the MILOM.

is exactly one clock period. Any change of these two extrema will result in the change of the TVC slope. To determine the slope, we calculate the integral of the raw TVC spectrum. The integral of the TVC spectrum from figure 2.2 (top) is also shown in figure 2.2 (bottom). As can be seen from the figure, the integrated TVC signal is indeed a straight line as expected from the transfer function equation 2.1. The fit function corresponds to a straight line between the two points  $(TVC_{min}, 0)$  and  $(TVC_{max}, A)$ , where  $A$  is the normalisation of the histogram. The fit result is shown in Figure 2.2 (bottom). The fit describes the observed distribution well. An internal ANTARES note [30] is dedicated to the calibration procedure of the TVC of the ARS. Runs 11236 through 11262 have been used to study the time stability of the ARS TVC. Data in these runs were collected with the Instrumentation Line shortly after its deployment. The evolution in time of the variables  $TVC_{min}$  and  $TVC_{max}$  of the two ramps of the TVC are shown in figure 2.4. As can be seen in the figure, the ARS TVC dynamic ranges appear to be stable, at least for the period of time during which the runs 11236 through 11262 were taken. The data missing in the different histograms of figure 2.4 correspond to the runs 11248, 11254 and 11246 for which there were no SPE hits recorded.

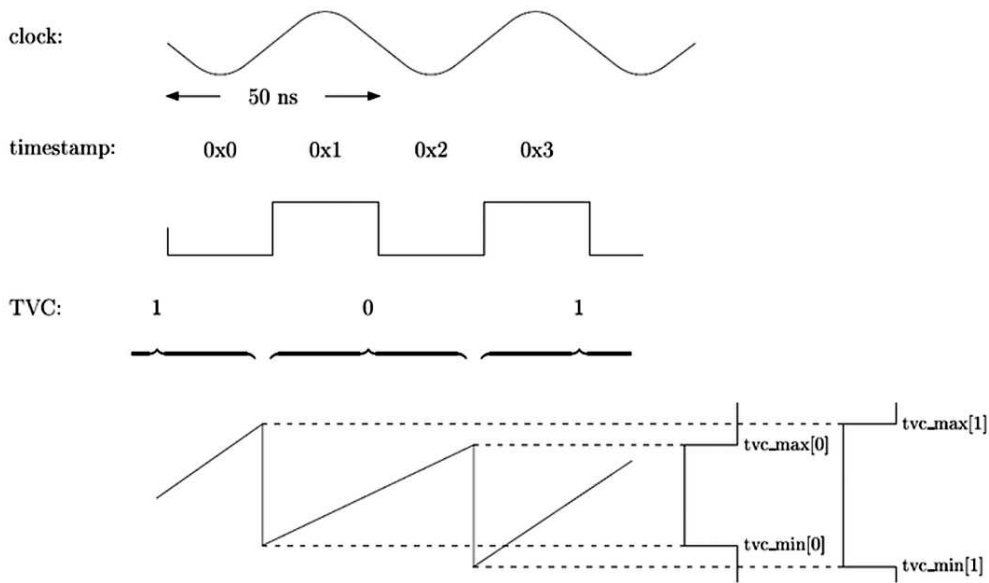


Figure 2.3: Correlations between ARS time stamp (TS) and Time to Voltage Converter (TVC).

## 2.3 The Data Quality Monitoring System

PhAntOM, or “Physics data of ANTARES Online Monitoring” is the data quality monitoring system of ANTARES. The main objective of PhAntOM is to compare ANTARES data with a set of reference histograms, in order to monitor the change in performance of the main components of the telescope during operations. In an internal note [31], it is explained how to use and install the data monitoring package of ANTARES. PhAntOM consists of three complementary software modules: Histogrammer, Comparator, and Histogram Presenter that are described separately in the next sections. A fourth module, Watchdog monitors the operational conditions of PhAntOM. The data flow between the various modules of PhAntOM is represented in figure 2.5. The PhAntOM system has been implemented to operate automatically during data taking with the ANTARES telescope. The Histogrammer module makes one-dimensional histograms of the data. The Comparator module compares one-dimensional histograms from two separate sets, using output files of the Histogrammer for instance. During data acquisition the program automatically compares the recorded histograms with a set of predefined reference histograms. If the histograms are not compatible, an error message is displayed on the screen, and further data analysis will be necessary to identify the cause of this result. The Histogram Presenter features a control panel that allows the analysis of histograms created by the Histogrammer and the Comparator. The Histogram Presenter which can operate on any set of one-dimensional histograms is described in detail in a separate internal note [32].

## 2.3 The Data Quality Monitoring System

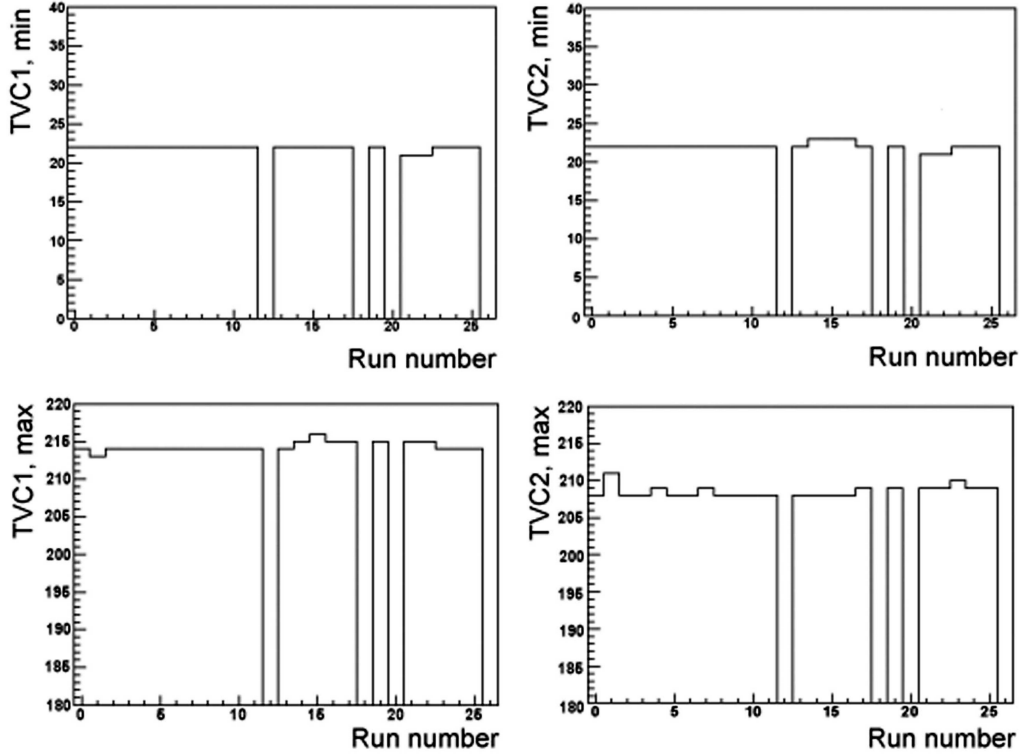


Figure 2.4: Time stability of the dynamic ranges of the ARS TVC. Top:  $TVC_{min}$  spectra of the first and second TVC slope respectively. Bottom:  $TVC_{max}$  spectra of the first ramp and second TVC slope respectively. Data were taken from runs 11236 through 11262 with the MILOM.

In the remaining of this section, the other three modules are described (in Section 2.3.1) and the principles of the so-called Kolmogorov-Smirnov test used in the Comparator are given (in Section 2.3.2).

### 2.3.1 Software Modules

#### Histogrammer

The Histogrammer module consists of several programs dedicated to the physics quantity of interest. The readout system of ANTARES consists of ARSs chips which digitize the charge and the time of the analogue signals of the photomultiplier tubes (PMTs). The Histogrammer can process the different data types produced by the ARS. Examples include the values of the time stamp, the time to voltage converter (TVC) and the amplitude to voltage converter AVC of the physics events. The Histogrammer builds one-dimensional histograms for each of the data types produced by ANTARES. For further analysis the histograms are stored in separate files. The main directory in which the histograms are stored is divided into subdirectories that correspond to the different data types of

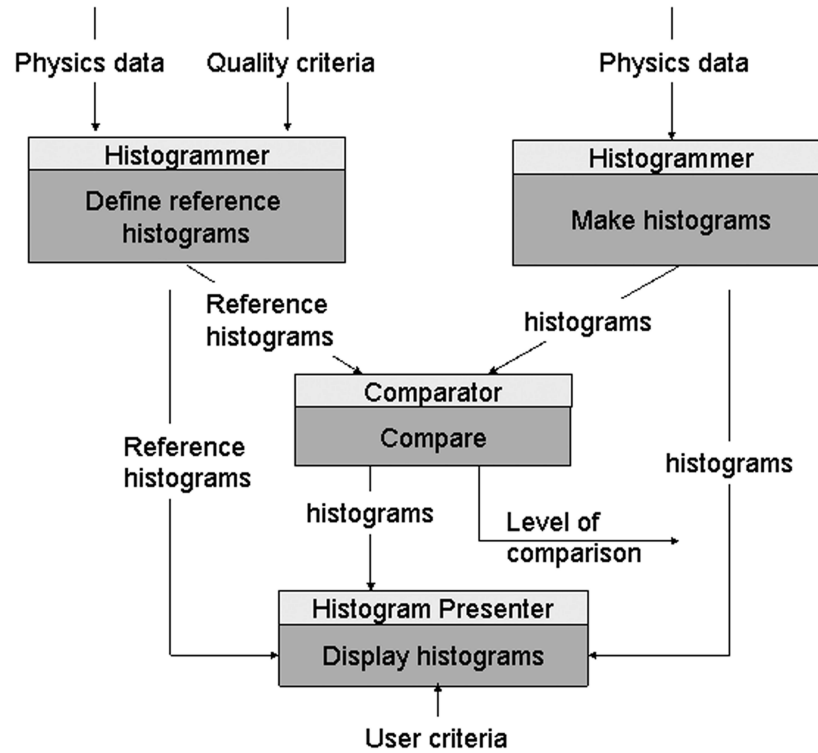


Figure 2.5: Diagram showing the data flow between the different modules of PhAntOM.

ANTARES. These directories are subdivided further into subdirectories, one for each variable of interest.

### Histogram Presenter

The Histogram Presenter is a stand alone program which can be used to manipulate one-dimensional histograms, using a graphical user interface (GUI). The user is free to use the program on any file containing one-dimensional histograms. The Histogram Presenter can also be used to identify a set of reference histograms for further usage by the Comparator. The installation procedure of the software package and the system requirements are described in detail in [32] which also contains a description of the main subpanels and buttons of the Histogram Presenter control window. Via the graphical user interface, histograms can be imported from a file. The user can browse through system directories and file structures to select the histograms and display them on the Histogram Presenter main window. A sample picture of the Histogram Presenter graphical interface is shown in figure 2.6. Once the histograms have been accumulated, they can be edited via a graphical editor. A file selection dialog permits to save the histograms as a picture in any format. A print option is also available. The dis-

played histograms can also be scanned to provide numerical information about the selected histograms.

### Comparator

The main purpose of the Comparator is to compare histograms produced by the Histogrammer package with a set of reference histograms. The program loops over all the input histograms and searches for the corresponding histograms in the reference file taking into account the name, dimension, binning, and number of channels. If the histograms are consistent, two different methods can be applied for the actual comparison: the Kolmogorov-Smirnov test and a bin by bin comparison. Histograms from the input file are compared one by one with the corresponding histograms from the reference file.

The Kolmogorov-Smirnov test is one of the most useful and general nonparametric methods for comparing two data samples, as it is sensitive to differences in both the location and the shape of the empirical distribution functions of the two data sets. The Kolmogorov-Smirnov test is accurate but it is more sensitive at points near the median of the distribution than on its tails. The Kolmogorov-Smirnov test is explained in Section 2.3.2.

The bin by bin comparison is based on the number of standard deviations by which the data from a histogram deviate from the data of a reference histogram. The error per bin  $i$  of an histogram is computed as the square root of the bin's contents  $x_i$ :

$$\sigma_i = \sqrt{x_i}.$$

The standard deviation, which is a measure of the spread or dispersion of a set of data is then defined as:

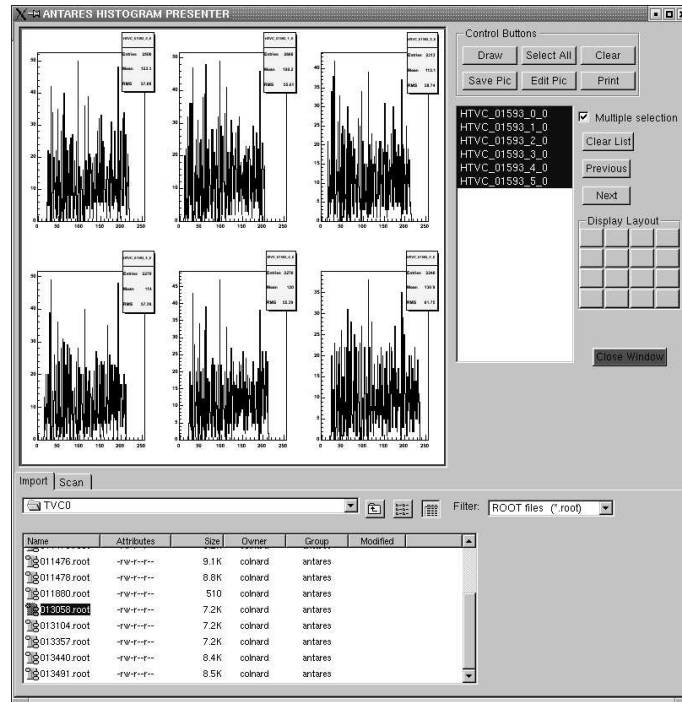
$$\sigma = \sqrt{\sum_i \sigma_i^2}.$$

In the bin by bin comparison test, the standard deviation is deduced from the reference histogram which is considered a perfect description of the true distribution. The difference between the bin contents of a histogram and that of the reference histogram is calculated for each bin  $i$  and compared with the standard deviation  $\sigma$ . As soon as the difference is significant for one bin, the two histograms are considered incompatible.

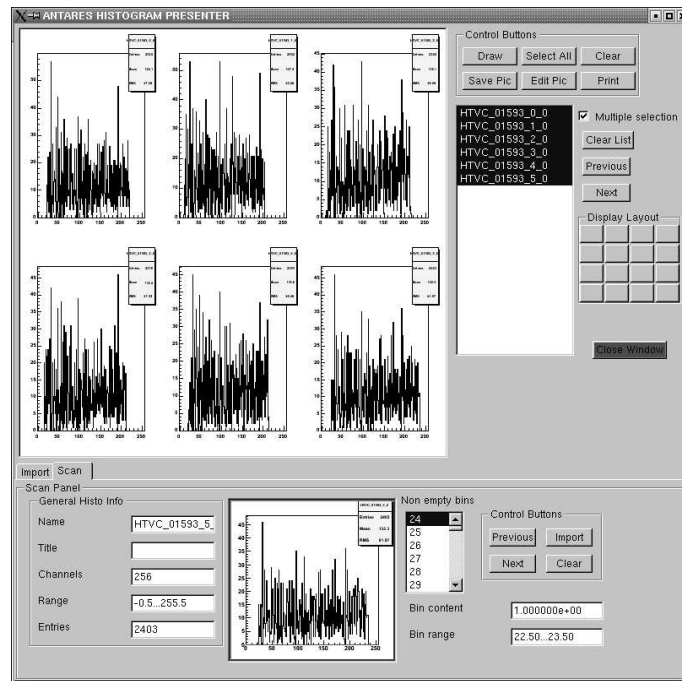
### 2.3.2 The Kolmogorov-Smirnov test

The Kolmogorov-Smirnov test is based on the work of mathematicians Andrey Nikolaevich Kolmogorov and Nikolai Vasilyevich Smirnov for the comparison of two one-dimensional data samples. While the  $\chi^2$  test is designed for discrete distributions and consequently in the continuous case only approximates the test statistic, the Kolmogorov-Smirnow test is designed to compare only continuous

## The ANTARES data acquisition system



(a) The lower panel is switched to the import mode.



(b) The lower panel is switched to the scan mode.

Figure 2.6: Sample picture of the ANTARES Histogram Presenter window.



## 2.3 The Data Quality Monitoring System

distributions of data. The Kolmogorov-Smirnov test is a non-parametric statistical test used to determine whether two independent distributions differ, or whether an underlying distribution function differs from a theoretical distribution, in either case based on finite samples. Non-parametric tests are often used instead of their parametric counterparts when certain assumptions about the underlying population are questionable. For example, the Kolmogorov-Smirnov test does not assume that the underlying population is normally distributed whereas its parametric counterpart, the  $\chi^2$  test does.

The two-sample Kolmogorov-Smirnov test is used to compare two continuous distributions,  $s_n$  and  $s_m$  with respectively  $n$  and  $m$  observations, in order to determine whether the two independent data samples are compatible, i.e. that they originate from the same distribution. The computation of the test involves two empirical distribution functions  $S_N$  and  $S_M$ . The empirical distribution function  $S_N(x)$  is a function of  $x$  which is equal to the fraction of data points that are less than or equal to  $x$  for each  $x \in \mathbf{R}$ . For  $N$  independent data points  $y_1, y_2, \dots, y_N$ , ordered from the smallest to the largest value,  $S_N(x)$  is defined as:

$$\begin{cases} S_N(0 \leq x \leq y_1) &= 0 \\ S_N(y_i \leq x \leq y_{i+1}) &= \frac{i}{N} \\ S_N(x \geq y_N) &= 1 \end{cases}$$

and hence  $S_N(x)$  can be calculated using:

$$S_N(x) = \frac{1}{N} \sum_{i=1}^N n(x_i \leq x)$$

where  $n(x_i \leq x)$  is the number of points for which  $x_i \leq x$ . The empirical distribution is a step function that increases by  $\frac{1}{N}$  at the value of each data point. Kolmogorov suggested in 1933 to estimate the largest distance  $D_{NM}$  between the two empirical distribution functions  $S_N$  and  $S_M$ , by measuring the difference in the y-direction in order to compare the two continuous distributions  $s_n$  and  $s_m$ . If the two samples have been drawn from the same original distribution, the empirical distribution functions of both samples may be expected to be close to each other. This is the null hypothesis  $H_0$ . If the two empirical distributions differ, the samples come from different populations. This is the alternative hypothesis  $H_1$ .

$$\begin{cases} H_0 : S_N(x) = S_M(x) & \text{for all } x \in \mathbf{R}. \\ H_1 : S_N(x) \neq S_M(x) & \text{for at least one value of } x. \end{cases}$$

The distance or test statistic  $D_{NM}$  between  $S_N$  and  $S_M$  for each  $x_i$  is the maximum deviation between the two integrated distribution functions. It is defined as:

$$D_{NM} = \max_{1 \leq i \leq N} |S_N(x_i) - S_M(x_i)|.$$

### *The ANTARES data acquisition system*

Normalized to the total number of entries, the test statistic becomes:

$$T_{NM} = \sqrt{\frac{NM}{N+M}} D_{NM}.$$

The null hypothesis  $H_0$  is rejected if the test statistic  $T_{NM}$  is smaller than a chosen critical value  $\alpha$ , also called the significance level which defines the sensitivity of the test.

Assuming the null hypothesis  $H_0$ , the probability that the Kolmogorov-Smirnov test statistic exceeds a value  $z$  at  $t \leq 0$  converges for large values of  $N$  and  $M$  to the confidence level of the test  $\alpha$  :

$$\lim_{n \rightarrow \infty} P_{H_0} \left( \sqrt{\frac{NM}{N+M}} D_{NM} > z \right) \rightarrow \alpha(z) = 2 \sum_{k=1}^{\infty} (-1)^{k-1} e^{-2k^2 z^2}.$$

The confidence level of the test  $\alpha(z)$  depends on the value  $z$  (see [33]). The relevant critical values  $z$  can be obtained from software programs that perform a Kolmogorov-Smirnov test. In practice the value  $z = 1.36$  is commonly used. This value corresponds to a confidence level  $\alpha(z) = 0.05$  for which the null hypothesis is inadvertently rejected in 5% of the cases when it is in fact true. In the Comparator module, the Kolmogorov-Smirnov test algorithm as implemented in ROOT [28] is used to test the compatibility in shape between two one-dimensional histograms with unbinned data. The returned value is calculated such that it will be uniformly distributed between zero and one for compatible histograms, provided the data are not binned. The result is 1 if the null hypothesis  $H_0$  can be rejected or 0 if it cannot be rejected. If the returned probability is less than the chosen confidence level, the two histograms are not compatible.

## Chapter 3

# Neutrino event generators

*In this chapter two different neutrino Monte Carlo event generators, ANIS and GENHEN are described. These generators are used to simulate neutrinos of all flavors and their interactions in the seabed rock and the water surrounding the neutrino detector ANTARES, in the energy range covered by the telescope. A comparison in performance of both neutrino event generators is presented.*



Monte Carlo simulations are of prime importance when studying the performance of a Cherenkov neutrino telescope as it enables the evaluation of the response of the telescope to neutrino interactions. Two distinct stages of simulation can be recognised: the neutrino event generation and the detector response simulation. Event generators accurately model the neutrino interactions in the media surrounding the Cherenkov neutrino telescope of interest, in the energy range covered by the telescope. The resulting secondary particles, such as muons, are propagated through the surrounding media towards the telescope using separate computer programs or subroutines. Neutrino event generation is the subject of the present chapter. In the second stage, the detector response to the Cherenkov light produced by the secondary leptons within the instrumented volume of the telescope is simulated. This second part is discussed in Chapter 4.

The chapter is organised as follows. In Section 3.1 the general concepts of neutrino event generators are explained. In 3.2 the neutrino generator GENHEN or ‘GENerator of High Energy Neutrinos’ is presented. The neutrino generator ANIS, or ‘All Neutrino Interaction Simulation’ is the subject of Section 3.3. When using ANIS, the produced secondary leptons need to be propagated towards the neutrino telescope using the lepton propagation code MMC or ‘Monte Carlo Muon Code’. MMC is also described in Section 3.3. Both ANIS and MMC

were primarily designed for use within the AMANDA collaboration but the programs have been adapted for ANTARES. A comparison of the performance of the two neutrino generators is presented in Section 3.4.

## 3.1 Event Generators and Propagators

### 3.1.1 Neutrino Generators

#### Neutrino interactions of interest for ANTARES

Neutrino generators are used to simulate neutrino interactions with nuclei and atomic electrons for each of the three neutrino flavors:  $\nu_\mu$ ,  $\nu_e$  and  $\nu_\tau$ . Both channels of the neutrino-nucleon weak interaction, charged current (CC) and neutral current (NC) interactions are supported.

Over the energy range of interest for ANTARES, the interactions of  $\nu_e$ ,  $\nu_\mu$  and  $\bar{\nu}_\mu$  with electrons can generally be neglected in comparison to the neutrino interactions with nuclei since the corresponding cross sections are much smaller than the neutrino-nucleon cross sections at high energies ( $m_e \ll m_N$ ). The reactions  $\bar{\nu}_e e^- \rightarrow W^- \rightarrow \bar{\nu}_\mu \mu$  and  $\bar{\nu}_e e^- \rightarrow W^- \rightarrow (\text{hadrons})$  form important exceptions, as an intermediate  $W^-$  boson is produced which decays in detectable secondary particles [34]. This channel dominates over the  $\bar{\nu}_e$ -nucleon scatterings in a narrow region around the energy of the resonance ( $E_\nu^{\text{res}} \approx 6.3 \cdot 10^6$  GeV) and needs to be taken into account by neutrino generators for high energy neutrinos (and anti-neutrinos). The resonant scattering of anti-neutrinos is named after physicist Sheldon Glashow who discovered this phenomenon. A detailed discussion of this process can be found in [35].

Tau neutrinos in CC interactions with nuclei produce tau leptons which can decay again into tau neutrinos. The secondary tau neutrinos may on their turn interact with nuclei. This is the tau neutrino generation chain. The decay of taus is often simulated in neutrino generators using the package TAUOLA [36] (see Sections 3.2 and 3.3).

#### Predominant interaction

The three neutrino flavors are usually assumed to be produced in their astrophysical sources in the ratio  $\nu_e:\nu_\mu:\nu_\tau = 1 : 2 : 1$ . While propagating from their source over cosmological distances, neutrinos oscillate between the three flavors. This results in a ratio when arriving on Earth of  $\nu_e:\nu_\mu:\nu_\tau = 1 : 1 : 1$  [37]. For muon neutrinos (and muon anti-neutrinos) the detection probability is higher, due to the long absorption length of muons produced in the charged-current (CC) interactions. The primary interaction of interest for the ANTARES telescope is therefore the CC muon neutrino scattering with nuclei.

### 3.1 Event Generators and Propagators

Various scattering processes must be taken into account while generating neutrino interactions with matter: deep inelastic scattering (DIS), quasi-elastic nucleon (QE) scattering, several nucleon  $N$  and  $\Delta$  resonance (RES) channels (with mass values below 2 GeV). In the QE channel of the CC muon neutrino interaction with nuclei,

$$\nu_\mu + N \xrightarrow{CC} \mu^- + N' \quad (3.1)$$

the final nucleon  $N'$  acquires some momentum but remains intact. The nucleon and  $\Delta$  resonance channels are given by

$$\nu_{\mu\mu} + N \xrightarrow{CC} \mu^- + N^* / \Delta \xrightarrow{decay} (\text{hadrons}). \quad (3.2)$$

In this case, a nucleon resonance ( $N^*$ ) or Delta resonance ( $\Delta$ ) is produced that decays into hadrons.

High energy neutrino generators often neglect the QE and RES channels since their contribution is only significant at low energies ( $E \leq 10$  GeV). Hence, the DIS neutrino-nucleon CC-scattering is the dominant interaction of neutrinos (and anti-neutrinos) in conventional matter in the energy range covered by ANTARES ( $E \geq 10$  GeV). The DIS channel of the CC muon neutrino interaction with nuclei can be expressed as

$$\nu_\mu + N \xrightarrow{CC} \mu^- + X \xrightarrow{hadronisation} \mu^- + (\text{hadrons}) \quad (3.3)$$

reflecting the disintegration of the struck nucleon  $N$  into partonic fragments  $X$  that hadronize into various hadrons. Figure 3.1 shows the corresponding Feynman diagram. The outgoing muon is scattered at the interaction vertex over a certain angle. The average angular difference between the initial neutrino direction and the emerging muon direction [24] is bound by the following inequality

$$\bar{\theta}_{\nu-\mu} < \frac{1.5^\circ}{\sqrt{E_\nu(\text{TeV})}} \quad (3.4)$$

where  $E_\nu$  represents the neutrino energy. For muons below 10 TeV, the angular resolution of the neutrino telescope ANTARES is dominated by the  $\nu_\mu$ - $\mu$  scattering angle described by Equation 3.4. Above 10 TeV, detector effects such as the water quality or the timing resolution (relative and absolute) of the photomultiplier tubes prevail. Above 10 TeV, an angular resolution of about  $0.3^\circ$  can be achieved with ANTARES.

#### Propagation through the Earth

Also for the propagation process through the Earth, only DIS interactions are simulated. It is now well established [38] [39] that the deep inelastic CC interaction

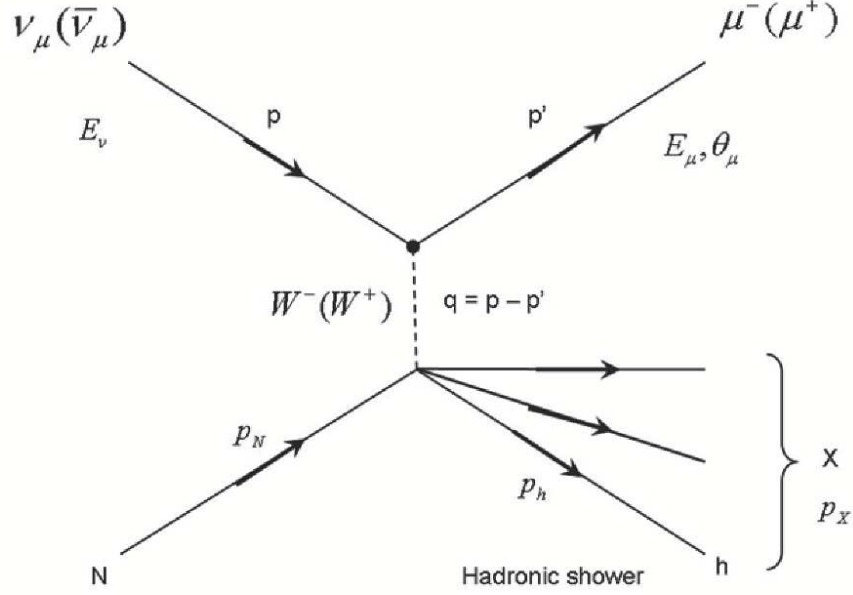


Figure 3.1: Neutrino (or anti-neutrino) deep inelastic scattering (DIS) event. A charged-current interaction between a muon neutrino (or muon anti-neutrino) and a nucleon (proton or neutron) is depicted. The incoming neutrino (or anti-neutrino) creates a  $W^-$  (or  $W^+$ ) boson and turns into a muon. The  $W^-$  interacts with an individual quark within the nucleon, resulting in its disintegration. The struck quark and the remaining two quarks shower into a variety of hadrons, dissipating the large amount of energy transferred to the nucleon.

length for neutrinos in rock is comparable with the diameter of the Earth at approximately 40 TeV. Above this energy, the Earth becomes gradually opaque to neutrinos. Below this energy, the Earth is getting more and more transparent to neutrinos. Deep inelastic scattering with nuclei is therefore also the major source of the attenuation of the neutrino flux while passing through the Earth. Electron neutrinos and muon neutrinos are absorbed in CC interactions and are driven to lower energies in NC interactions. Given the energies involved, QE and RES neutrino-nucleon and interactions can also in this case be safely neglected for the calculation of the neutrino attenuation.

Tau neutrinos are a particular case. They are never absorbed in CC interactions as they regenerate:  $\nu_\tau \rightarrow \tau \rightarrow \nu_\tau$ , as was already mentioned above. The Earth is thus transparent to tau neutrinos at all energies.

To quantify the phenomenon of absorption of the neutrinos in the Earth with more precision, neutrinos are propagated through the Earth using various den-

### 3.1 Event Generators and Propagators

sity profiles which model the interior of our planet. The most widely used density profile is taken from the Preliminary Reference Earth Model [40] [34], which is shown in Figure 3.2. In this model, the Earth consists of concentric spheres with different densities depending on the radial distance  $r$  to the center of the planet.

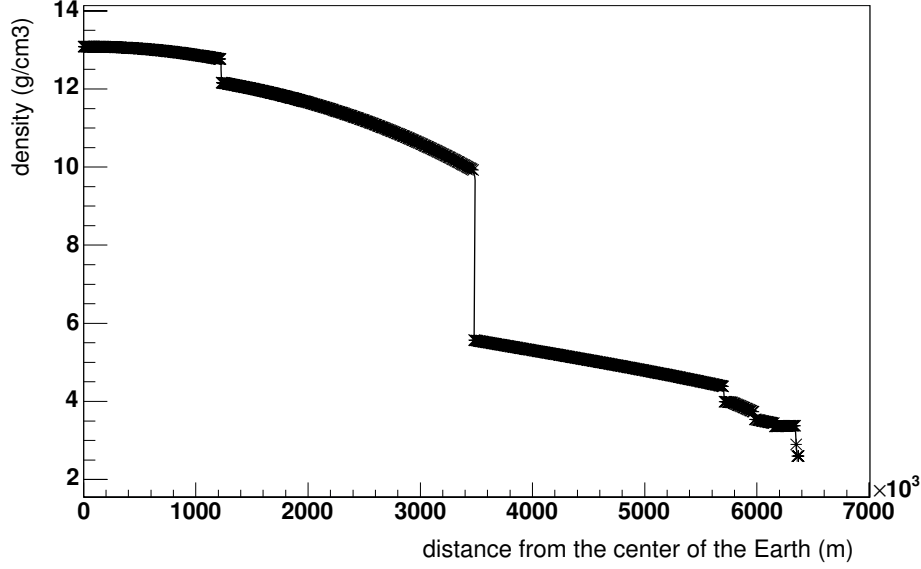


Figure 3.2: *Density profile of the Earth as a function of the distance from the center of the Earth.*

#### Kinematics

The kinematic variables describing the  $\nu_\mu$ - $\mu$  deep inelastic scattering (DIS) are the total center-of-mass energy  $\sqrt{s}$ , the square of the (negative) invariant momentum transfer between the incoming neutrino and the outgoing muon  $Q^2$ , the energy transfer in the target frame  $\nu$ , the Bjorken scaling variable  $x$ , the relative energy transfer or inelasticity  $y$  and the total energy of the outgoing hadrons in their center-of-mass frame  $W^2$ . The basic relations between the kinematic variables are presented in the following equations

$$s = (p + p_N)^2 = 2ME_\nu + M^2 \approx 2ME_\nu \quad (3.5a)$$

$$Q^2 = -q^2 = -(p - p')^2 = -(E_\nu - E_\mu)^2 = 4E_\nu E_\mu \sin^2 \frac{1}{2} \Theta_\mu > 0 \quad (3.5b)$$

$$\nu = \frac{q \cdot p_N}{M} = E_\nu - E_\mu = E_X - M \quad (3.5c)$$

$$x = \frac{-q^2}{2q \cdot p_N} = \frac{Q^2}{2M\nu} \quad \text{with} \quad 0 \leq x \leq 1 \quad (3.5d)$$

## Neutrino event generators

$$y = \frac{q \cdot p_N}{p \cdot p_N} = \frac{\nu}{E_\nu} = 1 - \frac{E_\mu}{E_\nu} = \frac{Q^2}{2ME_X} \quad (3.5e)$$

$$W^2 = E_X^2 - p_X^2 = (E_\nu - E_\mu + M)^2 - (p - p')^2 = -Q^2 + 2M\nu + M^2 \quad (3.5f)$$

where  $E_\nu$  and  $p$  are the energy and the four-momentum of the incident neutrino, respectively.  $E_\mu$  and  $p'$  are the energy and the four-momentum of the outgoing muon. The variables  $q = p - p'$ ,  $p_N$  and  $p_X$  are the four-momenta of the exchanged boson  $W^-$  (or  $W^+$ ), the incoming nucleon  $N$  and the outgoing hadronic final states  $X$ , while  $p_h$  is the four-momentum of one single hadron. The basic kinematic relations (3.5d) and (3.5e) lead to

$$xy = \frac{Q^2}{2ME_\nu} = \frac{Q^2}{s - M^2} \quad (3.6)$$

which shows that for a given energy  $E_\nu$ , DIS neutrino-nucleon scatterings can be characterized by two variables such as  $(x, y)$  or  $(x, Q^2)$ .

## Cross section

To calculate the rate of high energy events in a neutrino detector, the differential DIS neutrino-nucleon cross sections needs to be evaluated in the whole range of the kinematic variables  $0 \leq x \leq 1$  and  $0 \leq Q^2 \leq \infty$ . For an isoscalar nucleus of mass  $M$ , i.e. a nucleus with an equal number of protons and neutrons  $N = \frac{n+p}{2}$ , the leading order electroweak theory predicts the differential cross section for neutrino-nucleon DIS scattering as described by

$$\frac{d^2\sigma}{dx dy} = \frac{2G_F^2 ME_\nu}{\pi} \left( \frac{M_W^2}{Q^2 + M_W^2} \right)^2 [xq(x, Q^2) + x\bar{q}(x, Q^2)(1 - y)^2] \quad (3.7)$$

where  $M_W$  is the mass of the intermediate boson  $W^-$  and  $G_F = 1.16632 \times 10^{-5} \text{ GeV}^{-2}$  is the Fermi constant. This differential cross section is expressed per nucleon and differential in terms of the Bjorken scaling variables  $x$  and  $y$ . It is specific for neutrinos; for anti-neutrinos,  $q(x, Q^2)$  and  $\bar{q}(x, Q^2)$  need to be exchanged.

The hadronic part of the neutrino-nucleon interaction leads to the appearance of the parton distribution functions  $q(x, Q^2)$  and  $\bar{q}(x, Q^2)$  in Equation 3.7. The PDFs represent the probability density for finding a particle with a certain longitudinal momentum fraction  $x$  and momentum transfer  $Q^2$ . The differential cross sections in Equation 3.7 depend on both the PDFs of quarks  $q(x, Q^2)$  and anti-quarks  $\bar{q}(x, Q^2)$ . The known PDFs are obtained by using experimental data [41]. Experimentally determined PDFs are available from various groups worldwide such as the CTEQ [42], MRS/MRST/MSTW [43], H1 [44] and ZEUS [45] [46] collaborations.



### 3.1.2 Lepton propagators

#### Muon energy losses in matter at high energies

Only high energy muons originating from neutrino interactions in matter in or around ANTARES have a range long enough to reach the telescope. As a muon travels through matter it loses energy due to ionization, including delta ray production and excitation processes, bremsstrahlung, photo-nuclear interaction and pair production. The relative importance of these processes depends on both the target material and the muon energy. The process of muon pair production in muon propagation is usually neglected due to the very small cross sections involved [47]. The energy loss of a muon in matter below a few hundred GeV is continuous and dominated by ionisation as described in the Bethe-Bloch relation [48]. The energy transferred to the free electrons during a collision is rather small, but knock-on electrons, also called delta rays can be emitted. At high muon energies ( $E \geq 1$  TeV) the radiative processes become prevalent. In some rare cases, the radiative energy loss can be very large. As this happens only rarely, the energy loss cannot be treated as a uniform and continuous process. Instead, a division between a continuous and a discrete energy loss regime is usually introduced in the lepton propagation programs via an energy cut ( $E_{cut}$ ) and a relative energy loss cut ( $\nu_{cut}$ ) (see Sections 3.2.3 and 3.3.3). Below these cuts all losses are considered as continuous [49]. While  $E_{cut}$  is preferably used in the evaluation of the transport of muons and taus down to the detector location,  $\nu_{cut}$  is applied to simulate the leptons passing through the Cherenkov telescope to obtain the detector response. The energy thresholds are artificial and depend upon characteristics of the muon propagation algorithm but also on the configuration of the detector. The energy thresholds should therefore be chosen carefully in order to get the best accuracy within a reasonable calculation time since the stochastic treatment of the energy can lead to a very large number of separate energy loss events [50].

Bremsstrahlung, also known as decelerating radiation, is electromagnetic radiation which is produced by the acceleration of the muon when deflected by an atomic nucleus. Muons can also radiate a virtual photon which can interact with a nucleus and create a positron-electron pair. This is the direct pair production interaction. Bremsstrahlung and pair production are the dominant processes at high energy ( $E \geq 1$  TeV) as they contribute up to 40% and 50% of the average muon energy loss, respectively. The inelastic interaction of muons can be described via the exchange of a quasi-real photon between the muon and a nucleon. It is often referred to as photo-nuclear interactions of the muons. Its contribution is rather small but it becomes more important at high energy. This process contributes up to 10% of the total energy loss around 1 TeV. The photo-nuclear interaction is essentially a low  $Q^2$  process ( $Q^2 \ll 1 \text{ GeV}^2$ ) and its description is model dependent. Simplifications can be made in the theoretical considerations of the process to obtain convenient and simple formulae for the cross section. The most commonly used are the expressions given by Bezrukov and Bugaev [51] or

Borog and Petrukhin [52] which lead to results agreeing within 10% for the differential cross section and within about 5% for the average energy loss, provided that the same photo-nuclear cross sections are used in the calculations [53].

The total energy loss is determined by the summation of all individual contributions. The average rate of muon energy loss can be described by

$$-\frac{dE}{dx} = a(E) + b(E)E \quad (3.8)$$

with  $a(E)$  the muon energy loss by ionization, and  $b(E)$  the summation of bremsstrahlung, photo-nuclear interaction and pair production. Below 1 TeV, the first term dominates. As can be seen from Equation 3.8 it is (approximately) independent of the muon energy. Above 1 TeV the second term of the equation becomes dominant, where the energy loss is proportional to the energy of the muon.

## 3.2 GENHEN

The Monte Carlo event generator GENHEN generates high-energy neutrino interactions in the media surrounding the instrumented volume of the ANTARES neutrino telescope. An extensive description of the latest version of the program can be found in an ANTARES internal note [54] and a Ph.D. thesis [55]. In Figure 3.3 an example is shown of a diffuse AGN-like flux of muon neutrinos assuming  $E^2\Phi = 10^{-6}\text{GeV cm}^{-2}\text{s}^{-1}\text{sr}^{-1}$  which has been generated with GENHEN. A summary of the main characteristics of the program is given in the following sections.

### 3.2.1 Program summary

GENHEN simulates neutrino and anti-neutrino interactions with conventional matter for high-energy neutrinos up to  $10^9$  GeV. This upper limit on the neutrino energy is due to the lepton propagator programs which are used in GENHEN (see Section 3.2.3). For the propagation of the neutrinos through the Earth, the Preliminary Reference Earth Model [40] [34] is used to calculate the density profile. Details on this Earth model as implemented in GENHEN can be found in [56]. The detector reference system of ANTARES that is used by GENHEN is centered at the center of gravity of the telescope such that  $(x, y, z) = (\text{North}, \text{West}, \text{Up})$  with  $z = 0$  at the seabed level. Straight upward-going (vertical) events are characterized conventionally by a zenith angle  $\Theta = 0$ . Upward-going events therefore have a zenith angle  $\Theta$  such that  $0 \leq \cos(\Theta) \leq 1$ . The code is written in the programming language Fortran [57]. The particle identification numbers follow the scheme used in the GEANT [58] detector simulation program. Since different event topologies require different input conditions to be generated, GENHEN

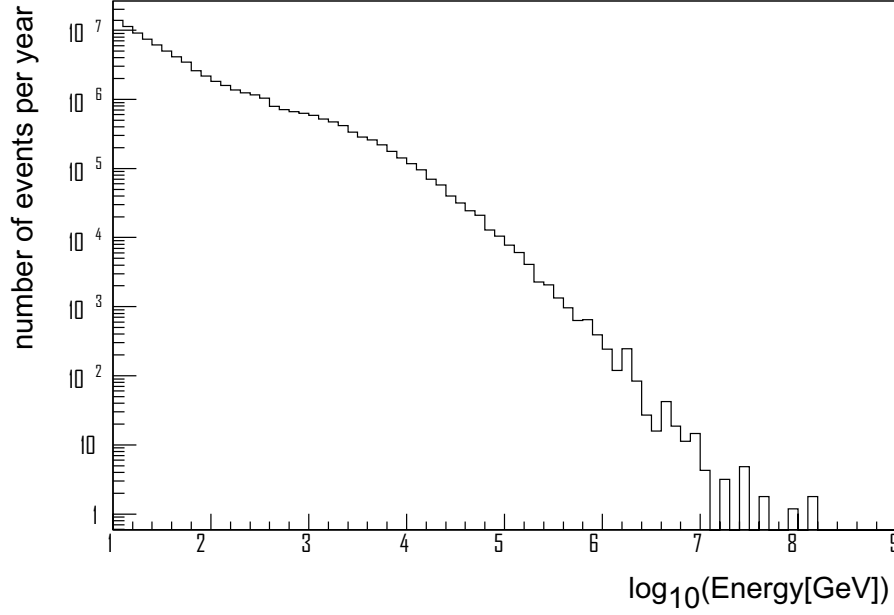


Figure 3.3: Upward-going muon neutrino energy spectrum simulated with GENHEN, assuming a diffuse AGN-like flux with energies between  $10 \text{ GeV}$  and  $10^9 \text{ GeV}$ . Events with a neutrino or secondary muons which could reach the Can were selected for further processing with a detector simulation. Few events can be seen at high energies due to the absorption of neutrinos in the Earth.

simulates one neutrino or anti-neutrino flavor at a time assuming only one type of interaction, essentially to improve the speed of the simulation.

A package based on the Monte Carlo programs LEPTO [59] and RSQ [60] has been implemented to simulate the neutrino interactions [54]. The total cross sections and event kinematics of neutrino-nucleon CC and NC interactions in the matter surrounding ANTARES are computed with the help of LEPTO for the DIS channel. LEPTO integrates the differential cross section given by Equation 3.7 over the full range of neutrino interactions relevant to ANTARES. As the LEPTO program is accurate up to neutrino energies of  $10 \text{ TeV}$ , GENHEN uses an extrapolation of the model to calculate the neutrino-nucleon cross sections and kinematics to generate DIS interactions up to an energy of  $10^9 \text{ GeV}$  [55]. GENHEN uses various parton density parametrizations of the C-TEQ group [42], provided by the library PDFLIB [61] for the DIS channel. The recommended (and used) parametrization is the last tested version CTEQ6D. The nucleon and  $\Delta$  resonant (RES) and the low energy quasi-elastic (QE) parts of the neutrino-nucleon interaction are generated with the program RSQ. GENHEN simulates the Glashow resonance using an internal routine [62].

### 3.2.2 Generation method

#### Geometry

The instrumented volume of ANTARES is represented as a cylinder centered on the center of gravity of the telescope and containing all the photo-multiplier tubes (PMTs). A larger cylinder referred to as the Can<sup>1</sup> encompasses the instrumented volume of the detector. The Can defines the volume within which Cherenkov light is produced in the Monte Carlo detector simulation when evaluating the response of the telescope. The Can is surrounded by a third cylinder: the Generation Volume in which neutrino interactions with nuclei and atomic electrons in the matter surrounding the telescope are simulated. The Generation Volume therefore represents the neutrino interaction volume. This volume ( $V_{gen}$ ) corresponds to the Can expanded with the maximum lepton range in the appropriate medium (rock or sea water) for the maximum value of the energy range ( $E_{max}$ ) to be generated. The range  $R_{max}^l$  (with  $l = \mu, e, \tau$ ) is determined for the simulated neutrino topology assuming that the lepton takes all the neutrino energy [54]. In the downwards direction  $V_{gen}$  is determined by the maximum lepton range in rock ( $R_{max}(\text{rock})$ ). The lower bound of the Can only extends to the seabed as leptons below this point won't be able to produce detectable light. Horizontally  $V_{gen}$  is calculated using the maximum lepton range in sea water ( $R_{max}(\text{water}) \times \cos \theta_{max}$ ) with  $\theta_{max}$  the upper edge of the range of the zenith angle). In the upward direction the extension of the Can is either determined by the maximum lepton range in sea water, or by the sea surface whichever is the smallest for downward-going neutrinos. If upward-going events are simulated, the Generation Volume stops at the top of the Can.

The Can and the Generation Volume are tools used in the generation method. The final result of the simulation should not depend on the details of  $V_{gen}$  or the Can, of course. The generation process is statistical and encompasses the entire generation volume  $V_{gen}$ .

#### Algorithm

The energy  $E$  and the direction of the neutrinos that need to be simulated are chosen to reflect the ANTARES neutrino telescope properties or specific interests of the user. The direction is defined by the zenith angle  $\theta$  and the azimuth angle  $\chi$ . It is sampled uniformly in the cosine of the zenith angle range  $[\theta_{min}, \theta_{max}]$ , and in the azimuth angle range  $[0, 2\pi]$ . For the energy spectrum, only power law spectra of the type  $\phi(E) \propto E^{-\gamma}$  are supported in GENHEN. Such an energy spectrum is motivated by the theory of Fermi shock acceleration (see Introduction) which

---

<sup>1</sup>The default Can which is commonly used in ANTARES simulations was also exploited in this work. It is defined by the lower extend  $dZ_{min} = -278.15$  m, the upper extend  $dZ_{max} = 341.47$  m, and the radial extend  $dR = 266.11$  m).

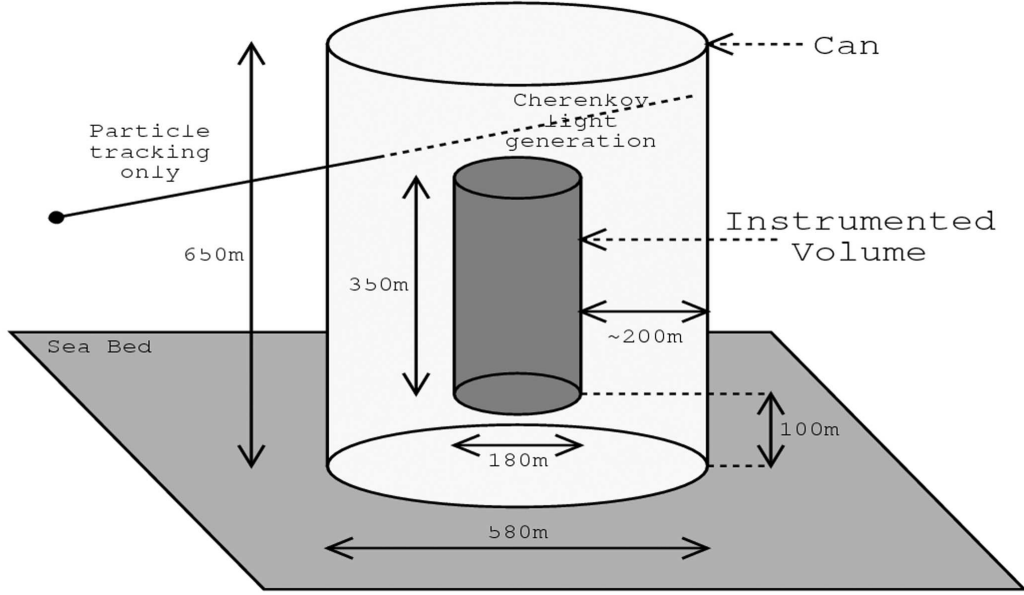


Figure 3.4: Definition of the telescope geometry inside the Monte Carlo event generator GENHEN, including a definition of the “Can”.

is commonly used to describe the production of high energy neutrinos. The energy is sampled in the range  $[E_{min}, E_{max}]$  such that  $E^{-\gamma}$  is uniformly distributed. The event generation in  $E$  and  $\cos\theta$  is therefore made such that the events are uniformly (flat) distributed over phase space.

The energy spectrum from which the events are drawn corresponds either to the flux of neutrinos at the interaction vertex close to the telescope or to the flux of primary neutrinos entering the opposite side of the Earth. A typical value of the spectral index  $\alpha$  is 1.4 for the interacting neutrino flux, as it gives reasonable statistics in all energy ranges. This value corresponds to a spectral index  $\gamma \approx \alpha + 1 = 2.4$  for the neutrino flux at the surface of the Earth <sup>2</sup>. In the case that the drawing spectrum is the primary neutrino spectrum, a full propagation through the Earth is required. If no full propagation through the Earth is performed, the shadowing effect of the Earth is contained in event weights (see next section) in the form of a transmission probability, taking only charged-current (CC) scatterings into account [54]. For a neutrino  $\nu$  with an energy  $E_\nu$  and a zenith direction  $\theta$ , the probability of survival through the Earth or the transmission probability  $P_{trans}$  can be expressed by

$$P_{trans}(E_\nu) = \exp \left[ -N_A \sigma_\nu(E_\nu) \int \rho_\theta(l) dl \right] \quad (3.9)$$

<sup>2</sup>In the energy range covered by GENHEN, the neutrino-nucleon interaction total cross-section is considered to rise linearly with the energy [63] [64].

## Neutrino event generators

with  $N_A$  the Avogadro number,  $\sigma_\nu$  the neutrino CC-cross section, and  $\rho_\theta$  the Earth column depth in the neutrino direction defined by the zenith angle  $\theta$ . This approximation is reasonable for muon and electron neutrinos [54], but NC interactions need to be taken into account when simulating tau neutrinos and their regeneration chain. Therefore a full simulation of the propagation through the Earth is necessary for tau neutrinos.

In order to limit the time required to simulate events within a large range of energies and obtain sufficient statistics at high energies, the total energy range is divided into a number of equal divisions in  $\log_{10}(E_\nu)$ , with  $E_\nu$  the energy of the neutrino. This makes it possible to define a different Generation Volume  $V_i$  for each energy bin  $i$ , and prevent large numbers of events from being generated at low energies in an interaction volume determined by the high energy range.

The number of events  $N_i$  generated in each energy bin  $i$  is calculated by weighting the events with the chosen neutrino generation spectrum

$$N_i(E_i^{min}, E_i^{max}) = N_{gen} \times \frac{\int_{E_i^{min}}^{E_i^{max}} E^{-\alpha} dE}{\int_{E_{min}}^{E_{max}} E^{-\alpha} dE} \quad (3.10)$$

where  $E_i^{min}$  and  $E_i^{max}$  are the extremes of the energy bin  $i$ , and  $E_{min}$  and  $E_{max}$  are the extremes of the entire energy range of the neutrinos to be simulated. In Equation 3.10,  $N_{gen}$  is the total number of events to be generated. As a next step, the number of events  $N_i$  per bin  $i$  is scaled by the ratio of the corresponding Generation Volume  $V_i$  for that bin  $i$  and the entire Generation Volume  $V_{gen}$  corresponding to the total generated spectrum. The obtained value is smeared with a Poisson distribution  $P$  in order to account for the fluctuations in the generated spectrum

$$N_i^{scaled}(E_i^{min}, E_i^{max}) = P\left(N_i \times \frac{V_i}{V_{gen}}\right). \quad (3.11)$$

At initialisation, the GENHEN program computes the interaction cross sections of the neutrinos with the surrounding matter for the topology chosen and initialises the lepton propagation code (see Section 3.2.3). Once the information is available the event loop starts. The energy  $E_i$  of the neutrino is sampled from the chosen generation spectrum. If the propagation through the Earth is not activated, the energy is drawn from the neutrino flux at the interaction vertex close to the telescope, accounting for the different densities of the media around ANTARES. If a full propagation is required, the energy is taken from the neutrino flux at the surface of the Earth. The coordinates and direction cosines of the neutrino interaction vertex are generated uniformly in the Generation Volume  $V_i$  depending on the value of  $E_i$ . If the interaction vertex is generated outside the Can volume, cuts on the distance of closest approach to the Can and the neutrino direction are performed to exclude events with secondaries which will not reach the Can and therefore cannot create detectable light and events with secondaries

that can reach the telescope but with insufficient energy to pass the detection threshold. If the event survives the cuts, or if the vertex is generated inside the Can, the interaction is taking place close to the detector, choosing a specific reaction channel based on the relative cross sections at the sampled energy. If a full propagation through the Earth is required, it is checked whether the event has an energy, vertex and direction that allow the neutrino to make at least one interaction in the propagation through the Earth, otherwise that event is discarded. If the neutrino undergoes a charged current (CC) interaction with nuclei deep in the Earth, the event is discarded as no emerging muon will survive the propagation. If it undergoes a neutral current (NC) interaction with nuclei, the final energy when leaving the Earth and entering the sea water is calculated. This becomes the energy at the interaction vertex close to the telescope.

As was mentioned before, the interaction channel is chosen based on the relative cross sections at the sampled energy. If leptons are produced in the interaction, they are propagated to determine whether they reach the Can, using one of the available lepton propagator programs. If an event contains a neutrino or a lepton which reaches the Can volume, a weight is associated to it, which depends on the energy bin. The event weights are described in the next paragraph and calculated using the prescriptions of References [65] and [66]. The weights are stored along with the events. This can be used to adapt the generated sample and obtain physical spectra. The final energy of the neutrino that propagates through the Earth is also recorded.

### Neutrino event distribution

To obtain a distribution corresponding to a model, specified by a given neutrino flux  $\phi_\nu^{model}(E_\nu, \theta_\nu)$  at the surface of Earth, the sample of generated events needs to be weighted by the ratio of the model neutrino flux to the generated flux. The differential flux of neutrinos (in units of  $\text{GeV}^{-1}\text{m}^{-2}\text{s}^{-1}\text{sr}^{-1}$ ) that is simulated at the surface of Earth <sup>3</sup> can be expressed by

$$\phi_\nu(E_\nu, \theta_\nu) = \frac{N_{gen}}{V_{gen} I_E I_\theta \sigma(E_\nu) \rho N_A E_\nu^\gamma P_{trans}(E_\nu, \theta_\nu) F}$$

where

- $V_{gen}$  (in  $\text{m}^3$ ) is the volume in which the neutrino interactions were generated.

---

<sup>3</sup>The flux corresponding to the events that are generated is the flux of neutrinos arriving at the telescope. The transmission probability through the Earth given in Equation 3.9 needs to be introduced in order to get the flux corresponding to the incoming neutrinos at Earth. If a full propagation through the Earth is simulated, there is no need to introduce the probability of transmission through the Earth in the weights. In this case  $P_{trans}$  is set to 1.

## Neutrino event generators

- $I_E$  (in GeV) is the energy phase factor

$$\begin{cases} I_E = \frac{E_{max}^{1-\gamma_{gen}} - E_{min}^{1-\gamma_{gen}}}{1-\gamma_{gen}} & \text{if } \gamma_{gen} \neq 1, \\ I_E = \ln \frac{E_{max}}{E_{min}} & \text{if } \gamma_{gen} = 1. \end{cases}$$

The energy phase factor results from the integration over the simulated energy range  $[E_{min}, E_{max}]$  in which neutrinos were generated.

- $I_\theta$  (in sr) is the angular phase factor

$$I_\theta = 2\pi(\cos\theta_{max} - \cos\theta_{min}).$$

It results from the integration over the simulated angular range  $[\theta_{min}, \theta_{max}]$ , assuming that the event generation is isotropic. As the solid angle  $\Omega$  is commonly specified by the zenith angle  $\theta$  and the azimuth angle  $\chi$ , the angular distribution is flat in  $\cos\theta$  and  $\chi$ .

- $\sigma(E)$  (in  $\text{m}^2$ ) is the neutrino-nucleus interaction cross section.
- $\rho N_A$  (in  $\text{m}^{-3}$ ) is the number of target nuclei per  $\text{m}^3$ , that is the target density.
- $P_{trans}$  is the probability of transmission through the Earth.
- $F$  is the number of seconds per year.

The weights  $w_i$  to be assigned to each event  $i$  are therefore

$$w_i = \frac{I_\theta I_E E_i^\gamma \sigma(E_i) \rho N_A V_{gen} P_{trans} F}{N_{gen}} \times \phi_\nu^{model}(E_i, \theta_i).$$

In the GENHEN output tags, three types of weight can be distinguished, for each event. The weight  $w1$  (in water equivalent  $\text{m}^3$ ) is the Can volume  $V_{gen}$ . The so-called generation weight  $w2$  (in units of  $\text{GeV m}^2 \text{sr s year}^{-1}$ ) does not depends on the flux model and is expressed as

$$w2 = I_\theta I_E E_i^\gamma \sigma(E_i) \rho N_A V_{gen} P_{trans} F.$$

The global weight  $w3$  (in  $\text{year}^{-1}$ ) is defined as  $w3 = w2 \phi_{atm}$  which corresponds to the generation weight  $w2$  folded with a neutrino flux model  $\phi_{atm}$  to give a rate of events per year. As a default the atmospheric neutrino flux due to Barthol is added to the event weight  $w3$  but other models can be used as well (see [63]). For details on how to use the weights of GENHEN we refer to [67]. GENHEN directly links to the program NUFLUX to simulate the various atmospheric flux models. NUFLUX is described in detail in [66]. For more details on weights, we refer to [68] and [55].



#### 3.2.3 Lepton propagator

GENHEN contains lepton propagation subroutines to calculate the maximum ranges which define the Generation Volume, i.e. the neutrino interaction volume, and the effective ranges that allow to compute effective areas (see Chapter 5). The main role of the subroutines is to propagate the produced leptons from the interaction vertex to the Can of the telescope simulating their energy losses and survival probabilities, including angular and lateral deflections due to multiple scattering.

##### The lepton propagator MUM

Three dedicated lepton propagators, MUM [49], PROPMU [69] and MUSIC [70] are included in GENHEN to calculate the cross sections, free paths and energy losses for lepton interactions and simulate the propagation of the muons over large distances in the media around ANTARES. While MUSIC and PROPMU include the angular and lateral deflections due to multiple scattering, MUM neglects muon scattering. It has been noted, however, that PROPMU is performing badly [71]: substantial numerical differences appear between the simulated and the predicted energy losses (up to 20%) for muon energy between 20 GeV and 10 TeV. MUM is the only lepton propagator available in GENHEN that can also propagate tau leptons, which loose energy differently than muons. The latest version of MUSIC also contains the propagation of taus (with the package TAUSIC), but this version has not yet been included in GENHEN. An ANTARES internal note details the comparison of the three lepton propagators [62]. As can be seen in that paper, MUM and MUSIC give comparable results for the muon propagation through matter, but the MUM algorithm is faster. Because of this, MUM has been chosen as the lepton propagator in this work. In this lepton propagator, the photo-nuclear cross sections according to Bezrukov-Bugaev [51] or the parametrization of the Zeus group [72] can be used. Bremsstrahlung is described according to Bezrukov-Bugaev-Andreev [73] or Koboulin-Kelner and Petrukhin (GEANT 4 [58]). The energy thresholds that determine the continuous and stochastic regimes (see Section 3.1.2 for their definition) are parameters for the initiation procedure of MUM and can be set to any value between  $10^{-4} \leq \nu_{cut} \leq 0.2$  and  $10 \text{ MeV} \leq E_{cut} \leq 500 \text{ MeV}$ . A study of these energy cuts [49] leads to the choice of  $\nu_{cut} = 0.01$  and  $E_{cut} = 10 \text{ MeV}$ .

### 3.3 ANIS: All Neutrino Interaction Simulation

ANIS is a Monte Carlo neutrino event generator for high-energy neutrino telescopes. It has been developed by Marek Kowalski and Askhat Gazizov for the AMANDA collaboration. A full description of the program is given in [74]. In Figure 3.5, an example is shown of a diffuse AGN-like flux of muon-neutrinos

generated with ANIS, assuming  $E^2\Phi = 10^{-6}\text{GeV cm}^{-2} \text{s}^{-1} \text{sr}^{-1}$ . Comparison between Figures 3.3 and 3.5 shows that the ANIS spectrum extends to higher energies. A summary of the properties of ANIS is discussed in the following sections.

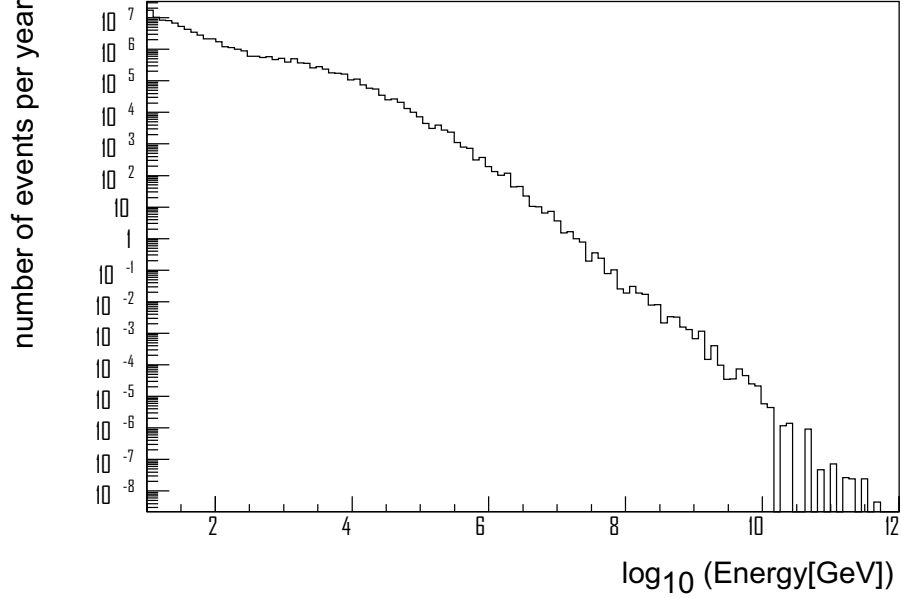


Figure 3.5: Upward-going muon neutrino energy spectrum generated using ANIS, assuming a diffuse AGN-like flux with energies between 10 GeV and  $10^{12}$  GeV. Events with a neutrino or secondary muons which could reach the Can were selected for further processing with a detector simulation. Few events can be seen at high energies due to the absorption of neutrinos in the Earth.

### 3.3.1 Program summary

ANIS can generate neutrinos and anti-neutrinos up to energies of  $10^{12}$  GeV. The program is written in the language C++ which makes it flexible and allows new physics processes to be implemented easily at a later stage. ANIS is independent of any external software package. Instead the program uses pre-calculated tables to provide cross sections for various final states which consist of pairs of the variables  $x$  and  $y$ , and rely on the type of interaction and the flavor of the neutrino that is generated. This makes the program fast and already implemented physics processes can be adapted by only modifying the cross section data in the tables without changing the code. The HepMC [75] Monte Carlo event record and the vector package of the CLHEP library, which is a set of high-energy physics utility classes, are used.

ANIS only simulates deep inelastic (DIS) neutrino interactions with matter as this channel is dominant at the energy range of interest for modern neutrino

### 3.3 ANIS: All Neutrino Interaction Simulation

telescopes. Both charged-current (CC) and neutral-current (NC) scattering are implemented, as well as neutrino interactions with atomic electrons. In the latter case, as was explained in Section 3.2, only the Glashow resonant  $\bar{\nu}_e e^- \rightarrow W^- \rightarrow \text{anything}$  interactions are relevant in the energy range of interest. All produced hadrons are considered to be pions since Cherenkov telescopes cannot distinguish between different types of hadrons.

ANIS also simulates the propagation of neutrinos through the Earth, using a density profile which follows the Preliminary Earth Model [40]. Neutrino absorption in CC scatterings with nuclei and energy loss in NC interactions with nuclei or Glashow scattering with electrons are simulated. The  $\nu_\tau \rightarrow \tau \rightarrow \nu_\tau$  regeneration chain through the Earth is also included with the help of the program TAUOLA [36], which provides data tables with the final products of the decay chain.

Deep inelastic scattering is described using the CTEQ5 parametrization [42] for the parton distribution functions (PDFs). At high energies, up to  $E \leq 10^{12}$  GeV, lepton-quark scattering occurs at small Bjorken  $x$  ( $x < 10^{-5}$ ), where no data exist. In the absence of any reliable PDF parametrization in this domain, extrapolations become inevitable. ANIS uses two approaches founded on different theoretical models that provide an extrapolation of the nucleon structure functions to small  $x$  and large  $Q^2$ : one is based on the CTEQ5 parametrization and the other one on a non-standard hard pomeron enhanced model [76] inspired by A. Donnachie and P.V. Landshoff [77]. In Figure 3.6 the DIS neutrino-nuclear cross sections for CC and NC interactions for the two high energy extrapolations are compared.

Starting from the neutrino-nucleon interaction vertex, secondary muons and taus have to be propagated further towards the telescope using a dedicated lepton propagation program. ANIS does not include such a program but the muon propagator MMC [50] can be used to propagate the secondary muons towards the telescope. A description of the program MMC and its interface with the ANTARES software is given in Section 3.3.3.

The detector reference system in ANIS is centered at the center of gravity of the telescope. The coordinate system is right-handed with the x-axis directed eastward and the z-axis pointing away from the Earth center. By convention straight downward-going (vertical) events are characterized by a zenith angle  $\Theta = 0$ . Upward-going events therefore have a zenith angle  $\Theta$  such that  $-1 \leq \cos(\Theta) \leq 0$ .

#### 3.3.2 Generation method

##### Geometry

In ANIS, neutrinos that survived the propagation through the Earth are simulated to interact within a rotating cylinder whose z-axis is parallel to the neutrino direction, which is referred to as the Final Volume. The Final Volume is centered

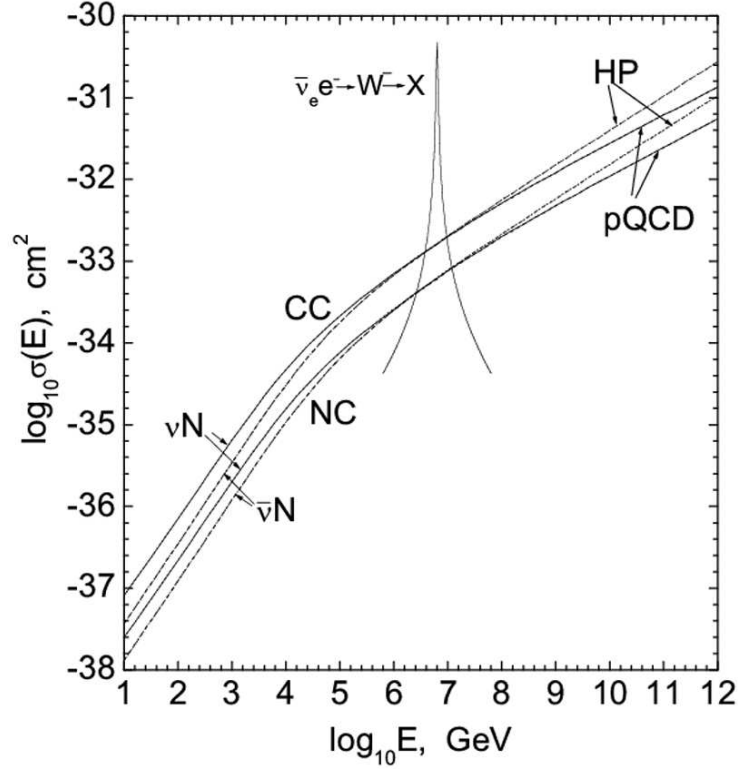


Figure 3.6: Differential neutrino-nucleon cross sections (in  $\text{cm}^2$ ) used by ANIS. Both NC and CC  $\nu - N$  interactions are represented. At high energy ANIS uses an hard-pomeron enhanced model (HP) or an extrapolation of the CTEQ5 parametrization (pQCD). Both neutrino (solid line) and anti-neutrino (dashed) cross sections are shown [74]. The resonant  $\bar{\nu}_e e^-$  reaction is also shown.

on the center of gravity of the telescope and two heights are defined: a positive height in the target region of the original neutrino-nucleon interaction and a negative height in the detector region. The size of the interaction volume is optimized by extending the positive height in the direction of the neutrino-nucleon interaction using the maximum muon range at the considered energy (currently this option is only available for muon neutrinos). The Final Volume is an auxiliary concept used in the generation method. Since it is defined for each event, it makes the generation process dynamic, but the final results should not depend on it.

### Algorithm

Initially, the energy  $[E_{min}, E_{max}]$  and directional ranges  $[\cos \theta_{min}, \cos \theta_{max}]$  (with  $\theta$  the zenith angle) of the neutrinos are chosen, together with the type of generation spectrum. Only power law spectra  $F(E) \propto E^{-\alpha}$  are supported, but other

### 3.3 ANIS: All Neutrino Interaction Simulation

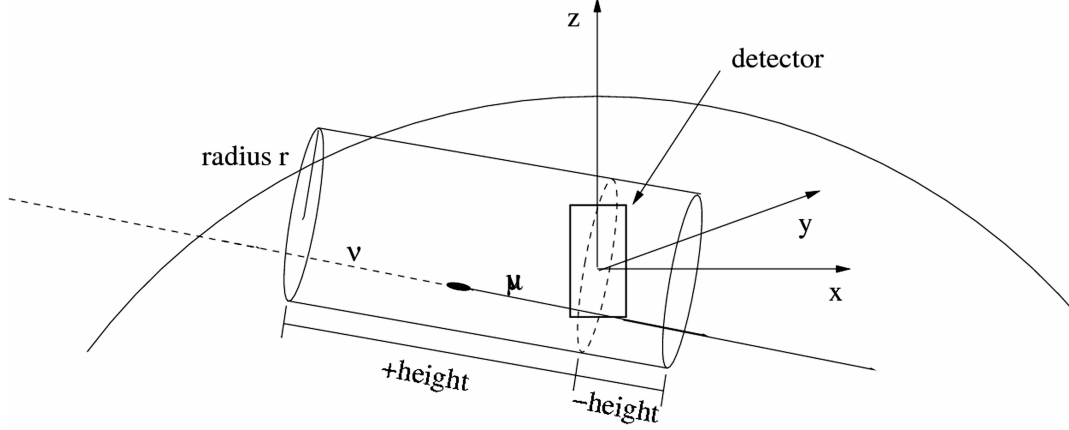


Figure 3.7: Definition of the telescope geometry assumed by the Monte Carlo event generator ANIS. The geometry is anchored to the detector center of gravity. A cylindrical Final Volume is defined for each neutrino event. The axis of the Final Volume is parallel to the direction of motion of the neutrino [74].

types could be added at a later stage. Neutrinos are generated uniformly on the surface of the Earth. Their energy is sampled from the chosen power law spectrum. Neutrinos are subsequently propagated through the Earth in small steps towards the telescope. Neutrinos that survive the propagation through the Earth are simulated to interact within the Final Volume.

All generated events are recorded or sampled according to their interaction probability. If all events are written to output, they need to be properly weighted in order to obtain distributions of physics variables. The weights used in ANIS for this purpose are defined below.

#### Neutrino event weights

Four event weights are defined in the program to produce a physical spectrum of the events once weighted with their interaction probability. These weights include a normalization constant  $W_{norm}$ , the interaction probability in the Final Volume  $P_{int}$  and two weights,  $R_{atm}^{v_e}$  and  $R_{atm}^{v_\mu}$ , that correspond to the atmospheric neutrino flux for electron and muon neutrinos. A detailed description of these weights and a tutorial on how to use them can be found in [74]. Here a brief description of these weights is given. The normalization constant  $W_{norm}$  (expressed in  $\text{GeV cm}^2 \text{ sr s year}^{-1}$ ) is computed as

$$W_{norm} = \frac{I_\Omega \times I_E \times F \times A_{gen}}{N_{gen}}$$

where

### Neutrino event generators

- $N_{gen}$  is the total number of generated neutrinos,
- $A_{gen}$  (in  $\text{cm}^2$ ) is the surface of the cross section of the Final Volume with the detector instrumented volume,
- $F$  is the number of seconds per year,
- $I_E$  is the energy phase factor. It is defined as

$$\begin{cases} I_E = \frac{E_{max}^{1-\gamma_{gen}} - E_{min}^{1-\gamma_{gen}}}{1-\gamma_{gen}} & \text{if } \gamma_{gen} \neq 1, \\ I_E = \ln \frac{E_{max}}{E_{min}} & \text{if } \gamma_{gen} = 1. \end{cases}$$

$I_E$  is given in units of giga electron-volt (GeV).

- $I_\Omega$  is the angular phase factor. It is defined as

$$I_\Omega = 2\pi(\cos\theta_{max} - \cos\theta_{min}).$$

$I_\Omega$  is given in units of steradian (sr).

The normalization constant is chosen such that the event rate per year  $R$  is given by

$$R = W_{norm} \sum_{i=1}^{i=N_{gen}} P_{int,i}.$$

The probability of interaction  $P_{int}$  (dimensionless) inside the Final Volume is defined as

$$P_{int} = 1 - \exp(-\sigma_{tot} \times \tau)$$

with  $\sigma_{tot}$  the neutrino total cross section for the event, and  $\tau$  the column depth. The atmospheric weights  $R_{atm}^{ve}$  and  $R_{atm}^{vm}$  (dimensionless) are defined as

$$R_{atm}^{ve/vm} = \frac{F_{atmo}^{ve/vm}(E, \theta)}{F_{gen}(E, \theta)}$$

with  $F_{atmo}(E, \theta)$  ( $\text{GeV}^{-1} \text{cm}^{-2} \text{sr}^{-1} \text{s}^{-1}$ ) the differential atmospheric flux for electron or muon neutrinos, and  $F_{gen}(E, \theta)$  ( $\text{GeV}^{-1} \text{cm}^{-2} \text{sr}^{-1} \text{s}^{-1}$ ) the generated differential flux at the surface of the Earth. The atmospheric neutrino flux contained in  $R_{atm}^{ve}$  and  $R_{atm}^{vm}$  has been derived from the Volkova flux using the Lipari parameters [78]. ANIS uses pre-calculated tables with the atmospheric neutrino flux data. The procedure on how to use these weights is described in detail in [74]. An example on how to use ANIS for simulating a neutrino flux in ANTARES is given in appendix A.

### 3.3.3 The Muon Propagator MMC

The muon propagator MMC propagates secondary charged leptons and neutrinos from neutrino-nucleon interactions towards the telescope. The program takes into account ionization losses, bremsstrahlung, photo-nuclear interactions and pair production, including effects such as Landau-Pomeranchuk-Migdal (LPM) and dielectric suppression, decay and Molière scattering. Several parametrizations for bremsstrahlung and photo-nuclear cross sections are available. All particles which have been produced during the propagation are also propagated until they disappear or exit the detector volume.

MMC can propagate leptons with energies from their rest mass up to  $10^{30}$  eV, using extrapolations of the known cross sections at high energies. A full description of the program is given in [50]. MMC has been originally developed by Dmitry Chirkin for the AMANDA telescope. The program is written in the object-oriented language Java with a C++ interface to improve the flexibility and readability of the code. The current version of MMC (at the time of the writing of this thesis), i.e. version 1.4.6, contains the water properties at the ANTARES site so that ANIS and MMC can be used in the full ANTARES Monte Carlo chain. An example on how to use MMC for simulating a neutrino flux in ANTARES is given in appendix B.

#### Use of MMC for the ANTARES telescope

MMC can be used to propagate the secondary muon and tau leptons created at the neutrino vertices by ANIS towards the Can<sup>4</sup> of the ANTARES telescope. As can be seen in Figure 3.8 the sea water at the ANTARES site is divided in three regions: one from the surface of the sea to the point where the track of the muon enters the cylindrical Can around the telescope. The second region starts here and ranges to the point where the muon trajectory exits the Can, while the rest of the track lies in the third region. We assume that the relative energy loss cut  $\nu_{cut}$  and the energy cut  $E_{cut}$  are interchangeable and related by  $E_{cut} = \nu_{cut} \cdot E_{\mu}$ , where  $E_{\mu}$  is the energy of the propagated muon. The muons are propagated for a fixed  $\nu_{cut}$  or  $E_{cut}$  through the medium until the particle reaches a point where it loses an energy  $\Delta E_{\mu}$  that is more than the cutoff energy  $\Delta E_{\mu} \geq E_{cut}$  or  $\nu = \Delta E_{\mu} / E_{\mu} \geq \nu_{cut}$ . By default, in the first region, the muon relative energy loss cutoff is taken to be  $\nu_{cut} = 0.05$  (dimensionless). In the second region the absolute energy cutoff is fixed at  $E_{cut} = 500$  MeV, and finally in the third region the muon is propagated in one step with a relative cutoff of  $\nu_{cut} = 1$  (all loss is continuous) to the point where it is lost. Only secondaries and interactions in the second region are recorded into the output. For more details on the implementation of the ANTARES main characteristics in MMC, see appendix B.

---

<sup>4</sup>As defined in Section 3.2.

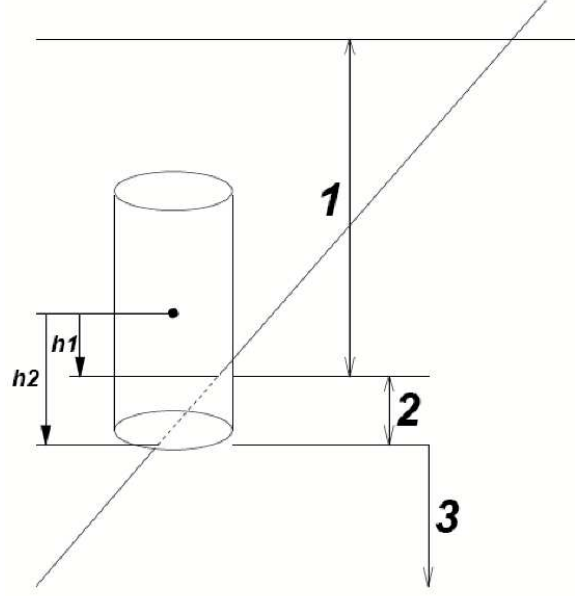


Figure 3.8: Geometry used by the muon Monte Carlo propagator MMC [50] to propagate leptons through the media towards the ANTARES telescope. There are three propagation regions before the detector (the propagation is done with a fixed  $v_{cut}$ ), inside the detector (the propagation is done with fixed  $E_{cut}$ ), and after the detector (fast propagation with  $v_{cut} = 1$ ).

### Comparison with the ANTARES lepton propagator MUM

The performance of MMC has been compared with that of the lepton propagator MUM for the same settings ( $v_{cut} = 10^{-3}$ , ZEUS [72] parametrization of the photo-nuclear cross sections and Bezrukov-Bugaev-Andreev [73] parametrization of bremsstrahlung) for both standard rock and water. Figure 3.9 shows the final energy distributions of  $5 \times 10^5$  muons with initial energy 100 TeV which were propagated through 1 km of water, calculated by MMC and MUM. The details of this comparison can be found in [50]. As can be seen in the figure, both programs give comparable results. The same settings were used in the framework of this thesis for the comparison of GENHEN(+MUM) and ANIS(+MMC) for the ANTARES telescope, described in the following section.

## 3.4 Comparison between ANIS and GENHEN

### 3.4.1 General differences

Both ANIS and GENHEN are Monte Carlo (MC) event generators for neutrino Cherenkov telescopes. While GENHEN has been developed specifically for AN-



### 3.4 Comparison between ANIS and GENHEN

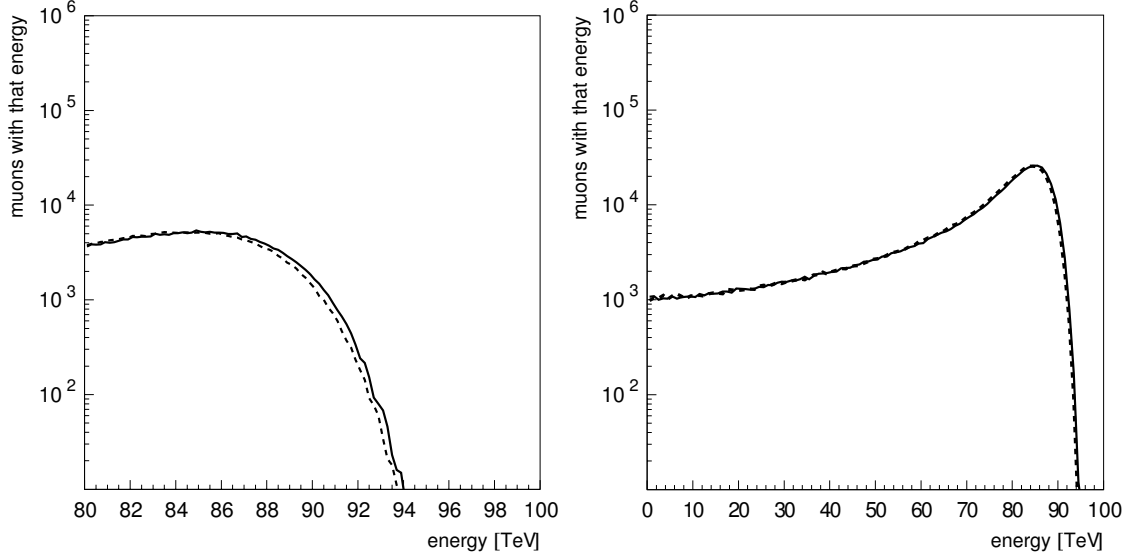


Figure 3.9: Comparison of the final energy distributions of 500000 muons with initial energy 100 TeV which were propagated through 1 km of water, calculated by MMC (solid line) and MUM (dashed) with the same parametrizations of all cross sections and value of energy cutoff ( $v_{cut} = 1 \cdot 10^{-3}$ ). Left: a close-up of the picture on the right [50].

TARES, ANIS can be used for any high-energy neutrino Cherenkov detector. Both algorithms can generate neutrinos of all flavors ( $\nu_e, \nu_\mu, \nu_\tau$ ), taking into account all relevant interactions with atomic nuclei and electrons. GENHEN can simulate neutrino events up to  $10^9$  GeV which is the usual energy range of interest for neutrino telescopes of the size of ANTARES. ANIS can generate events up to  $10^{12}$  GeV with special emphasis on the simulation of the highest energy neutrinos. For this reason, quasi-elastic (QE) and resonant (RES) interactions are neglected in ANIS, while they are properly accounted for in GENHEN. Note that these processes are only relevant at low energies ( $E < 10$  GeV).

GENHEN is written in the language Fortran whereas ANIS has been implemented in C++. The use of the C++ programming language makes the ANIS code fast and more flexible. GENHEN uses the ANTARES Monte Carlo event libraries while ANIS does not link to any library that is specific to a given detector. ANIS uses the HepMC and Vector packages of the CLHEP library to record the neutrino events energies, positions and directions.

The neutrino-nucleon interaction cross sections are described in ANIS using a parametrization for deep inelastic (DIS) scattering based on the CTEQ5 parametrization, whereas GENHEN can use various parametrizations of the CTEQ group [42]. In the framework of this thesis, CTEQ6, which is the latest parametrization available was used. As can be seen in Figure 3.10, there is a small dif-

ference between the cross sections calculated with the CTEQ5<sup>5</sup> and the CTEQ6 parametrizations for neutrinos with energies in excess of  $10^8$  GeV.

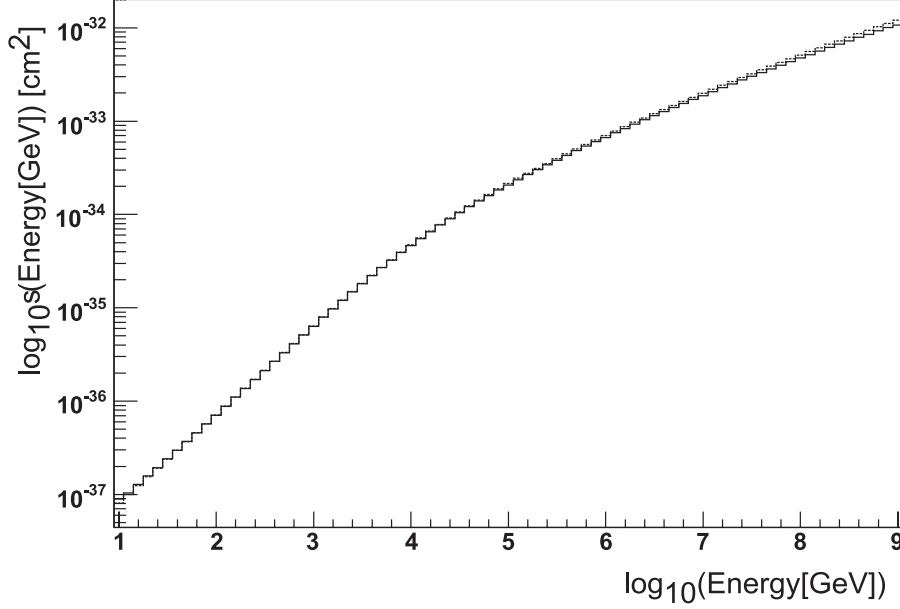


Figure 3.10: *Differential neutrino-nucleon cross sections for the deep inelastic (DIS) channel of the charged-current (CC) interaction for the CTEQ6 parametrization (solid line) and the ANIS results based on the CTEQ5 parametrization (dashed).*

Both ANIS and GENHEN generate neutrinos which follow a power law spectrum  $E^{-\gamma}$  (with  $\gamma$  the spectral index) at the surface of Earth. While in GENHEN fluxes are described in the unit  $\text{GeV}^{-1} \text{m}^{-2} \text{sr}^{-1} \text{s}^{-1}$ , ANIS uses  $\text{GeV}^{-1} \text{cm}^{-2} \text{sr}^{-1} \text{s}^{-1}$ . In order to compare event rates produced with ANIS and GENHEN, fluxes and atmospheric weights in GENHEN have been scaled with a factor  $10^4$  to convert square meters into square centimeters.

GENHEN generates either neutrinos or anti-neutrinos for each run, while ANIS simulates 50% neutrinos and 50% anti-neutrinos. For ease of comparison, the ANIS code has been modified such that either neutrinos or anti-neutrinos are exclusively produced, similar to GENHEN.

GENHEN generates either charged-current (CC) or neutral-current (NC) neutrino interactions with nuclei for each run, while ANIS simulates both interaction channels. Only CC or NC events have therefore been selected with ANIS, after production for comparison with GENHEN. It is also possible to combine two runs of GENHEN with CC and NC events and to renormalize them, in terms of generated numbers of events so they can be compared with ANIS. In this thesis, the first method was chosen.

<sup>5</sup>In this comparison, the known anomalous behaviour of CTEQ5 (at very small  $x \leq 10^{-6}$ ) has been overcome [74]. ANIS uses two different extrapolations for small  $x$  and large  $Q^2$  in order to correct for this anomaly in the CTEQ5 distribution sets.

### 3.4 Comparison between ANIS and GENHEN

ANIS only simulates DIS neutrino scattering with nuclei as the program focus on high energy neutrinos. Since GENHEN also generates the QE and RES channels, only DIS events have been selected after they were produced for comparison with the results of ANIS. When GENHEN propagates neutrinos through the Earth, only the DIS channel is simulated as absorption is important only at high energies.

#### 3.4.2 CPU time Comparison

The Linux time command is used to acquire timing information about the high-energy neutrino event generators GENHEN and ANIS. The speed of both programs depends on the range of energies chosen and the drawing spectrum. On a single Linux machine (Intel(R) Pentium(R) 4 CPU 2.80 GHz)  $10^5$  muon neutrinos have been generated with GENHEN and ANIS, assuming a flux  $F(E) = E^{-2}$  at the surface of the Earth. Only Charged Current (CC) interactions at the neutrino-nucleon interaction vertex close to the detector are taken into account. All events are written to disk. The system CPU time used by the two programs are shown in Table 3.1. Since GENHEN is often used without the full simulation of the Earth for muon neutrinos, timing statistics for a run performed without the full propagation through the Earth are also shown. The amount of time

Software	Number of events at the Can	Generation time
ANIS	44589	43' 48.75
GENHEN	31095	49' 27.53

Table 3.1: CPU usage of ANIS and GENHEN for the generation of  $10^5$  up-going events. The number of events with a neutrino or secondary muons which could reach the Can of the telescope are also given.

required for the simulation using ANIS is somewhat smaller compared to that required using GENHEN while it generates substantially more events at the detector. This is caused by the fact that GENHEN includes the propagation of the produced leptons towards the telescope, while ANIS does not include this process. However, the lepton propagator MMC which is used in conjunction with ANIS, takes only about 5 minutes to propagate the secondary muons produced in DIS neutrino-nucleon interactions with ANIS. ANIS in association with MMC is therefore slightly faster than GENHEN. This can be attributed to the use of pre-calculated tables which implies that ANIS does not need to make a link to any other package for tau decay simulation, cross section and atmospheric flux calculations. We conclude that ANIS and GENHEN require roughly an equal amount of CPU time per event generated.

### 3.4.3 Event rate comparison

To compare the output of both codes,  $10^5$  upward-going muon neutrinos were generated with ANIS assuming an  $E^{-1}$  power law spectrum at the surface of Earth.

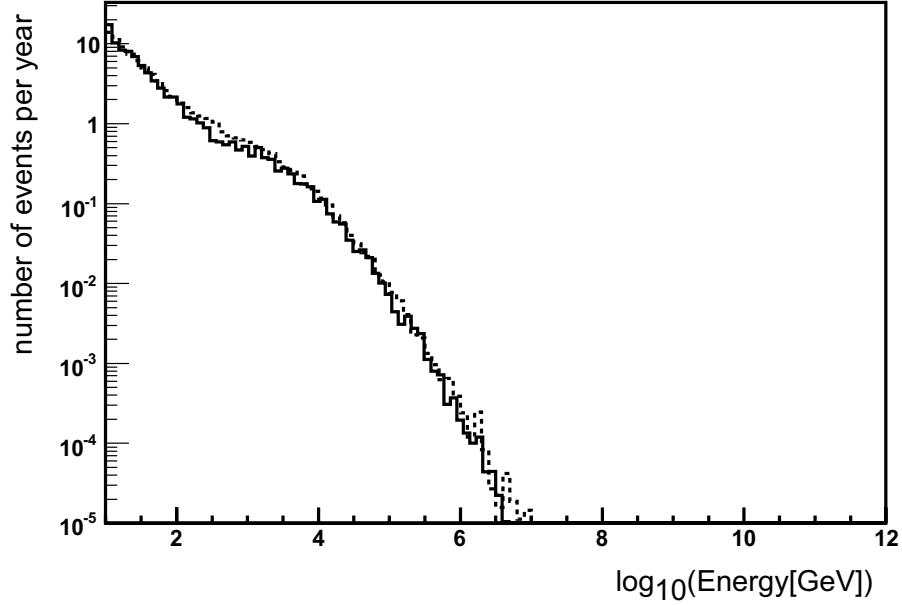


Figure 3.11: Upward-going muon neutrino rates simulated with GENHEN (dashed) and ANIS (solid line), assuming a diffuse AGN-like spectrum, for energies between  $10$  and  $10^9$  GeV. Only events with a neutrino or secondary muons which could reach the telescope are displayed.

The produced muon secondaries were propagated towards the Can of the ANTARES telescope using the lepton propagator MMC and re-weighted to a diffuse AGN-like neutrino flux  $E^2\Phi = 10^{-6} \text{GeV cm}^{-2}\text{sr}^{-1}\text{s}^{-1}$  at the surface of Earth. In parallel  $10^9$  upward-going muon neutrinos were generated with GENHEN, assuming an  $E^{1.4}\Phi = \text{GeV m}^{-2}\text{sr}^{-1}\text{s}^{-1}$  power law interacting spectrum. The produced muon secondaries were propagated towards the Can of ANTARES using the lepton propagator MUM and were re-weighted to a neutrino flux  $E^2\Phi = 10^{-6} \text{GeV cm}^{-2}\text{sr}^{-1}\text{s}^{-1}$  at the surface of Earth.

In Figure 3.11, only charged-current (CC) neutrino interactions of the deep inelastic (DIS) channel are shown, with events occurring inside or at the Can and events with a secondary muon which could reach the Can. This event selection is done automatically with GENHEN as the program provides an option which

### 3.4 Comparison between ANIS and GENHEN

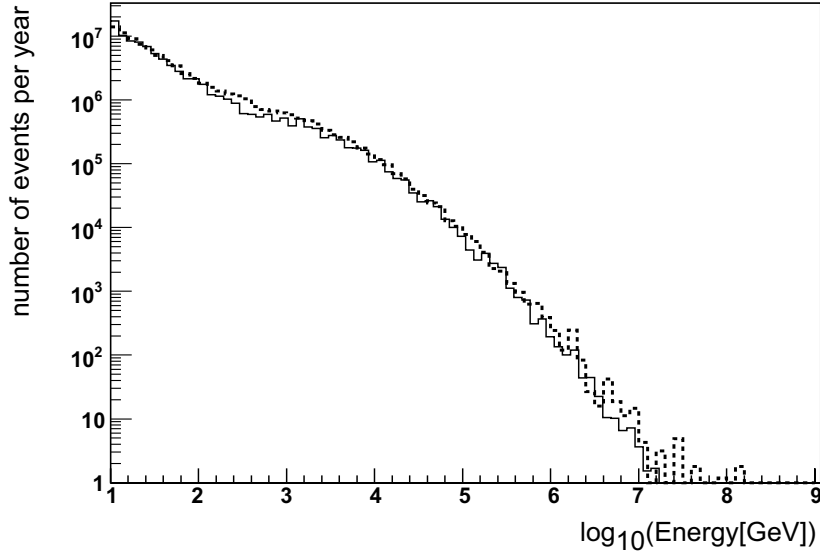


Figure 3.12: Atmospheric muon neutrino rates simulated with GENHEN (dashed) and ANIS (solid like). Only events with a neutrino or secondary muons which could reach the telescope are displayed. The parametrization from Lipari [78] was used.

allows to store events at or inside the Can. For ANIS, the program Atmflux<sup>6</sup> which belongs to the MMC package was used to process the muons produced in neutrino-nuclei interactions.

As can be seen in Figure 3.11, the energy spectra obtained with ANIS and GENHEN are comparable. The remaining differences between the two spectra can possibly be attributed to the use of two different generation algorithms. The low event statistics at energies above  $E > 10^7$  GeV are due to the opacity of the Earth for very high-energy neutrinos (see Introduction). For a study of ultra-high energy (UHE) cosmic neutrinos with ANTARES, one therefore needs to focus on downward-going events. A method to select such events in order to arrive at an estimate of the sensitivity of ANTARES to these rare neutrino events is described in Chapter 5.

In Figure 3.12 the neutrino rates for an atmospheric neutrino flux are compared using either the Barthol model for GENHEN or the Lipari model for ANIS. The rates are comparable. The small differences are most likely due to the slightly different atmospheric flux model and the generation method used. It is concluded that - when suitably tuned - both GENHEN and ANIS can be used to simulate high energy neutrino spectra for ANTARES. However, for ultra-high energy downward-going neutrinos (of  $E_\nu \geq 10^9$  GeV), only ANIS can be used.

<sup>6</sup>Atmflux allows to propagate leptons produced in neutrino-nuclei interactions, from the interaction vertex towards the Can of the telescope and gives an estimate of the energy lost along the path. If a muon reaches the Can or a neutrino interaction occurs inside the Can the energy is positive.

*Neutrino event generators*

## Chapter 4

# Detector simulation and Track reconstruction

*In this chapter a new detector simulation program for neutrino telescopes is presented. The software package, named SIRENE is primarily designed for use with the future cubic kilometer-size detector KM3NeT, but has been applied to ANTARES as the program allows to be easily adapted for other neutrino telescopes. The performance of SIRENE has been compared with that of KM3, another detector simulation package. To validate the quality of the events generated using SIRENE, they have been subjected to two different track reconstruction programs. The results of the comparisons are presented.*



Two different stages of Monte Carlo simulation can be discerned when modelling cosmic-neutrino telescopes: the neutrino event generation and the detector response. Monte Carlo event generators are described in the previous chapter of this thesis. The present chapter focuses on the simulations which model the Cherenkov light created by secondary leptons produced in neutrino interactions, in the instrumented volume of the telescope of interest. It also includes a discussion of the reconstruction algorithms used to extract observables from the simulated events. The design of new neutrino telescopes such as KM3NeT [79] requires the simulation of many different detector geometries and configurations of the photo-sensors in the instrumented volume. However, most programs are not flexible enough to allow different neutrino telescope geometries and only accept neutrino events in a limited energy range. Hence, a fast detector simulation program, capable of modeling the detector response for neutrino events up to the highest energies, and allowing any configuration of the photo-sensors in a neutrino telescope had to be developed. The new detector simulation program

SIRENE does have these features. In the framework of the research project described in this thesis, SIRENE has been integrated in the chain of simulation and reconstruction programs of ANTARES to make it possible to study neutrinos in the ultra high energy range.

A description of the algorithms implemented in SIRENE and the usage of SIRENE to simulate the response of ANTARES are presented in Section 4.1. The tracking method of the secondary particles, essential for neutrino detection and the algorithm used to track the produced Cherenkov photons towards the photomultiplier tubes (PMTs) of the telescope are also discussed. In Section 4.2, the simulation of the signal digitisation and trigger algorithms of ANTARES are presented. A comparison of SIRENE with the existing detector simulation program KM3 is described in Section 4.3. Finally, Section 4.4 focuses on the reconstruction of the energy and track geometry of the muons which caused the hits in the detector.

## **4.1 SIRENE**

The primary objective of SIRENE is to simulate the response to neutrino events of any type of high energy neutrino telescope, considering all scattering processes in the optically transparent medium (water or ice) surrounding the telescope in which Cherenkov radiation occurs. Any type of secondary particle capable of generating detectable Cherenkov photons can be implemented and processed by the detector simulation program.

In the context of this thesis which focuses on the detection of ultra high energy neutrinos, Cherenkov photons from muon neutrino interactions are primarily considered, since the detection probability of such particles is higher than that of the other neutrino flavors due to the longer path length of the produced muons. The tracking of the secondary particles and the evaluation of the Cherenkov photon field they generate for the sea water conditions at the ANTARES site are described in this section. The corresponding software implementation, with the most important C++ classes of the SIRENE libraries and a short summary of their functions are presented in appendix C.

### **4.1.1 Tracking secondary particles**

The various sources of Cherenkov photons generated in muon neutrino interaction, and the passage of the resulting muon through the detector are described in this section, together with their implementation in SIRENE.



## Muons

Input to SIRENE are the starting position, direction, initial energy and time of the muons propagating from the neutrino interaction vertices towards the detector volume. Only particles passing through the Can<sup>1</sup> volume are taken into account. The high energy muons propagate with the speed of light in vacuum  $c$ , since they are relativistic particles produced by very high energy neutrinos. The muon tracks are assumed to be straight lines. The muons suffer stochastic energy losses which produce independent electromagnetic (EM) showers with lower energy. The muon energy loss  $dE_\mu/dx$  is proportional to the muon energy  $E_\mu$ , depositing an energy  $dE_\mu$  in the form of an EM-shower for every distance  $dx$  travelled. The distance  $dx$  is calculated using the mean free path (or interaction length)  $L_\mu$  in the medium the muon traverses. The mean free path depends on the muon interaction processes involved. Bremsstrahlung dominates over the other muon interaction processes at moderate energies ( $E_\mu \geq 1$ ) and contributes about 40% of the total energy loss at ultra high energies (see Chapter 3). According to reference [80], at high energies, the Bremsstrahlung cross section differential in energy is described by

$$\frac{d\sigma}{dk} \approx \frac{1}{n_{at}X_0} \frac{1}{k} \left\{ \frac{4}{3} - \frac{4}{3}y + y^2 \right\} \quad (4.1)$$

with  $n_{at} = N_A \rho / A$  the number of atoms per volume of the medium ( $N_A$  is the Avogadro number,  $\rho$  the density of the medium and  $A$  the mass per mole),  $X_0$  the mean range of muons in the medium,  $k$  the energy of the photons radiated, and  $y = k/E_\mu$  the energy transferred to the photons.

The (truncated) total cross section for emitting photons with a minimum energy<sup>2</sup>  $K_{min}$  is

$$\sigma(E_\mu, k \geq K_{min}) \approx \int_{K_{min}}^{K_{max}} \frac{d\sigma}{dk} dk$$

with  $K_{max} \approx E_\mu$  the maximum energy radiated by the photons.

At high energies ( $E_\mu \gg K_{min}$ ), the total cross section can then be approximated by

$$\sigma(E_\mu) \approx \frac{4}{3} \frac{1}{n_{at}X_0} \ln \left( \frac{E_\mu}{K_{min}} \right). \quad (4.2)$$

A factor 2.5 is used to scale the expression in Equation 4.2 to account for electron-positron pair production (50%) and photo-nuclear interactions (10%) whose contributions are relevant at high energies.

The mean free path of the muon is the inverse of the resulting total cross section. The total number of mean free paths  $n_L$  the muon travels before interacting

---

<sup>1</sup>See Chapter 3.

<sup>2</sup>As can be seen in the next paragraph, this is relevant for the implementation of electromagnetic showers in SIRENE.

is determined in a differential approach to particle transport, which is used in many simulations [53]. First, the quantity  $n_L$  is evaluated,

$$n_L = -\ln \eta$$

with  $\eta$  a random number uniformly distributed in the range (0,1). The corresponding distance is then given by

$$dx = n_L L_\mu$$

with  $L_\mu$  the mean free path of the muon in the medium.

### **Electromagnetic showers**

Muons may give rise to a succession of electromagnetic showers (EM-showers) in the electric field of nuclei on their way through the detector. These EM-showers are composed of charged particles (electrons, positrons and photons). The electrons (and positrons) suffer Bremsstrahlung and generate Cherenkov photons in the sea-water. The photons emitted may, in their turn create an electron-positron pair which may also lead to the emission of Cherenkov photons. This mechanism continues until the energy of the secondary particles falls below the critical energy for which the energy losses via ionisation and the radiative processes become equal (see Chapter 3). The energy at which electrons stop radiating Cherenkov photons has been estimated to be  $E_C = 0.7 \times 10^{-3}$  GeV [81]. At this point, no further EM-showers are produced.

On the length scale of high energy neutrino telescopes, EM-showers can be considered as point-like, i.e. as localised events along the track. Statistical fluctuations between electromagnetic cascades are small if they contain a large number of secondary particles. This is true for showers of energies much higher than their Cherenkov thresholds [82]. As the energy of the EM-showers in SIRENE has a minimum energy of 10 MeV, the EM-showers become independent of the initial muon. For that reason, all EM-showers can be considered identical. In SIRENE, an EM-shower, characterized by its position, direction, energy and time can thus be treated as a source of Cherenkov photons, in the same way as a muon.

The total energy  $E_{rad}$  of the Cherenkov light radiated by the EM-showers can be obtained in the simulation from an exponentiation of the muon energy  $E_\mu$ :

$$E_{rad} = K_{min} \left( \frac{E_\mu}{K_{min}} \right)^\eta$$

with  $\eta$  a random number uniformly distributed between (0,1). The distribution ranges between  $K_{min}$  and  $E_\mu$ , since the muon can transfer substantial amounts, or even almost all of its energy to the particles in the shower. In the code, an EM-shower is created by drawing a random number  $R$  uniformly distributed in the

range (0,1) which needs to fulfill the following requirement

$$R \leq 1 - v + \frac{3}{4}v^2 .$$

This expression is the muon Bremsstrahlung energy loss [53] with  $v = E_{rad}/E_\mu$  the relative energy transfer.

In order to save computing time, a parametrisation is used, replacing the individual particle tracking for the simulation of the EM-shower by results of previous studies on EM-showers parametrisations in ANTARES [83]. The amount of light emitted by the EM-showers and the corresponding angular distribution are smeared using empirical fits to GEANT4<sup>3</sup> detector simulation results.

Since at the energies considered, all EM-showers are identical, only electrons are taken into account for the parametrisation. The total number of Cherenkov photons emitted depends on the energy  $E_{EM0}$  of the initial particle which initiated the EM-shower, in this case the high energy photon from muon Bremsstrahlung. Considering that the energy is equally divided among the electrons (or positrons) and the photons in the shower, the final number of radiating electrons is

$$N_{e^-} = 0.5 \frac{E_{EM0}}{E_C}$$

with  $E_C$  the critical energy for the electron energy loss. This number is then smeared with a Gaussian distribution  $G(N_{e^-})$  to take into account statistical fluctuations in the number of produced electrons. Finally, the number of emitted Cherenkov photons is computed with

$$N_{\gamma EM} = \frac{G(N_{e^-})}{N_{e^-}} \times 6.5 \times 10^4 \times E_{EM0} . \quad (4.3)$$

The value of the constant  $6.5 \times 10^4$  was obtained from empirical fits to GEANT4 simulations. It is the number of photons radiated per centimeter, times the integrated path length of electrons in an EM-shower of 1 GeV.

It is assumed that all the radiated Cherenkov photons are emitted isotropically in azimuth  $\phi$  from the shower axis. The angular distribution of the EM-shower depends on the zenith angle  $\theta$ , according to a parametrisation of the angular distribution in  $\cos \theta$  given by

$$\frac{dN}{d\cos\theta} = 13.7132 \exp \left( -5.2 |\cos\theta - 0.75|^{0.35} \right) . \quad (4.4)$$

The angular distribution is normalised such as to integrate to 1. It is considered to be the same for all particles and shower energies since the amount of electrons, positrons and gamma photons produced in the shower reaches an equilibrium. The form of Expression 4.4, and the values of the constants used result from fits to GEANT4.

---

<sup>3</sup>GEANT4 or GEOMETRY ANd Tracking is a platform to simulate the passage of charged particles through matter [58].

## **Hadronic showers**

Hadronic showers are created in case of a photo-nuclear interaction, i.e. hadrons produced in charged-current inelastic neutrino-nucleus scattering at the neutrino interaction vertex (see Chapter 3). As for electromagnetic showers, hadronic showers can be considered point-like on the large length scale of a neutrino telescope. When an event occurs within the Can of the telescope, the hadronic showers should in principle be simulated, as they may produce charged particles and yield Cherenkov photons [55]. They create a significant number of photons, especially at high energies. However, the high energy neutrino events are likely to be well reconstructed, irrespective of whether the light from the hadronic showers is considered. The contribution of Cherenkov light produced by charged hadronic showers at the neutrino interaction vertex is thus not simulated in SIRENE. Nevertheless, for energies below 100 PeV, the simulation of hadronic showers can be added with the help of the ANTARES GEANT-based Monte Carlo program GEAMU [84], [85]. An interface between SIRENE and this hadronic simulation program is available.

### **4.1.2 Photon field simulation**

All Cherenkov photons are propagated for each individual source towards every optical module of the telescope. The Cherenkov photons produced by a source, which can be either a muon track or a full electromagnetic shower, are tracked using a scattering model of the water at the site of the neutrino telescope. The position, direction, arrival time and wavelength of the photons hitting the optical modules of the telescope are recorded.

## **Medium properties**

The medium in which the photons travel, from their emission point on the muon track to the optical modules (OMs) of the telescope, influences their probability of detection. It is thus necessary to take the main properties of that medium into account when tracking the Cherenkov photons to the detector. The water properties and the scattering model chosen to represent the ANTARES site [86] are implemented in SIRENE. Alternative scattering models representing different medium properties can be added.

**Index of refraction and group velocity** The index of refraction  $n_{medium}$  of a medium is a measure for how much the speed of light is reduced in a transparent medium. It is defined as the ratio of the speed of light in vacuum (reference medium) to the phase velocity  $v_p$  of the photons in the medium of interest

$$n_{medium} = \frac{c}{v_p} .$$

The phase velocity is the rate at which the phase of a light pulse propagates in the transparent medium and depends on the wavelength as

$$v_P = \frac{\lambda}{T} = \frac{w}{k}$$

with  $\lambda$  the wavelength,  $T$  the period,  $w$  the angular frequency and  $k$  the wavenumber of the photons in the medium. As a result, a dispersion of the light inside the medium is induced.

An empirical equation for the index of refraction of sea water, based on a parameter fit by Quan and Fry [87], corrected for the pressure at the ANTARES site was determined as a function of the wavelength  $\lambda$  of the photons [55], [86]. As can be seen in Figure 4.1, the model describes well the refractive index of the sea water at the ANTARES site, for the range of wavelengths of interest ( $300 \text{ nm} \leq \lambda \leq 600 \text{ nm}$ ). The empirical equation is given by

$$n(\lambda) = 1.3201 + 336. \times 10^{-5} + \frac{16.256}{\lambda} - \frac{4382}{\lambda^2} + \frac{1.1455 \times 10^6}{\lambda^3} . \quad (4.5)$$

In SIRENE, the photons are assumed to propagate in the transparent medium around the telescope with the group velocity  $v_g^{medium}$  which is defined as

$$v_g^{medium}(\lambda) = \frac{c}{n_g^{medium}}$$

with  $c$  the speed of light in vacuum and  $n_g^{medium}$  the effective refractive index group velocity in the medium or group index of refraction, which is defined below<sup>4</sup>. The group velocity is the speed with which the variations in the shape of the photon waves amplitude (i.e. is the modulation or envelope of the waves) propagate through a transparent medium. It can be written as

$$v_g^{medium} = \frac{dw}{dk}$$

with  $w$  the angular frequency and  $k$  the wave number of the light waves. Since  $w$  and  $k$  depend on the refractive index  $n_{medium}$  of the medium and the wavelength  $\lambda$  of the photons, such that

$$w = \frac{ck}{n_{medium}}$$

and

$$k = \frac{2\pi}{\lambda} .$$

---

<sup>4</sup>The index of refraction was used in earlier detector simulations, but it was found to introduce a non-negligible error, considering the high resolution of neutrino telescopes such as ANTARES [88], [55].

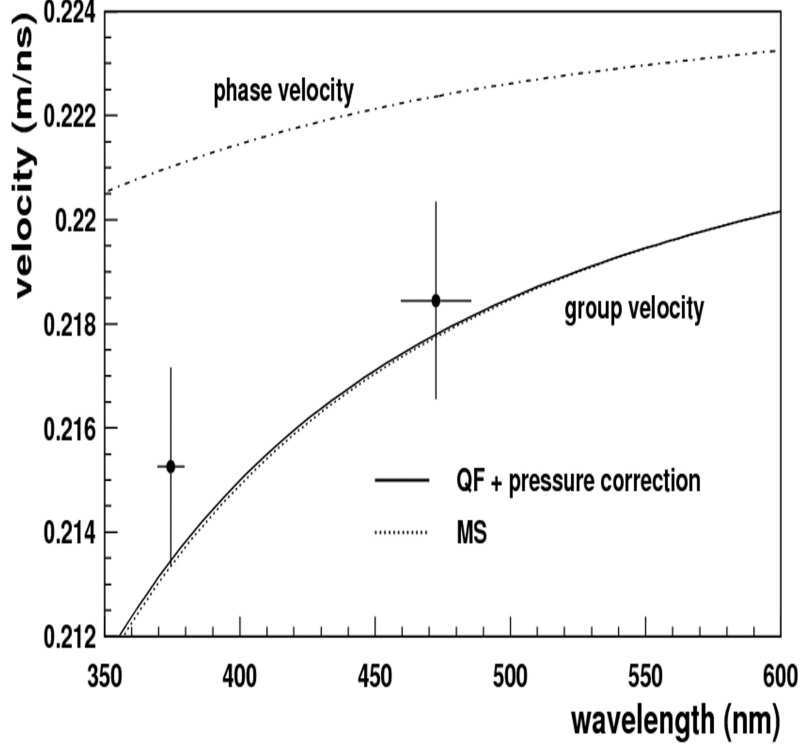


Figure 4.1: Comparison of measurements of the group velocity of light in sea water at the ANTARES site and model prediction. The phase velocity is also shown [86].

The group velocity of the photons in the medium and the index of refraction  $n_{medium}$  are related by

$$v_g^{medium} = \frac{c}{n_{medium}} \left( 1 + \frac{\lambda}{n_{medium}} \frac{dn_{medium}}{d\lambda} \right).$$

This equation is used to define the group index of refraction

$$n_g^{medium}(\lambda) = \frac{n}{1 + \frac{\lambda}{n} \frac{dn}{d\lambda}}$$

which will be used together with the parametrisation given by Equation 4.5 to determine the path length and the arrival time of the photons at the OMs. The wavelength dependence of the group velocity (and consequently the index of refraction group of light) induces a spread in the arrival times of the Cherenkov photons at the OMs.

**Light absorption** The absorption length  $L_{medium}$  of the transparent medium surrounding the telescope is the mean free path of a photon, before undergoing a

non-elastic interaction in the medium. It is wavelength dependent. For sea water at the ANTARES site, the absorption length is parametrised by the model described in [89], rescaled to coincide with the maximum absorption length which was measured in situ at the reference wavelength <sup>5</sup> of 460 nm [86]. A flux of photons travelling a distance  $l$  through a transparent medium will then be attenuated by the absorption factor  $A(\lambda)$ , depending on  $L_{medium}$  with

$$A(\lambda) = \exp\left(\frac{-l}{L_{medium}(\lambda)}\right)$$

where  $\lambda$  is the wavelength of a photon.

### Tracking algorithm

Since the number of events to be processed by the detector simulation is large, the number of secondary particles produced is also large. As the distances traversed by the muons are also large, propagation of the total number of emitted photons is not feasible. In SIRENE, an alternative method has been implemented.

For each source, Cherenkov photons are generated, with a wavelength distribution between 300 nm and 600 nm. The corresponding arrival times on every optical module (OM) in the telescope are calculated, using the medium properties described above. Direct and scattered photons from muons, and direct photons from electromagnetic (EM) showers are recorded. As a first approximation, the wavelength and time distributions of the generated photons are taken to be independent. Both wavelength and time distributions are normalised to the total number of generated photons.

In SIRENE, photons are propagated to a so-called “virtual module”, defined as a sphere encompassing one or more OMs of the telescope. The concept of a virtual module allows efficient comparison between different configurations of optical modules (OMs). It reduces the total CPU time when comparing different OM-configurations inside the virtual module, as only the propagation of the photons inside the virtual module has to be repeated.

The emitted Cherenkov light is propagated towards a plane intersection of the virtual sphere. The orientation of the disk defined by the intersection is perpendicular to the direction of the photon (of 460 nm). In the case of the ANTARES telescope, the virtual sphere was chosen to enclose a single OM <sup>6</sup> and the disk passes through the center of it (see Figure 4.2). The radius of the virtual sphere

---

<sup>5</sup>The wavelength taken as a reference is 460 nm. This corresponds to the maximum sensitivity of the optical modules (OMs) of the ANTARES telescope.

<sup>6</sup>To gain running time, a virtual sphere could also envelop an entire storey (see Chapter 1) which is the basic component of the ANTARES telescope, consisting of three optical modules (OMs). SIRENE has also been tested with this configuration. To ease the implementation of the existing software generating the effect of the front-end electronics, it was decided to define for ANTARES the virtual module to be the optical module (see Section 4.2).

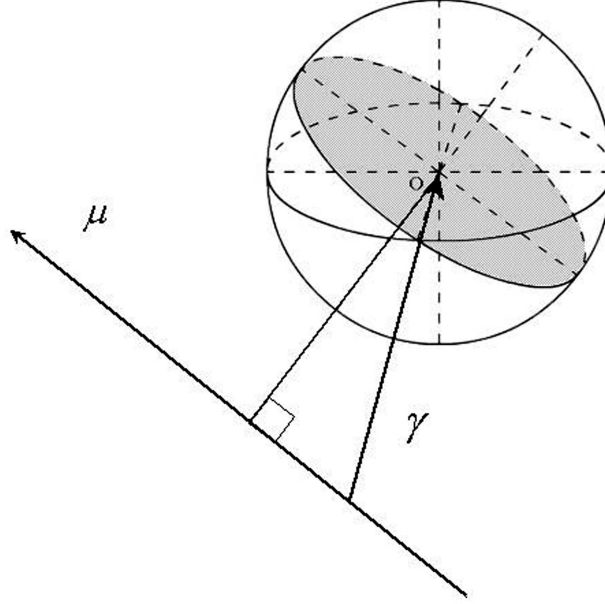


Figure 4.2: Tracking of a photon  $\gamma$  from the muon track  $\mu$  towards the module centered at  $O$ . The virtual sphere which is used in the simulation is shown, together with the optimally oriented virtual module, which is the (grey) plane perpendicular to the photon direction. In this example, the virtual sphere was chosen to encompass one single optical module (OM). The sphere and the module have the same radius.

is identical to that of the OM, so the OM and the abstract module have the same geometric characteristics and the number of detected photons is closest to reality. The tracking of the photons to the optical modules is illustrated in Figure 4.3.

The quantities relevant [68] to determine the amount of light reaching the OM are:

- the expected photon field path length,
- The predicted angle of incidence of the photons on the OM, i.e. the angle between the direction of the photon field and the pointing direction of the OM,
- the predicted arrival time  $t_{hit}^{th}$  of the photons on the OM.

These three properties characterize the position and the orientation of a given OM relative to the muon track. To determine the path length of the emitted photons, the angle of incidence and the true arrival time at the OM, the location of the OM,  $\vec{r}_{OM}$  is required, as well as the start and end-position of the muon track,  $\vec{r}_{start}$  and



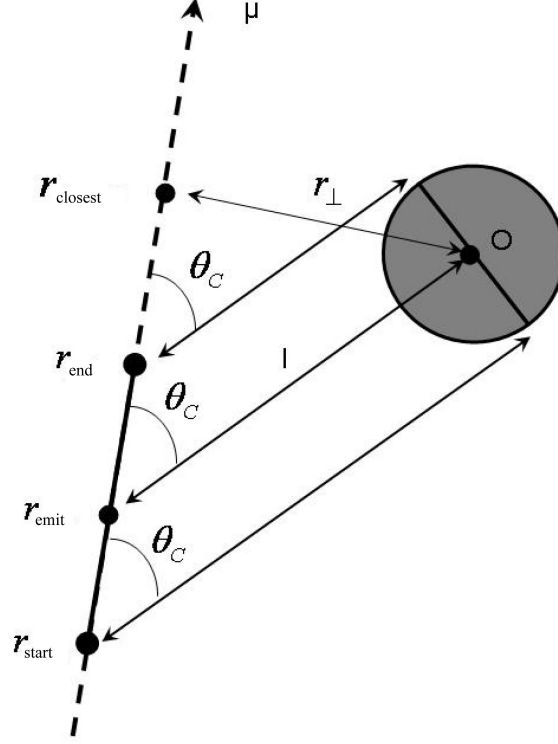


Figure 4.3: Coordinates used to describe the detection of Cherenkov light. The muon track  $\mu$  is characterized by its start-position  $\vec{r}_{start}$  at time  $t_{start}$  and end-position  $\vec{r}_{end}$  at time  $t_{end}$ . Cherenkov photons are emitted in  $\vec{r}_{emit}$  at time  $t_{emit}$ , under the angle  $\theta_C$ . The shockfront of the generated photon field hits the optical module (OM) located in  $\vec{r}_{OM}$  at time  $t_{hit}$ . The distance the photons travelled to reach the OM is  $l$ . The distance of closest approach between the muon track and the center of the OM is  $r_{\perp}$ .

$\vec{r}_{end}$  and the time  $t_{start}$  at  $\vec{r}_{start}$ . In the following paragraphs, it is explained how these quantities are calculated.

**Photon path length** The path length  $l$  of the photon field is the distance between the OM and the position  $\vec{r}_{emit}$  on the track emitting the light. According to Figure 4.3, it can simply be calculated as

$$l = |\vec{r}_{OM} - \vec{r}_{emit}| = \frac{r_{\perp}}{\sin \theta_C}$$

where  $r_{\perp}$  is the distance of closest approach between the track and the center of the OM, which is the distance perpendicular to the muon direction. For Cherenkov

radiation (see Chapter 1), the sinus of the emission angle can be expressed as

$$\sin \theta_C = \sqrt{(1 - \cos^2 \theta_C)} = \sqrt{1 - \frac{1}{\beta^2 n_g^2}}$$

with  $\beta = v/c$  the velocity of the particle  $v$  expressed as a fraction of the speed of light in vacuum  $c$ . Since the muons are relativistic particles,  $\beta = 1$ , the path length of the photons in sea water can thus be calculated as

$$l = \frac{r_{\perp}}{\sqrt{1 - \frac{1}{n_g^2}}}$$

**Incident photon angle** The cosine of the angle of incidence of the photon field on the OM can be approximated by the dot product between the direction of the emitted photons and the direction of the OM axis. The maximum efficiency of the OM is obtained when the photon field is parallel to the front of the OM, which correspond to  $\cos \theta = 1$ . In contrast,  $\cos \theta = -1$  corresponds to the minimum efficiency of the OM, i.e. when a photon flux hits the back of the OM which is painted black.

**Arrival time of the photons** The arrival time of the photons on the OMs is calculated from the muon track parameters as

$$t_{hit}^{th} = t_{start} + \frac{|\vec{r}_{emit} - \vec{r}_{start}|}{c} + \frac{|\vec{r}_{OM} - \vec{r}_{emit}|}{v_g^{water}} \quad (4.6)$$

which is the sum of the initial time of the muon track, the time the muon travelled before reaching  $\vec{r}_{emit}$  and emitted light, and the time it takes for the produced photons to reach the OM. For ease of writing, Equation 4.6 will be written in the following as

$$t_{hit}^{th} = t_{start} + t_{emit} + t_{travel}.$$

In SIRENE, this expression is implemented as follows. The time of emission of the photons on the muon track can be calculated as

$$t_{emit} = \frac{|(\vec{r}_{closest} - \vec{r}_{start}) - (\vec{r}_{closest} - \vec{r}_{emit})|}{c}$$

where  $\vec{r}_{closest}$  is defined in Figure 4.3. This expression can also be written as

$$t_{emit} = \frac{|\vec{r}_{closest} - \vec{r}_{start}|}{c} + \frac{l \cos \theta_C}{c}.$$

The time the light travels in water is expressed as the ratio of the path length  $l$  and the group velocity  $v_g^{water}$  of the photons in sea water

$$t_{travel} = \frac{l}{v_g^{water}} = \frac{1}{v_g^{water}} \left( \frac{r_{\perp}}{\sin \theta_C} \right).$$

The time of arrival of the photons on the OM is thus calculated by

$$t_{hit}^{th} = t_{start} + \frac{1}{c} \left( |\vec{r}_{closest} - \vec{r}_{start}| - \frac{r_{\perp}}{\tan \theta_C} \right) + \frac{1}{v_g^{water}} \left( \frac{r_{\perp}}{\sin \theta_C} \right). \quad (4.7)$$

If muons are relativistic particles, and considering the Cherenkov approximation, the hit time can be modelled by

$$t_{hit}^{th} = t_{start} + \frac{|\vec{r}_{closest} - \vec{r}_{start}|}{c} + \frac{1}{c} \left( \frac{r_{\perp}}{\sqrt{1 - n_g^2}} \right) (1 - n_g^2). \quad (4.8)$$

The model is similar to the one used in the detector simulation programs KM3 [90] and GEASIM [84].

The hit time and wavelength of the Cherenkov photons which can reach the optical module (OM) are then randomly sampled from the generated distributions so that each event is unique.

Both the direct and scattered photons from muons are sampled from the same distributions. The arrival times for the scattered photons are smeared using a truncated normal distribution. This truncated distribution is the probability distribution of the normally distributed hit time whose values are bound by the standard deviation

$$\sigma = 2.5 \sqrt{0.0005 + t_{travel}^{460}}.$$

The variable  $t_{travel}^{460}$  is the amount of time a reference photon with a wavelength of 460 nm needs to travel from the muon track to the OM. Only the photons which scatter with relatively small angles are taken into account in this parametrisation. They are more likely to be observed with a time delay of less than typically 10 ns with respect to direct photons. Photons which scatter with relatively wide angles and are delayed more have been neglected. The high energy neutrino events are likely to be well reconstructed, irrespective of whether these photons are considered.

In Figure 4.4, the simulated time residuals  $r = t_{hit} - t_{hit}^{th}$  are shown between the hit time  $t_{hit}$  obtained from the PMTs and the predicted arrival time  $t_{hit}^{th}$  of the photons on the OM. The contribution from the muons and the EM-showers are shown separately. The broad tails at large positive values of  $r$  are due to light scattering. All distributions are peaked around  $r = 0$  ns. Direct photons from muons carry the most precise timing information, while scattered photons from muons are delayed with respect to this reference time. The distribution of the arrival time for (direct) photons from EM-showers occurs in a broader time range. This is due to the fact that the photons are not emitted at a fixed angle  $\theta_C$  but according to an angular distribution (see Section 4.1.1).

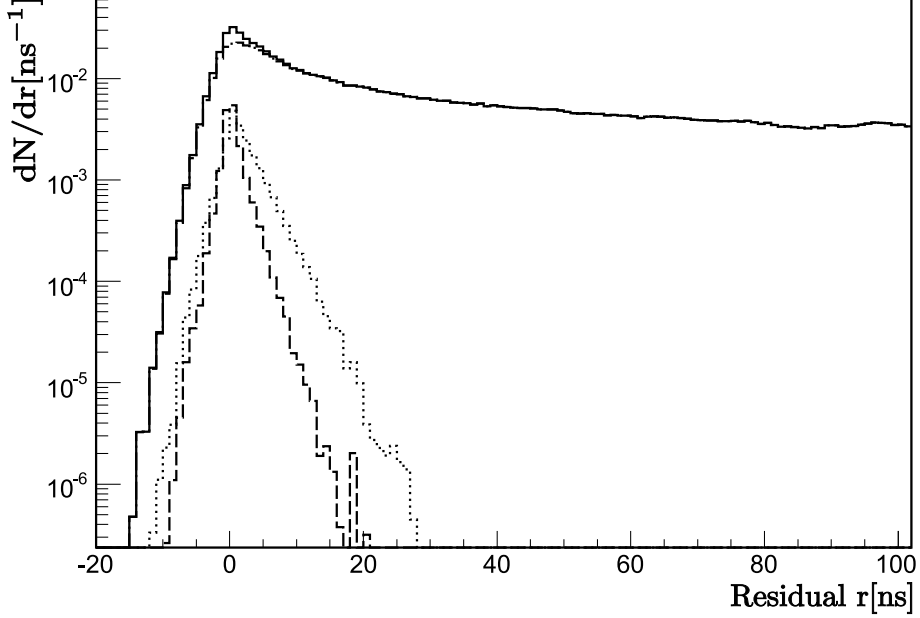


Figure 4.4: Simulated distributions of the time residuals  $r$  (in ns) between the hit time obtained from the PMTs and the predicted arrival time of the photons on the OMs. The contribution from direct photons emitted by muons is shown by the dashed line. The contribution from all muons is represented with a dotted line. The time residual for photons from electromagnetic showers is displayed by the dotted-dashed line. The contribution for all photons is shown by the solid line.

**Effective photon flux detected** The photons inside the optical module (OM) need to be tracked towards the photomultiplier tube (PMT) to determine the average number of photo-electrons which are produced. The effective photon field strength is computed taking into account the reduction of the light flux due to absorption by the OM glass and optical gel, as well as the quantum efficiency of the PMT, and the angle of incidence  $\theta_{inc}$  of the photons. This is calculated for each OM in the telescope, by weighting the photon flux arriving on the glass sphere by the effective area  $A_{eff}$  of the OM, which depends on the wavelength of the Cherenkov photon and the OM orientation. The quantity  $A_{eff}$  is the product of the OM angular acceptance  $A_g(\theta_{inc})$ , the light transmission through the OM glass  $P_{transmission}^{glass}(\lambda)$  and the optical gel  $P_{transmission}^{gel}(\lambda)$ , as well as the quantum efficiency  $QE(\lambda)$  of the PMTs

$$A_{eff}(\theta_{inc}, \lambda) = A_g(\theta_{inc}) \times P_{transmission}^{glass}(\lambda) \times P_{transmission}^{gel}(\lambda) \times QE(\lambda)$$

with  $\theta_{inc}$  the incident angle with respect to the OM orientation axis.

The angular acceptance  $A_g(\theta_{inc})$  of the OMs accounts for the differences in detection probability of photons that arrive with different angles with respect to the photo-cathode. The OM of the ANTARES telescope has been described in Chapter 1. The angular acceptance function  $A_g(\theta_{inc})$  has been determined by the Gamelle measurements [91]. It is described by a fit to these results [92], which is normalised such that the angular acceptance  $A_g$  gives the maximum OM efficiency for  $\cos(\theta_{inc}) = 1$

$$A_g(\cos\theta_{inc}) = 0.26 + 0.67\cos\theta_{inc} + 0.31\cos^2\theta_{inc} - 0.23\cos^3\theta_{inc} .$$

The transmission of the photons through the glass of the OM  $P_{transmission}^{glass}(\lambda)$  and through the optical gel  $P_{transmission}^{gel}(\lambda)$ , as well as the quantum efficiency (QE( $\lambda$ )) of the PMTs are wavelength dependent. Their parametrisations as a function of the wavelength are needed to estimate the amount of light which can reach the PMT before digitisation of the signal (see Section 4.2). Measurements of these wavelength dependences by Hamamatsu for the PMT and laboratory measurements for the OM main characteristics [93], [91] are used in SIRENE.

**Computation** The Cherenkov wavelength range is divided into bins of width  $d\lambda = \lambda_{i+1} - \lambda_i = 10$  nm from 300 nm to 610 nm. According to Equation 1 in Chapter 1, the amount of Cherenkov light produced by a muon, per unit of track length  $r$ , in the wavelength domain  $[\lambda_i, \lambda_{i+1}]$  is given by

$$\frac{dN_\gamma}{dr} = \frac{2\pi\alpha}{\lambda^2} \left(1 - \frac{1}{\beta^2 n^2}\right) \frac{\lambda_{i+1} - \lambda_i}{\lambda_{i+1} \lambda_i} .$$

The average number of photons emitted by the muon track for a given wavelength bin  $[\lambda_i, \lambda_{i+1}]$  is then calculated by

$$N_\gamma(\lambda) = |\vec{r}_{end} - \vec{r}_{start}| \frac{dN_\gamma}{dr} .$$

The average number of photons detected by the OM in each wavelength domain can then be computed as the number of photons emitted by the muon track in this wavelength bin, multiplied by the OM effective area,

$$N_{detected}(\lambda) = N_\gamma(\lambda) A_{eff}(\theta_{inc}, \lambda) . \quad (4.9)$$

The total number of photo-electrons (npe) detected by the OM can then be computed by taking the integral of equation 4.9 over the full Cherenkov wavelength range

$$N_{npe} = \int_{\lambda=300\text{nm}}^{\lambda=610\text{nm}} N_\gamma(\lambda) A_{eff}(\theta_{inc}, \lambda) d\lambda .$$

The total number of photo-electrons is smeared with a Poisson/Gaussian (the Poisson distribution becomes normal for large npe) distribution to take into account the statistical fluctuations between the different wavelength domains. The Gaussian is used when the total number of npe is larger than the saturation level of the ARS of the photo-multiplier tube (PMT) inside the OM <sup>7</sup>. The result represents the total number of photo-electrons that actually need to be generated by the simulation.

Wavelengths and arrival times of each photon are pulled randomly from the generated wavelength and arrival time distributions of the emitted Cherenkov photons. The positions and directions of the photons on the virtual module are also randomly sampled. The output of the program is a set of photo-electrons with their position, direction, energy and arrival time at the different OMs in the telescope.

**Results** The simulated number of detected Cherenkov photons per OM is shown in Figure 4.5 as a function of the distance of closest approach of the muon track to the hit OM. As can be seen from the figure, at low energies ( $E \leq 1$  TeV) the contribution from muons is still relatively important as compared to that of the EM-showers. Above this energy, the number of photons from showers starts to dominate. This is in agreement with the muon energy loss behaviour (see Chapter 3). Roughly 90% of the hits originate from within 300 m of the track, which is inside the limits of the default Can volume of ANTARES (see Chapter 3). This validates the choice of the Can parameters.

In Figure 4.6, the number of detected photons from EM-showers is displayed as a function of energy. The number increases roughly exponentially with the muon energy, while the contribution from muons alone is constant. This is in agreement with our expectations based on the known equation of the muon energy loss (see Chapter 3).

The amount of Cherenkov light detected becomes considerable for the highest energy events. Unfortunately, the corresponding simulation becomes CPU-intensive and yields output files of a very large size. To avoid this problem when simulating high energy events, and in order to make the simulation CPU-effective, SIRENE generates a maximum number of photons on the telescope's OMs and associates a weight to each of them. The photon weight is equal to 1 if the number of photons reaching an OM is smaller than the maximum of photons allowed for the simulation. If the number of photo-electrons detected by an OM is larger than the maximum number of photo-electrons allowed, the weight is set equal to the ratio of the number of photons that should have been generated to the maximum number of photons allowed. The maximum amount of Cherenkov photons allowed to be generated on each OM can be set manually at the start of

---

<sup>7</sup>The saturation level of the ARS of the ANTARES telescope is 8 photo-electrons in the so-called single photo-electron (SPE) detection mode [94].

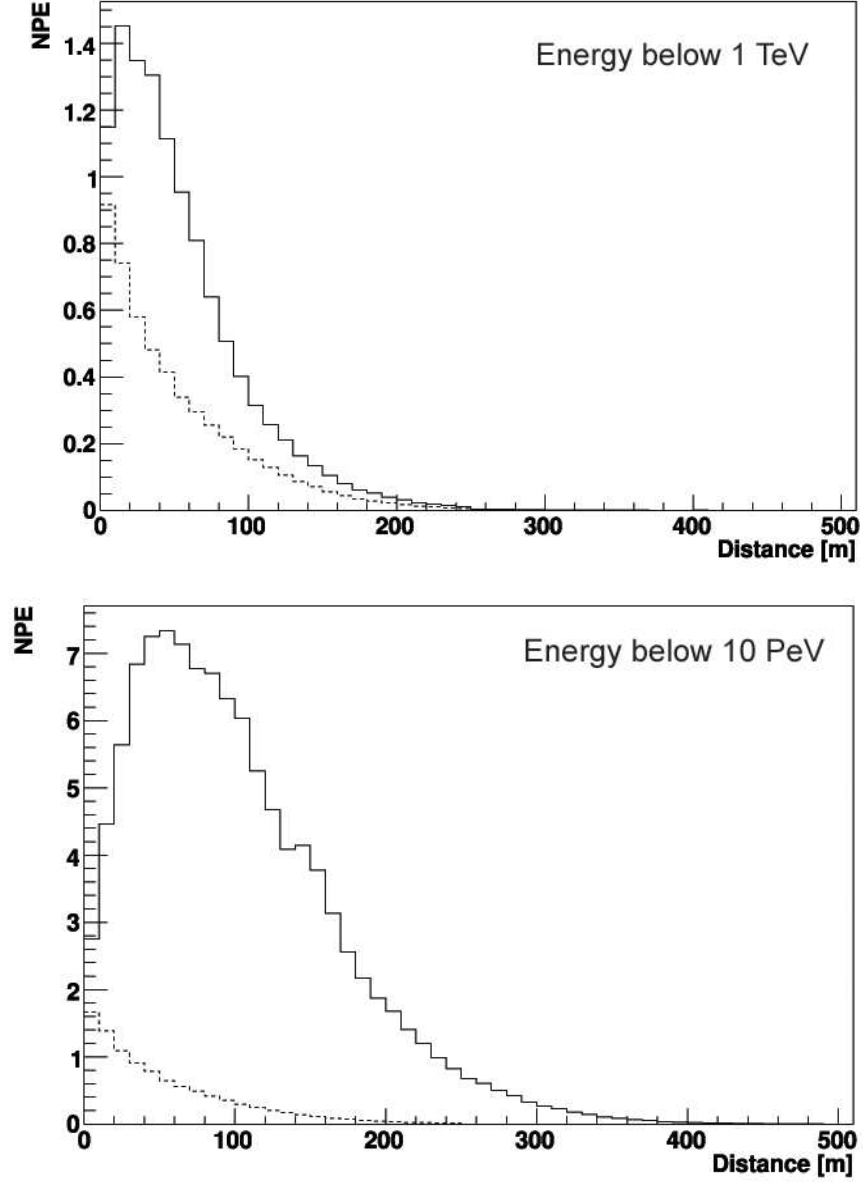


Figure 4.5: Simulated number of detected Cherenkov photons (NPE) per OM as a function of the distance of closest approach of the muon track to the hit OM. The total number of detected photons, i.e. from muons and EM-showers is shown as a solid line. The contribution from muons only is shown by a dashed line. In the top plot the number of photons for muons with an energy  $E_\mu \leq 1$  TeV is shown. In the bottom plot, the number of photons for muons with an energy  $E_\mu \leq 10$  PeV is shown.

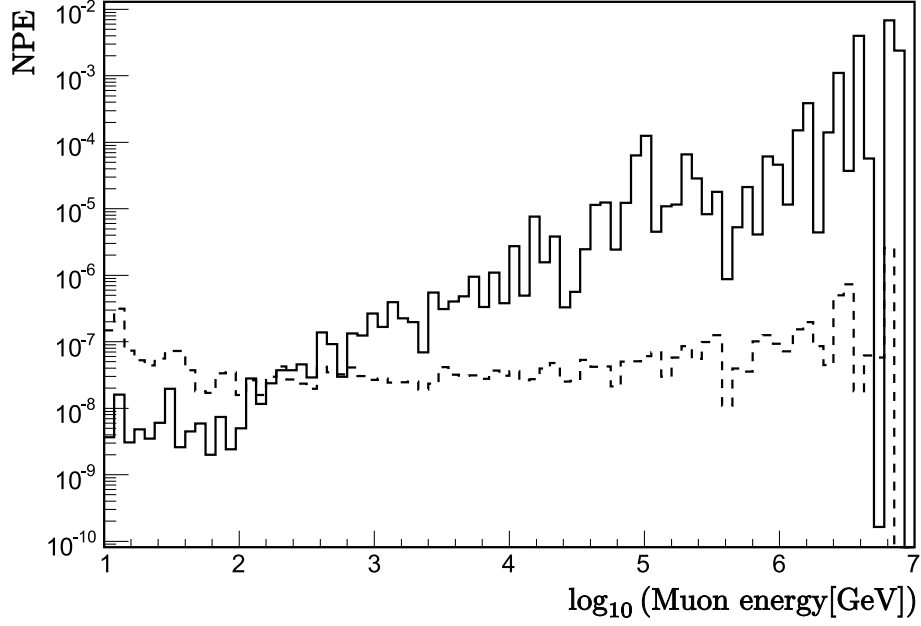


Figure 4.6: *Distribution of the number of detected Cherenkov photons (NPE) from electromagnetic showers (solid) and muons (dashed) as a function of the muon energy.*

the simulation. The default value is 80 photons, which is far beyond the saturation level of the PMT cathode at 8 npe. Thereafter the hits need to be processed by a simulation of the detector electronics to be able to study the performance of the trigger and the reconstruction software. This final step is presented in the next section.

## 4.2 Signal digitisation and triggering

As seen in Chapter 2, the front-end ARS chip integrates the analogue signal of the PMT by summing the total number of detected photons over a typical time window (25 ns). This is simulated by the trigger software (see Chapter 2) which translates the amplitude and time information of each hit into AVC, timestamp and TVC values, respectively. A so-called L0 trigger occurs when the PMT signal exceeds a certain threshold. In SIRENE, hits with an amplitude larger than 0.3 of a single photo-electron amplitude are selected. Since consecutive photons arriving on a PMT within less than 25 ns cannot be observed separately due to the ARS integration, they are combined into one single signal. The trigger adds the amplitudes of the photons and the hit time is considered to be the time of the earliest photon. This is illustrated in Figure 4.7, where the time residuals  $r = t_{hit} - t_{hit}^{th}$  between the hit time  $t_{hit}$  obtained from the digitized PMT signal and the predicted arrival time  $t_{hit}^{th}$  of the photons on the OMs are shown. The tail of the peak at  $r = 0$



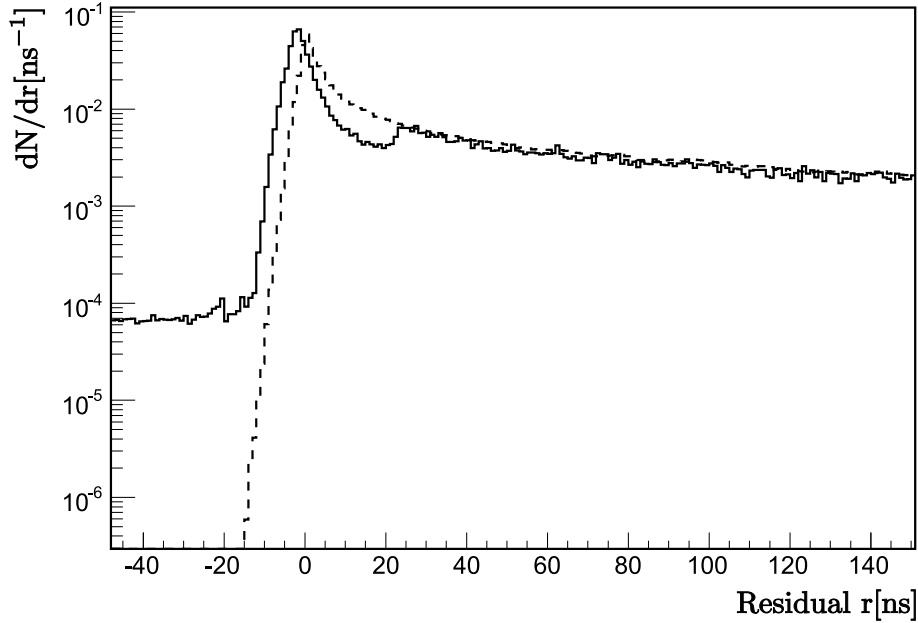


Figure 4.7: Time residuals  $r = t_{hit} - t_{hit}^{th}$  between the hit time  $t_{hit}$  obtained from the digitized PMT signal and the predicted arrival time  $t_{hit}^{th}$  of the photons on the OMs (solid). The distribution without simulation of the electronics is shown (dashed) for comparison.

is depleted compared to the distribution before digitisation (see Figure 4.4) and a smaller second peak can be seen above 25 ns. The additional peak corresponds to the integration of the signal by the second ARS of the PMT while the first chip is inactive. As can be seen in the figure, the peak at  $r = 0$  is shifted to the left compared to the distribution without the simulation of the electronics. This is due to the combination of the hits which are separated by less than 25 ns, especially if the number of photons that was merged is large. The trigger can also add a constant rate of uncorrelated background to the hits from  $\beta$ -decay of  $^{40}\text{K}$  in salty sea water and bioluminescence (see Chapter 1). In Figure 4.7 a rate of 70 kHz per PMT, which is the uncorrelated background usually observed in situ was added. This is reflected in the plateau at negative time residuals in Figure 4.7.

L1 triggered hits are built from two or more L0 hits at the same storey over a small time window of typically 20 ns. Any of the available trigger algorithms can be applied to the digitized SIRENE data. In this work, the standard three-dimensional trigger or 3D-trigger (see Chapter 2) was used to select the hits with minimum five local coincidences (5L1 hits). The detector geometry, as well as the AVC, the TVC, and the overall time calibrations are used by the trigger algorithm to convert the raw data into calibrated data for further processing by the reconstruction and analysis programs. The decoding is done by retrieving information from files obtained with the calibration methods described in Chapter 2.

In order to validate the performance of the new detector software, SIRENE

has been compared with KM3 and GEASIM, using the ANTARES geometry. The results of this comparison are presented in the next section.

## **4.3 Comparison with the ANTARES detector simulations**

### **4.3.1 KM3 and GEASIM**

The ANTARES collaboration has developed two Monte Carlo programs for the simulation of the response of the detector to passing muons, each simulating different aspects of the events. The package KM3 simulates the detector response to the Cherenkov light produced by muons and secondary electromagnetic particles from neutrino interactions in the media surrounding the telescope, including scattering in sea water. Pre-calculated data tables generated with a full GEANT simulation [58] are used to parametrise the amount of Cherenkov light reaching the optical modules (OMs) of the detector. The use of these “photon-tables” makes the simulation faster.

The second simulation program is GEASIM which accounts for hadronic effects not included in KM3. GEASIM performs the tracking of all particles, except for the Cherenkov photons, through the entire telescope volume. It uses an analytical function to estimate the number of photons detected, assuming there is no light scattering in the sea water.

Both KM3 and GEASIM are written in the FORTRAN language and are running under UNIX. A detailed description of the programs and the methods chosen for tracking the particles of interest can be found in several ANTARES internal notes [90], [84] and PhD theses [55], [68].

For a realistic simulation of the angular resolution of the telescope, light scattering cannot be neglected. This is included in both SIRENE and KM3. The latter program uses the package *MUSIC* (see Chapter 3) to propagate the muons in straight lines, through the telescope. Electromagnetic showers (EM-showers) are randomly generated along the path when the muon energy loss exceeds the Cherenkov threshold (0.3 GeV). Since the contribution of the Cherenkov photons from charged hadrons can be substantial in the low part of the energy range covered by ANTARES, GEASIM is used in combination with KM3 to add the light emitted from hadronic showers. As in SIRENE, light scattering in sea-water is neglected for EM-showers and hadronic showers. The models implemented in GEASIM for light scattering and the wavelength dependence of the refractive index are the same as the ones in SIRENE.

While SIRENE is designed to process neutrino events of the highest energies ( $E_\nu \leq 10^{12}$  GeV), the existing ANTARES detector simulation programs cannot be used above  $10^7$  GeV. For the study of the ultra high energy cosmic neutrinos, it is thus necessary to use SIRENE. However, in order to validate the new detector

### 4.3 Comparison with the ANTARES detector simulations

simulation program, SIRENE has been compared to KM3 with GEASIM at lower neutrino energies.

#### 4.3.2 Simulation results

##### Event rates

To compare the output of SIRENE with that of KM3/GEASIM,  $N_{gen} = 10^9$  upward-going muon neutrinos were generated with GENHEN, assuming an AGN-like  $E^2\Phi = 10^{-6} \text{ GeV m}^{-2} \text{ sr}^{-1} \text{ s}^{-1}$  power law spectrum at the surface of the Earth, in the energy range  $10 - 10^7 \text{ GeV}$ . The produced muon secondaries were propagated towards the default Can of ANTARES using the lepton propagator MUM. Both SIRENE and KM3/GEASIM were used to process the output file of GENHEN. On output only those events were selected, which produce detectable light. In Figure 4.8, an example of the corresponding energy spectra of the simulated neutrino events which could be detected is drawn. Only charged-current (CC) neutrino interaction events are shown.

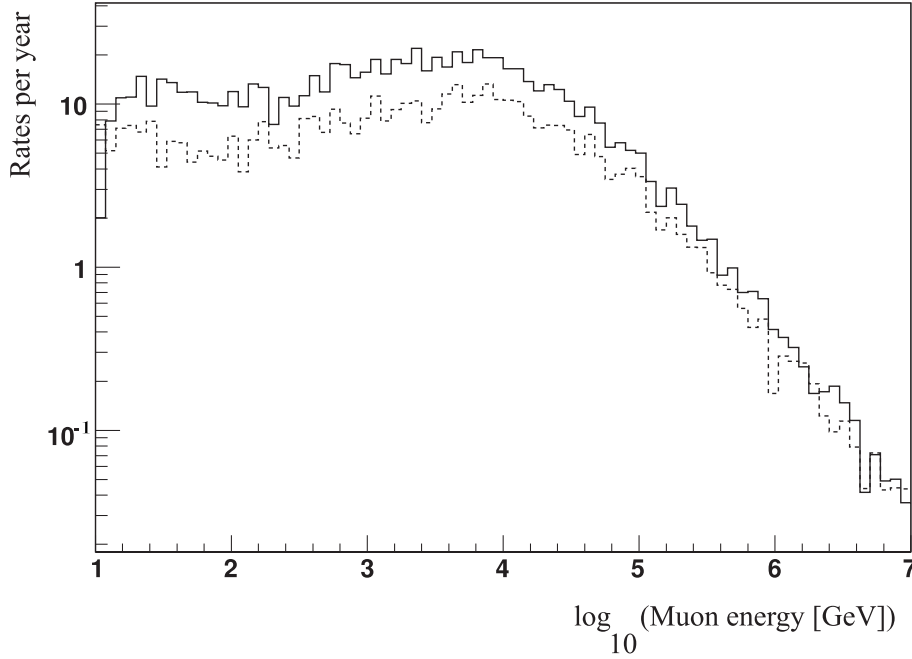


Figure 4.8: *Simulated energy spectra of events producing detectable secondaries in ANTARES. SIRENE (solid) and KM3 (dashed) were used with the same input file containing muon tracks, generated by GENHEN. The Cherenkov photons were simulated within the default Can of ANTARES.*

As can be seen in Figure 4.8, the two distributions are similar in size and shape, in particular for energies above  $10^4 \text{ GeV}$ . As SIRENE has been designed

for processing events of the highest energies, the discrepancies at lower energies can be attributed to the parametrisation of the muon total cross section which neglects low energy effects (see Section 4.1). The remaining differences between the spectra are assumed to be caused by the use of two different photon tracking algorithms.

### Hit time residuals

In Figure 4.9, the time residuals  $r = t_{hit} - t_{hit}^{th}$  between the hit time  $t_{hit}$  obtained from the PMTs and the predicted arrival time  $t_{hit}^{th}$  of the photons on the OM is shown. Both distributions are peaked at  $r = 0$ . The distribution produced using SIRENE is broader compared to the one computed with KM3. This is due to the fact that SIRENE takes the dimensions of the OM sphere into account, while KM3 does not. The photons may hit the OM earlier or later than they would have arrived at its center.

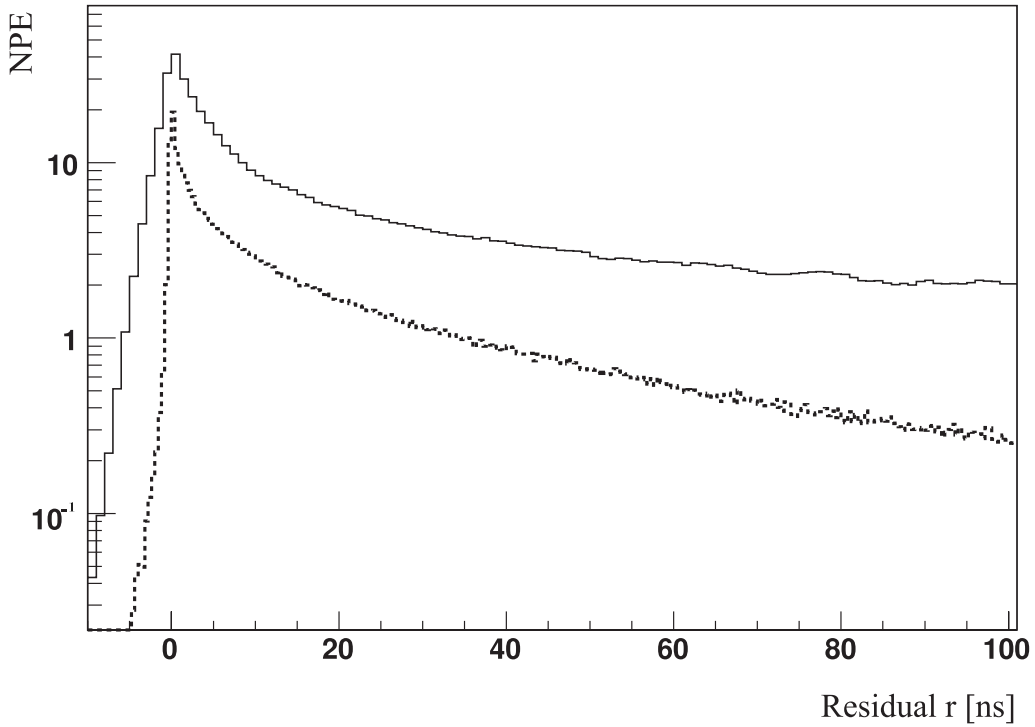


Figure 4.9: Distribution of the time residuals between the hit time obtained from the PMTs and the theoretical arrival time of the emitted Cherenkov photons on the OMs. Photons from muons and electromagnetic showers are taken into account. The time residuals calculated with SIRENE are shown by a solid line, while the time residuals given by KM3 are represented by a dashed line.

It can be concluded that KM3 and SIRENE give similar results, although dif-

ferences remain that can be attributed to different methods and amount of detail employed by the two programs. In contrast to KM3, SIRENE is suited for neutrino simulations at ultra high energy, that is above  $10^7$  GeV.

The methods used to reconstruct the SIRENE data, after their digitisation and processing through the trigger software are described in Section 4.4. Possible extensions of the program are presented in the last section of this chapter.

## 4.4 Reconstruction

Several dedicated programs are available within the ANTARES collaboration to reconstruct the muon position, direction and energy, considering the time and amplitude of the physics events recorded by the trigger software. The task of the reconstruction routine is to estimate track parameters<sup>8</sup> that are compatible with the observed hits. The relation between the position and orientation of the muons with the arrival time of the emitted photons is described by the model prediction given by Equation 4.7. Hence, the track reconstruction is non linear. Therefore, approaches such as maximum likelihood, minimum chi-square or other least square methods [95] are usually applied in an iterative process. The procedures can be used in a linearised form by keeping one of the parameters constant. For instance, it has been demonstrated [96] that the hit time is a linear function of the muon position, once the track direction is fixed. The iterative process allows then to find a unique solution for the muon position and time for each direction, in each step. This concept was exploited by the reconstruction algorithms that are used below.

The events produced by SIRENE were reconstructed with an algorithm, known as AartStrategy [68] and a more recent algorithm called ScanFit [21]. The algorithms are based on different approaches to overcome the non linearity of the problem mentioned above. The reconstruction routines also provide information on the precision and quality of the proposed fits and the associated uncertainties of the results. For the energy reconstruction, an independent program [97] is used.

The probability of observing a certain set of hits, considering a given set of muon parameters is described in the next section. Probability density functions (PDFs), the maximum likelihood principle, a derived method called M-estimator and the minimum chi-square evaluation, which are both used by AartStrategy and ScanFit are also presented. Details of the tracking and energy reconstruction procedures, as well as results of their application to SIRENE events are discussed in subsequent subsections.

---

<sup>8</sup>A muon track is described by five independent parameters. Two parameters are necessary to define the position of the muon at a given time. Two angles, the zenith and azimuth angles describe its direction. The last parameter is the time.

#### 4.4.1 Probability Density Functions

The probability density function (PDF), which is denoted by  $f(\vec{y}|\vec{\Theta})$  describes the probability of observing the hits  $\vec{y}$  given a track  $\vec{\Theta} = (\vec{p}_\mu, \vec{d}_\mu)$ , with  $\vec{p}_\mu$  the position and  $\vec{d}_\mu$  the direction of the muon at a certain time.

If the hits are statistically independent, the PDF can be expressed as the multiplication of PDFs for individual hits [68]

$$f(\vec{y}|\vec{\Theta}) = \prod_{i=1}^N f_i(y_i|\vec{\Theta}) .$$

The probability of measuring a certain hit time depends on the muon track parameters and therefore on how the track and the optical modules (OMs) of the telescope relate to each other. As was discussed in Section 4.1, the PDF of a single hit can therefore be described in terms of the predicted hit time, the photon path length  $l$  and the angle of incidence  $\theta_{inc}$  of the photons on the OMs. The PDF can also be written as a function of a more convenient quantity: the time residual  $r_i = t_i - t_i^{th}$  between the observed time  $t_i$  and the predicted time  $t_i^{th}$  of hit  $i$ . The resulting PDF of all hits can thus be expressed by

$$f(\vec{y}|\vec{\Theta}) = \prod_{i=1}^N f_i(r_i|l_i(\vec{\Theta}), \theta_{inc,i}(\vec{\Theta}), A_i(\vec{\Theta})) . \quad (4.10)$$

The quantity  $A_i$  is the predicted amplitude of the hit  $i$ . It has been added to the list of quantities defining the PDF, since a hit is characterised by its time and amplitude.

#### Signal and Background

The PDF of the hit time residuals has contributions from both signal and background hits. The PDF of the signal is often parametrised with a continuous, differentiable function of the time residual which favor the use of optimisation methods based on maximum likelihood, minimum chi-square or M-estimate approaches. In those cases, the model prediction can be linearised by only considering signal hits and no background hits. In the last step of the reconstruction procedure only, after the iterative process has converged towards an unique solution, background hits are usually taken into account to give a more precise estimate of the muon track geometry. The PDF that describes the background hits is a constant function of the hit time, corresponding to a known rate of uncorrelated bioluminescence and  $^{40}\text{K}$  decay hits (usually 70 kHz).

The relative contribution of the signal and background hits is determined from the hit amplitude  $A_i$ , the photon path length  $l$  and the incident angle  $\theta_{inc}$  of the photons on the optical modules (OMs). The PDF of the hit residual  $r_i$  can

be expressed as a weighted sum of both the PDFs of signal and background hits such that

$$f_i(r_i|l_i, \theta_{inc,i}, A_i) = \frac{1}{N^{tot}} \left( N^{sig} f_i^{sig}(l_i, \theta_{inc,i}, A_i) + f_i^{bg}(l_i, \theta_{inc,i}, A_i) \right) \quad (4.11)$$

where  $N^{sig}$  is the number of signal hits and  $N^{tot}$  is the total number of hits in the event. Both  $N^{sig}$  and  $N^{tot}$  depend on  $l_i$ ,  $\theta_{inc,i}$ , and  $A_i$ . The number of signal and background hits is calculated from an empirical fit to simulated events. This ensures that the PDF is normalised for any value of  $l_i$ ,  $\theta_{inc,i}$  and  $A_i$ .

#### 4.4.2 Linear least square methods

##### Maximum Likelihood Principle

The estimate is given by the values that maximise the likelihood  $L(\vec{\Theta}|\vec{y})$  that the muon track  $\vec{\Theta}$  will cause the measured hits  $\vec{y}$ . The likelihood function is defined as

$$L(\vec{\Theta}|\vec{y}) = f(\vec{y}|\vec{\Theta})$$

where  $f(\vec{y}|\vec{\Theta})$  denotes the probability density function (PDF) that specifies the probability of observing the hits  $\vec{y}$  given the muon track  $\vec{\Theta}$ . According to the expression of the single hit PDFs in Equation 4.10, the likelihood can be expressed by

$$L\left(t_i^{th}, l_i, \theta_{inc,i}, A_i | t_i\right) = \prod_{i=1}^N f_i\left(t_i | t_i^{th}(\vec{p}_\mu, \vec{d}_\mu), l_i(\vec{p}_\mu, \vec{d}_\mu), \theta_{inc,i}(\vec{p}_\mu, \vec{d}_\mu), A_i(\vec{p}_\mu, \vec{d}_\mu)\right)$$

with  $\vec{p}_\mu$  the position and  $\vec{d}_\mu$  the direction of the muon tracks at a fixed time  $t$ .

##### Minimum Chi-Squared Estimate

This approach defines a Chi-Square ( $\chi^2$ ) merit function<sup>9</sup>:

$$\chi^2 = \sum_{i=1}^N \left( \frac{y_i - f(y_i|\vec{p}_\mu, \vec{d}_\mu)}{\sigma_i} \right)^2$$

with the same convention as for the maximum likelihood. The variable  $\sigma_i$  is the central deviation of the chi-square distribution. If the single hit PDFs are expressed in terms of time residuals, the chi-square function becomes:

$$\chi^2 = \sum_{i=1}^N \left( \frac{(t_i - t_i^{th}(\vec{p}_\mu, \vec{d}_\mu))}{\sigma_i} \right)^2.$$

The best fit parameters are determined by the minimisation of this expression over the muon parameter space.

---

<sup>9</sup>A merit function measures the agreement between the observed data and the fitting model for a particular choice of the parameters.

### M-estimator

The performance of the likelihood maximisation or the chi-square minimisation depends on the assumed distribution that has been chosen to describe the observed data. These approaches can thus become inefficient and biased when small departures from the idealised assumptions are found. In the case PDFs are a function of the hit time, points with large fluctuations of the time residuals appear, mainly due to light scattering, as seen in Figure 4.4. To minimise their effects on the fitting procedure, another estimator is used, the M-estimator. This is a so-called robust estimation which is insensitive to small deviations and irregularities from the idealised assumptions used. The following expression is minimised:

$$M = \sum_{i=1}^N g(r_i) \left( \frac{t_i - t_i^{th}(\vec{p}_\mu, \vec{d}_\mu)}{\sigma_i} \right).$$

with  $g(r)$  a function which ensures that the minimisation of  $M$  is also efficient for large residuals. The function is chosen to provide the desirable properties (in terms of bias and efficiency) of the M-estimator when the data are truly from the assumed distribution.

### 4.4.3 Track reconstruction with AartStrategy

The algorithm “AartStrategy” is used for the reconstruction of muon tracks with energies above 50 GeV. According to previous work [68], it can safely be used up to an energy of  $10^7$  GeV. The algorithm is optimised to reconstruct upward-going neutrinos and is therefore less suitable for downward-going events. The code was adapted so it could take into account the photon weights simulated by SIRENE.

### Probability Density Functions

To describe the signal, AartStrategy benefits from PDFs which have been developed for the first reconstruction algorithm [89] used by the ANTARES collaboration. These PDFs are parameterised by empirical fits to Monte Carlo simulations of muons traversing the telescope, with an energy ranging from  $10^2$  to  $10^5$  GeV, and assuming a flat  $E^{-1}$  power-law spectrum. The cross sections involved take into account all muon energy loss processes. Photons from electromagnetic (EM) showers are simulated. The peak of the distribution is fitted with a Gaussian function, while the tail is approximated by an exponential. These two functions are joined together by a third-order polynomial function.

However, background hits can degrade the performance of the track reconstruction. For this reason, PDFs in which background hits are taken into account have been developed and included in the final step of the fitting procedure [68].



In these improved PDFs, the signal is represented by the functions described above.

### Description of the procedure

The reconstruction procedure consists of four consecutive fitting algorithms, each of them improving the results of the previous step.

The first routine is a straight line fit of the spatial coordinates of the muon track, as a function of the hit time, called Linear Prefit. It is used as first step of the reconstruction algorithm since it does not require any starting position. The position of the hits are approximated by the most likely points of closest approach of the track to the optical modules (OMs). The points are estimated from the likelihood that a track at a certain distance from a PMT will cause a hit with the measured amplitude.

The second and third routines rely on the calculation of the time residuals between the hit time  $t_i$  obtained from the PMTs and the predicted arrival time  $t_i^{th}$  of the corresponding photons on the OMs. The best estimates of the track parameters are the values that maximise the quantity

$$Q = \sum_{i=1}^{i=N} g(r_i, \vec{\theta})$$

where  $r_i = t_i - t_i^{th}$  is the hit time residual for each hit  $i$  and  $g(r_i, \vec{\theta}) = \ln f(r_i)$ , with  $f(r_i)$  the PDF of finding a hit  $i$  with residual  $r_i$  as in Equation 4.10. Uncorrelated background hits are not taken into account. The PDFs describe the signal only. Due to the shape of the hit time residual distribution, the PDFs are relatively flat for large residuals. It is therefore rather difficult to find the maximum of the corresponding likelihood function. To overcome this problem, the third routine makes use of the M-estimator with  $g(r_i, \vec{\theta}) = -2\sqrt{1 + r_i^2/2} + 2$ , which is linear in  $r$  for large values of the residual. The accuracy of the reconstruction algorithm is improved by iterating the second and third routines with gradually improving start positions. The best track estimate at each step is the one for which the likelihood function has reached a maximum. The final track estimate is based on the Maximum Likelihood (ML) approach, using a PDF that takes the background hits into account. A quality cut based on the value of the likelihood function at the fitted maximum has been implemented to better discriminate between well-reconstructed (error on the reconstructed angle  $\alpha \leq 1^\circ$ ) and the badly-reconstructed events (error  $\alpha \geq 45^\circ$ ).

#### 4.4.4 Track reconstruction with ScanFit

##### Probability Density Functions

The PDF of hit  $i$  which describes the signal in ScanFit consists of a pure Gaussian distribution of a given width  $\sigma_i$  given by

$$f_i(\vec{t}_i, \vec{\Theta}) = \frac{1}{\sqrt{(2\pi\sigma_i)}} \exp \left[ -\frac{1}{2} \left( \frac{t_i - t_i^{th}(\vec{\Theta})}{\sigma_i} \right)^2 \right]$$

where  $\vec{\Theta}$  is the vector of the muon parameters. This approximation is useful when applied with least square fitting methods as it simplifies the optimisation procedures.

Since maxima are not affected by monotone transformations, one can take the logarithm of the associated likelihood to turn the product of individual PDFs into a sum. The likelihood function  $L(\vec{t}, \vec{\Theta})$  can be expressed as an equivalent logarithmic likelihood

$$L(\vec{t}, \vec{\Theta}) = \sum_i \ln f_i(\vec{t}_i, \vec{\Theta}) = \sum_i \left( -\frac{i}{2} \ln 2\pi - \ln \sigma_i - \frac{(t_i - t_i^{th}(\vec{\Theta}))^2}{2\sigma_i^2} \right).$$

As the first two terms of the root mean square are constant, the maximisation of the likelihood depends on the minimisation of the last term of the sum only. Instead of using a chi-square distribution for the minimisation, preference is given to an M-estimator, in order to reduce the influence of outliers. The function  $g(r)$  of the M-estimator method is taken to be

$$g\left(\frac{t_i - t_i^{th}}{\sigma_i}\right) = \ln \left( 1 + \frac{1}{2} \frac{(t_i - t_i^{th})^2}{\sigma_i^2} \right).$$

When accounting for background hits, ScanFit uses the complete PDFs with background hits which have been developed for Aart Strategy [68].

##### Description of the procedure

The algorithm used by the ScanFit reconstruction program has been modified to take into account the photon weights simulated by SIRENE. According to previous work [21], the ScanFit algorithm can be safely used up to an energy of  $10^7$  GeV. A preselection of the hits is made by scanning over the angular space parameters. Correlations between hits are searched for in about 170 pre-defined directions, requiring the standard 1D-Trigger conditions (see Chapter 2). A set of hits is obtained for each candidate direction. A linear prefit of the hits allows to give a first estimate of the best track positions and times. The problem is linear since the direction is fixed and M-estimator PDFs are used which do not take

background hits into account. A chi-squared estimate is constructed based on the previously selected hits, to determine the final muon parameters in each of the remaining directions. Finally the track candidates are ordered, according to the number of selected hits and the chi-square values. To improve the results, a final fit is thus made on all hits, using the complete PDFs with background hits.

#### 4.4.5 Energy Reconstruction

The algorithm used to calculate the energy of the muon is similar for both Aart-Strategy and ScanFit and was first developed by Alain Romeyer [97]. The algorithm was chosen in favor of two alternative methods [98] [99], since the Romeyer approach does not depend on the telescope geometry. The corresponding program has been modified to take into account the photon weights simulated by SIRENE. The quality of the reconstruction algorithm has been verified for energies up to  $10^7$  GeV [97], [68]. The mean muon energy loss (and thus the muon energy) in this approach is estimated by

$$\langle \frac{dE}{dx} \rangle = A_{tot} D_{\mu}^{-1} \left( \frac{1}{N_{PMT}} \sum_{i=1}^{N_{PMT}} \frac{A_g(\theta_{inc,i})}{l_{reco}} \exp(-l_{reco}/L_{water}) \right)^{-1} \quad (4.12)$$

with  $A_g(\theta_{inc,i})$  the angular acceptance of the optical module (OM) as a function of the angle of incidence  $\theta_{inc}$ ,  $l_{reco}$  the photon path length from the reconstructed track, and  $L_{water}$  the absorption length in sea water. The constant  $A_{tot}$  is the sum of the recorded amplitudes and  $D_{\mu}$  is the part of the track which is contained in the Can of the telescope. An empirical fit is made to determine the muon energy estimate using the average muon energy loss. This function does not extend to low energies, as below 100 GeV the estimate of the average muon energy loss is almost independent of the muon energy. Therefore, the energy reconstruction algorithm cannot be used for energies smaller than  $E_{\mu} = 100$  GeV.

#### 4.4.6 Performance of the Reconstruction algorithms

##### Track Reconstruction of simulated events

To evaluate the performance of the full simulation chain,  $N_{gen} = 10^9$  upward-going muon neutrinos were generated with GENHEN, assuming an AGN-like  $E^2\Phi = 10^{-6} \text{ GeV cm}^{-2} \text{ sr}^{-1} \text{ s}^{-1}$  power law spectrum at the surface of Earth, in the energy range  $10 - 10^7$  GeV. The produced muon tracks were passed to SIRENE and processed by the 3D-Trigger to search for time correlated hits in any direction, requiring a minimum of 5L1 local coincidences. The triggered hits were finally passed to the reconstruction program.

The performance of the reconstruction algorithm can be expressed by plotting the distribution of the reconstruction error  $\alpha_{\mu}$  defined as the angle between the

true direction of the muon track and the direction of the reconstructed track such that

$$\alpha_\mu = \cos^{-1} \left( \vec{d}_\mu \cdot \vec{d}_\mu^{reco} \right)$$

with  $\vec{d}_\mu$  the direction of the muon and  $\vec{d}_\mu^{reco}$  the direction of the reconstructed muon track. In the next paragraphs, results obtained with AartStrategy and ScanFit are presented.

**Results with AartStrategy** In Figure 4.10, the distribution of the reconstruction errors using AartStrategy is shown. As can be seen in the figure, a first peak appears in the distribution around  $\alpha_\mu = 0.1^\circ$  (well-reconstructed events) and a second one around  $\alpha_\mu = 85^\circ$  (badly-reconstructed events). About 61.4% of the events are reconstructed with an error on the direction smaller than  $10^\circ$  and 56.4% are reconstructed within  $1^\circ$  from the true track. When using KM3 for simulation of the detector response, these numbers are smaller [68]. A possible explanation is given below.

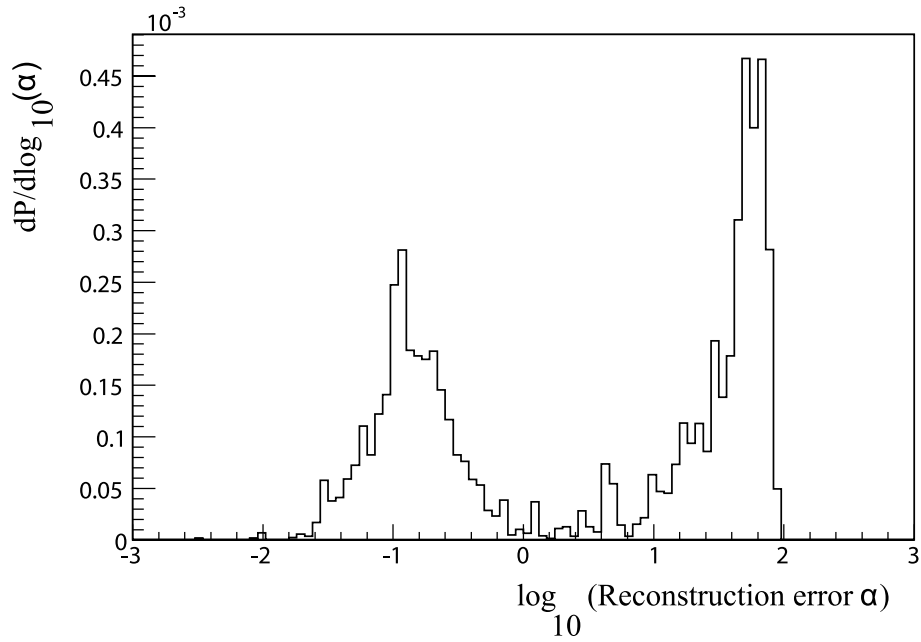


Figure 4.10: Distribution of the reconstructed error  $\alpha_\mu$  on the direction of the muon obtained with the AartStrategy procedure. Only upward-going events are shown.

In Figure 4.11, the error on the reconstructed position of the muon which is defined as the distance of closest approach between the true and the reconstructed muon tracks is shown. Even though the position of the muon track does not play a leading role in track reconstruction, this result is shown for completeness. As can be seen in the figure, most events are reconstructed within 1m from the true

muon track. A peak appears in the distribution around 0.2-0.3 m with a large tail. The tail disappears and the distribution becomes approximately Gaussian for events which were reconstructed within  $1^\circ$  of the true direction, demonstrating a correlation between the directional and the position errors. The same behaviour can be observed when using KM3 for the simulation of the detector response [68].

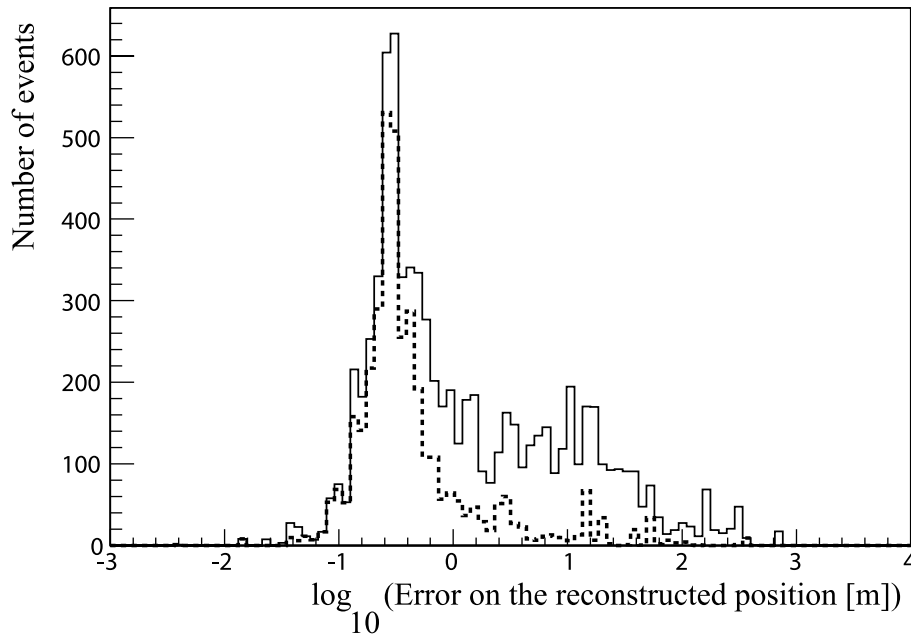


Figure 4.11: *Distribution of the reconstructed error  $\eta_\mu$  on the position of the muon obtained with AartStrategy. The distribution is shown for all events (solid line) and for the events which were reconstructed within  $1^\circ$  of the true direction (dotted line).*

The accuracy of the reconstruction depends on the four consecutive steps of AartStrategy. This can be seen in Figure 4.12 which shows the effect of the subsequent application of the linear pre-fit, the M-estimator and the ML method with the original PDFs.

Although the results improve at each step, the number of well-reconstructed events does not increase much. Still, the final fit using the full PDF functions with background clearly gives the best result. The last step would need a better starting position for the ML estimate to perform better. This behaviour was already observed in previous work on track reconstruction [68].

In order to enhance the reconstruction efficiency, the method used to choose the starting points needs improvement, by using a different function  $g(r)$  in the M-estimator. In addition, if the likelihood function yields multiple local maxima, the algorithm has difficulties to determine the global maximum. In most cases, it will converge to a local maximum which is close to the starting point. The ef-

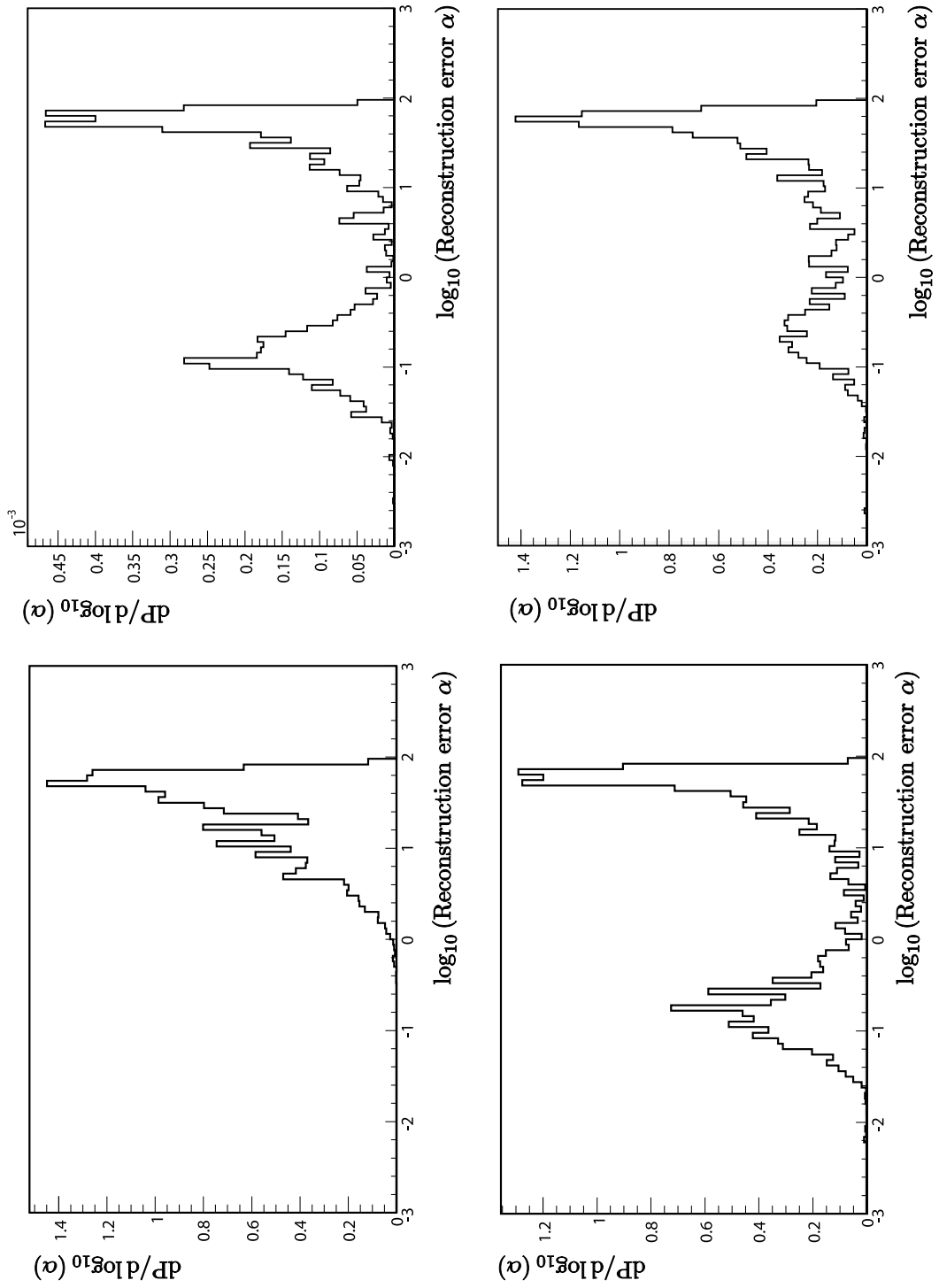


Figure 4.12: Distribution of the reconstructed error  $\eta_\mu$  on the direction of the muon obtained with the AartStrategy procedure. The performance of the linear prefit (top left), the M-estimator (top right), the maximum likelihood with the original PDFs (bottom left) and the final fit with the improved PDFs (bottom right) are shown separately.

efficiency of the ML estimate depends therefore on the starting point but also on the PDFs themselves. As seen in the previous section, the PDFs used in AartStrategy involve cross sections that describe the muon energy loss for energies below  $10^5$  GeV. Since SIRENE uses a high energy approximation for the muon cross sections and neglects the processes involved at low energy, the presently used PDFs are less suitable. Moreover, the PDFs strongly depend on the model that is used to determine the hit time, as well as the parameters which define the relations between the muon track and the optical modules (OMs) in the telescope. The calculations of the photon path length, but also the incident angle of the photons on the OMs and the amplitude of the hits differ in KM3/GEASIM and SIRENE. A different tracking algorithm, involving specific muon cross sections and medium properties is used as compared to the ones used for determining the PDF parametrisation. Hence, new PDFs need to be determined for reconstruction of SIRENE events using AartStrategy. The algorithm depends on many parameters, especially on the hit selection criteria and further tuning is required to improve its performance with the reconstruction of events generated using SIRENE.

Given the arguments above, it is not unreasonable to find that only about half of the events which survived the trigger selection are well-reconstructed using AartStrategy. This is sufficient to give an order-of-magnitude estimate of the performance of ANTARES in the energy range below  $10^7$  GeV. However, AartStrategy is not suitable for the reconstruction of neutrino events at energies above  $10^7$  GeV. For an optimal analysis of such data, a dedicated high energy reconstruction algorithm needs to be developed.

**Results with ScanFit** In Figure 4.13, the distribution of the error  $\alpha_\mu$  on the reconstructed direction is shown, as obtained for events simulated with SIRENE and reconstructed with the ScanFit algorithm. As can be seen in the figure, a first peak is observed around  $\alpha_\mu = 0.5^\circ$  and a second one at  $\alpha_\mu = 85^\circ$ . As for AartStrategy the first peak represents the well-reconstructed events, while the second peak corresponds to the badly-reconstructed events. About 63.5% of the triggered events are reconstructed within  $10^\circ$  of the true direction and 50.8% within  $1^\circ$ .

The ScanFit reconstruction program performs slightly better with SIRENE than AartStrategy. More events are well reconstructed. This can be attributed to the use of simple Gaussian PDFs (except for the final fit) by Scanfit. However, the ScanFit algorithm is less accurate than Aart Strategy since it has an angular resolution of almost  $0.5^\circ$  instead of  $0.1^\circ$ . This is a known behaviour of the program [21]. However, AartStrategy performs better in terms of angular accuracy. The same remarks concerning the PDFs and the various steps used in the reconstruction procedure which were made for AartStrategy also apply to ScanFit. The algorithm should be further tuned for a better performance with the reconstruction of events generated with SIRENE. Moreover, ScanFit is not suitable for ultra high energy simulations. An high energy reconstruction program needs to be

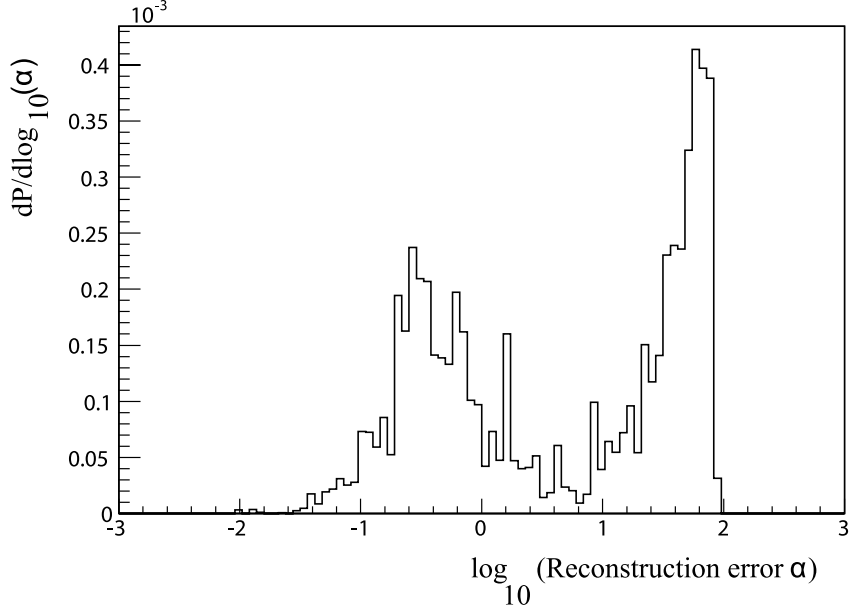


Figure 4.13: Distribution of the reconstruction error  $\alpha_\mu$  on the direction of the muon obtained for events simulated with SIRENE and reconstructed using the ScanFit procedure. Only upward-going muons are shown.

developed for use with SIRENE above  $10^7$  GeV.

### Energy Reconstruction results

In Figure 4.14 the distribution of the reconstructed muon energy is shown as a function of the true muon energy for events simulated with SIRENE. Muons from muon neutrinos were generated by ANIS in the energy range  $10 - 10^7$  GeV, following an AGN-like  $E^2\Phi = 10^{-6} \text{ GeV cm}^{-2} \text{ sr}^{-1} \text{ s}^{-1}$  power-law spectrum at the surface of the Earth. As can be seen in the figure, the muon energy is not well reconstructed for values of the true energy smaller than 100 GeV. The algorithm performs better at high energies (above  $10^4$  GeV). It is less accurate at low energies (below  $10^4$  GeV) where the reconstructed energy is biased towards higher values. This behaviour can be attributed to the reconstruction program [68], as several low energy events are not reconstructed. The program also does not take into account light from hadronic showers. This may play a role in the energy range considered. It can be concluded that the energy reconstruction algorithm used with SIRENE has a moderate accuracy for muon energies above  $10^4$  GeV, which is the energy domain of interest for our present study. However, a dedicated algorithm for the reconstruction of the neutrino energy above  $10^7$  GeV needs to be developed.



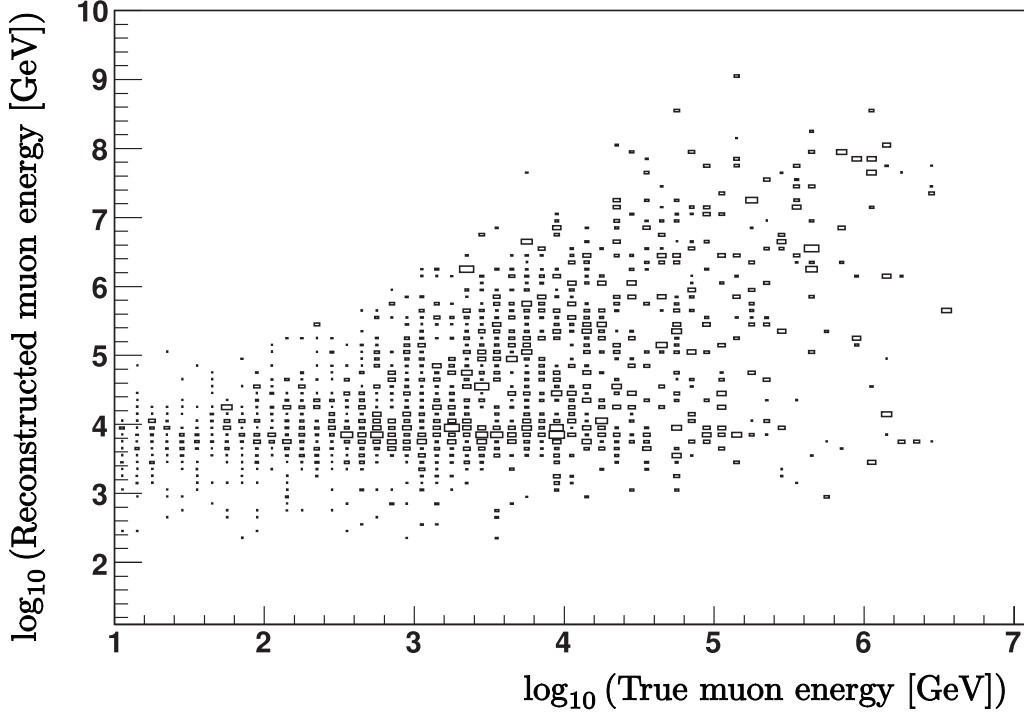


Figure 4.14: *Distribution of the reconstructed muon energy as a function of the true muon energy. Muons were generated by ANIS, following a muon-neutrino AGN-like spectrum at the surface of the Earth. The strategy described in [97] was used to estimate the muon energy of events simulated by SIRENE.*

## 4.5 Future extensions

To further improve the performance of SIRENE, several extensions of the program can be envisaged.

An important issue is the addition of electron and tau leptons as Cherenkov light sources into the program. Specific tracking methods for these particles also need to be developed.

Simulation of the muon energy loss at high energies should be extended with the implementation of electron-positron pair production and photo-nuclear interactions with the associated generation of hadronic showers. Continuous muon energy loss due to ionisation should be implemented for the use of SIRENE in low energy studies.

Concerning the photon tracking algorithm, one single distribution with correlated wavelengths and times should be determined, as the arrival times of the photons on the optical modules (OMs) of the telescope depend on the wavelength. Different wavelength and hit time distributions should also be implemented for both the direct and scattered photons. A parametrisation for the arrival time distribution of the photons which scatter with a wide angle and reach

### *Detector simulation and Track reconstruction*

the OMs with a relatively long time delay needs to be implemented.

For a proper reconstruction of UHE muon tracks generated, new PDFs have to be determined for use in the reconstruction programs.

## Chapter 5

# High Energy Simulations Results

*The sensitivity of the ANTARES telescope to a diffuse flux of cosmic neutrinos with energies above  $10^7$  GeV has been estimated using the newly developed chain of simulation programs. An average upper limit of the event rate is determined and the corresponding effective areas for neutrinos are presented.*



he study of the diffuse neutrino flux that originates from discrete sources which cannot be individually resolved, or from interactions of cosmic rays with intergalactic matter or radiation, may yield important cosmological information. Such measurements are of particular interest for neutrino energies in excess of  $10^{16}$  eV, in the so-called ultra high energy (UHE) range. Indeed, the origin of UHE neutrinos and the associated high energy cosmic rays has remained a mystery for many years (see Chapter 1). Recent results appear to correlate extragalactic supermassive black holes at the center of nearby active galaxies with the observation of UHE cosmic rays on Earth. The detection of UHE neutrinos will provide crucial information on the sources of UHE cosmic rays and the processes involved in the production of such extremely energetic particles.

Above  $10^7$  GeV, the Earth is opaque to muon neutrinos. At the same time the neutrino interaction probability is still insufficient for the limited mass of sea water above the telescope to yield a reasonable event rate. Hence, only horizontally traveling neutrinos have a chance of being detected in an underwater neutrino telescope.

When searching for neutrinos in the UHE domain, the background consists of atmospheric muons which can reach the detector. They are produced in large air showers by interactions of cosmic ray primaries with the Earth's atmosphere. Especially multiple atmospheric muons in a short time slot can be mis-reconstructed

as secondary leptons from charged-current deep-inelastic neutrino scattering interactions. The distribution and intensity of the atmospheric muons therefore need to be known in order to discriminate this large background from the UHE neutrino signal.

The techniques usually employed for neutrino searches (see Chapter 2) need to be reconsidered when looking for UHE neutrinos. The Earth cannot be used as a shield against downward-going atmospheric muons. Moreover, the reconstruction algorithms typically used by ANTARES are optimised<sup>1</sup> for muon energies lower than  $10^5$  GeV and not necessarily suited for the reconstruction of UHE muon tracks. However, trigger selections and cuts on the energy and zenith angle can be applied, based on the expectation that the signal is dominated by the downward-going, almost horizontal direction, while the background is mostly vertically downward-going.

The generation of UHE neutrino interactions and the subsequent response of the detector to these events are simulated using the dedicated high energy Monte Carlo programs described in the previous chapters of this thesis. Details on the actual simulations for UHE neutrinos are given in the next section. The proposed strategy to discriminate between the penetrating UHE neutrino events and the atmospheric background is presented in Section 5.2 which also includes a calculation of the upper limit for UHE neutrino detection with ANTARES and a comparison to existing upper limits. The chapter is concluded with a discussion on these results.

## 5.1 Monte Carlo simulations

### 5.1.1 Ultra high energy neutrino simulation

The Pierre Auger Observatory has found evidence suggesting that Active Galactic Nuclei (AGN) are likely sources of the highest energy cosmic rays [13]. The present study therefore focuses on diffuse neutrino fluxes from AGN and the simulations are based on assumed AGN-like neutrino spectra.

At the energies of interest for this analysis, the values of the interaction cross section for neutrinos and anti-neutrinos are nearly identical (see Chapter 4). Hence, only neutrinos need to be considered. The Monte Carlo program ANIS [74] has been used to generate a flux of  $10^5$  muon neutrinos and their interactions in the media surrounding the ANTARES telescope. The simulation assumes a generic AGN-like spectrum of the form  $E^2\Phi = 10^{-6}\text{GeV cm}^{-2}\text{s}^{-1}\text{sr}^{-1}$ , for energies ranging between  $10^4$  GeV and  $10^{11}$  GeV. Muons produced in charged-current interactions are propagated towards the telescope using the program MMC [50].

---

<sup>1</sup>The Probability Density Functions (PDFs) describing the signal distribution accounting for uncorrelated background hits are empirical fits to Monte Carlo simulations of muons with energies between  $10^2$  and  $10^5$  GeV. See Chapter 4.

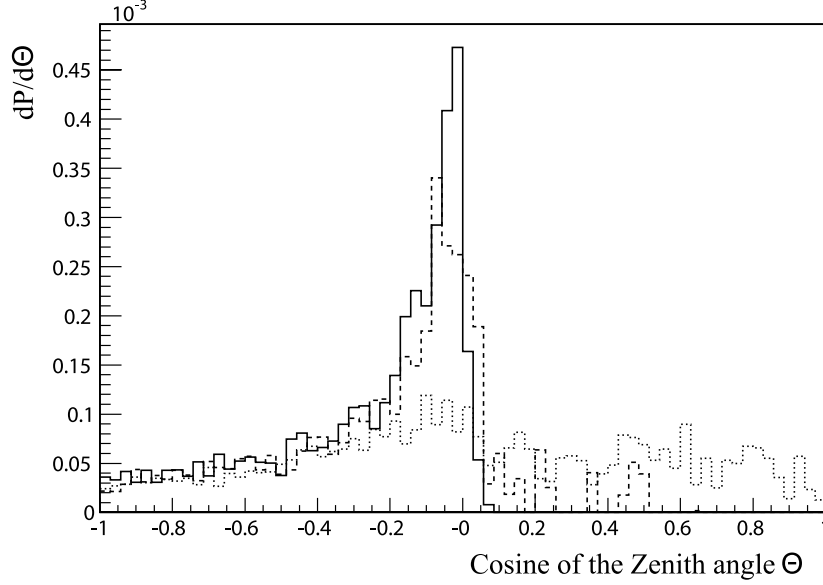


Figure 5.1: *Distribution of the cosine of the zenith angle for neutrinos which can produce a muon able to reach the detector. Neutrino interactions were simulated with ANIS, assuming an AGN-like spectrum. Muon secondaries were propagated to the default Can of ANTARES with MMC. The probability distribution is shown for neutrinos with an energy below  $10^7$  GeV (dotted), between  $10^7 - 10^9$  GeV (dashed), and  $10^9 - 10^{11}$  GeV (solid line). In the ANTARES reference frame, a zenith angle of  $0^\circ$  corresponds to an upward-going neutrino, while an angle of  $180^\circ$  corresponds to a downward-going neutrino.*

In Figure 5.1, the distribution of the cosine of the zenith angle of the generated muon neutrinos is shown, for various energy ranges. Only events which can produce a muon able to reach the detector Can (see Chapter 2) are shown. As can be seen in the figure, the generated neutrino events concentrate near the horizon as the energy increases. This is expected as the Earth becomes opaque to UHE neutrinos and the path length through the atmosphere and the sea water is longest in the horizontal direction. A major fraction of muons from UHE neutrinos will therefore reach the detector in the downward-going, horizontal direction. In the present analysis, only downward-going events will thus be considered.

The detector simulation program SIRENE (see Chapter 5) has been used to determine the photon field and the hits in the telescope. In Figure 5.2, the event rates are shown (with a solid line), as a function of the muon energy for those events which could produce a detectable signal. In the figure, only downward-

<sup>3</sup>The energy spectrum of cosmic rays primaries follows an  $E^{-2.7}$  spectrum for energies below  $10^{15}$  eV (the knee) and above  $10^{19}$  eV (the ankle). In between these two limits, it is proportional to an  $E^{-3}$  spectrum. Since this work focuses on the highest energies, the cosmic ray energy spectrum has been approximated with an  $E^{-2.7}$  energy spectrum.

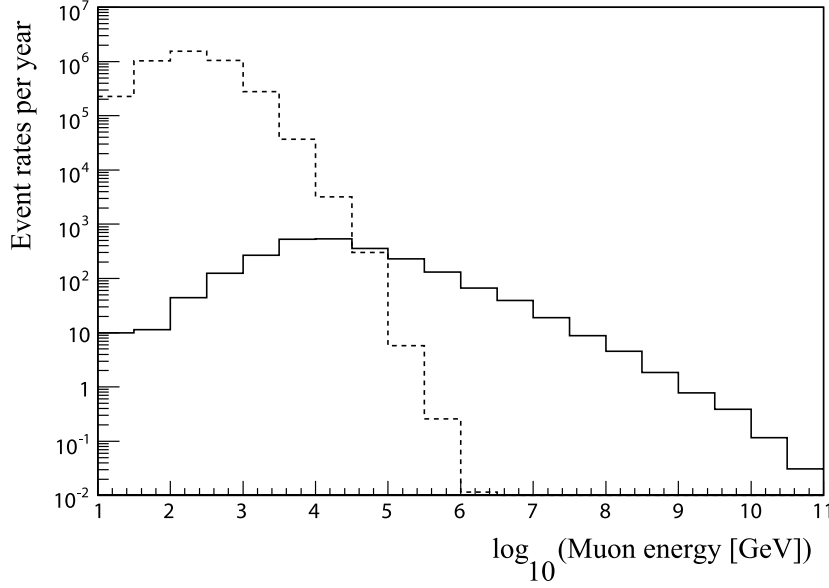


Figure 5.2: Energy distribution of muons from downward-going ultra high energy (UHE) astrophysical neutrino (solid) and cosmic ray (dashed) interactions in the atmosphere. Only events which can reach the detector are shown. The UHE events have been simulated using ANIS, assuming an AGN-like spectrum. The atmospheric muons have been simulated using MUPAGE. The atmospheric spectrum has been extrapolated<sup>3</sup> beyond 500 TeV, assuming an  $E^{-2.7}$  spectrum.

going events have been used and the ANTARES twelve line geometry is assumed.

### 5.1.2 Atmospheric muon background simulation

The spectrum of atmospheric muon bundles impinging on the ANTARES detector surface has been simulated with the program MUPAGE [100] or MUon Generator from PArametric formulas. MUPAGE is a parametrisation of the atmospheric muon flux at the depth of the detector, simulating single and multiple underwater muons between 20 GeV and 500 TeV and up to  $85^\circ$  zenith angle. All kinematic parameters of the muons are tuned with a Monte Carlo simulation of primary cosmic ray interactions and shower propagation in the atmosphere, based on the program HEMAS [101]. It allows the calculation of the high energy muon component ( $E \geq 500$  GeV) in extensive air showers (EAS) assuming a primary total energy between  $10^{12}$  and  $10^{20}$  eV. Hadronic interactions are handled with DPMJET [102] which embodies a phenomenological model [103], using results from direct and indirect measurements of cosmic rays in the energy range between 10 GeV and 1 EeV. Direct observations are used to extrapolate the energy spectra of each element to high energies. The muons which could reach the sea

level are then transported through water, towards the telescope with the lepton propagator MUSIC [70] (see Chapter 4).

A total number of  $10^5$  downward-going atmospheric events, consisting of bundles of at most 1000 muons have been generated with MUPAGE, in the energy range 20 GeV - 500 TeV at the default ANTARES Can (see Chapter 4), for zenith angles with  $-1 \leq \cos \theta \leq -0.087$ . The detector simulation program SIRENE has been used to determine the resulting photon hits in the telescope. In Figure 5.2,

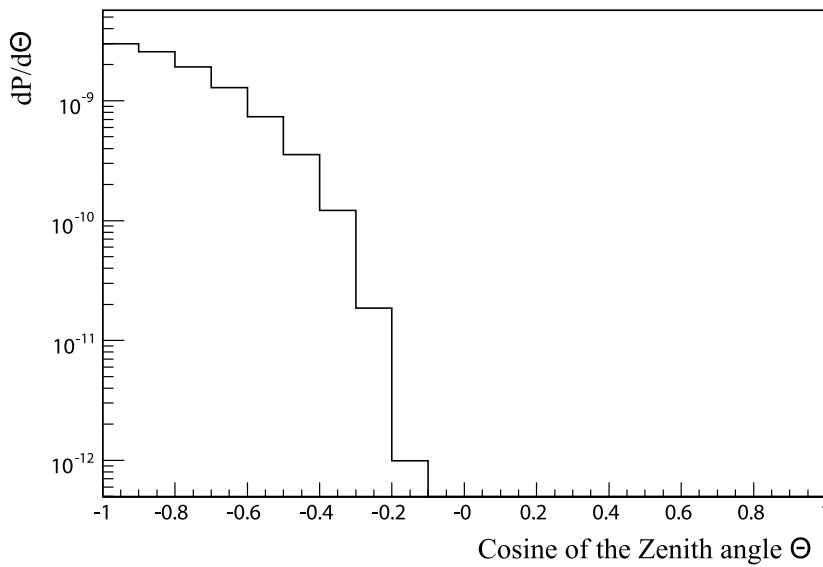


Figure 5.3: *Distribution of the cosine of the zenith angle for atmospheric muons which could reach the detector. The events have been simulated using MUPAGE. In the ANTARES reference frame, a zenith angle of  $0^\circ$  corresponds to an upward-going muon, while an angle of  $180^\circ$  corresponds to a downward-going muon.*

the event rates are shown (with a dashed line), as a function of the muon energy, for those events which could produce a detectable signal. As can be seen in the figure, the distribution drops rapidly with increasing energy.

In Figure 5.3 the distribution of the cosine of the zenith angle is shown for atmospheric muons which could produce a detectable signal. As can be seen in the figure, most atmospheric muons reach the detector from the vertical downward-going direction. Such a spectrum is limited to an angular range of approximately  $\cos \theta \leq -0.10$ .

## 5.2 Data selection and analysis

A dedicated data analysis method needs has been developed in order to reduce the amount of atmospheric muon background while preserving sensitivity to the

ultra high energy (UHE) signal. Using this analysis method, an estimate can be made of the upper limit that can be achieved with ANTARES on the assumed astrophysical neutrino flux.

### 5.2.1 Track energy estimate

As can be seen in Figure 5.2, the muon energy spectrum expected from an AGN-like neutrino flux at the detector extends to larger values than that of the atmospheric muons. Thanks to the steeper slope of the atmospheric spectrum, the signal over background ratio improves with energy. In principle, it is thus possible to search for an excess of astrophysical neutrinos at higher energies. Since for ANTARES no reconstruction program is available for ultra high energy muons, the reconstructed muon energy cannot be easily used to distinguish muons induced by cosmic neutrino interactions from atmospheric muons. On the other hand, the muon energy can be estimated [89] from the muon energy loss on its way to and through the telescope (see Chapter 5). In fact, the amount of light emitted by the muons and the associated electromagnetic showers provides an indirect measure of the muon energy. It should be realized though that the number of photons hitting the photo-multiplier tubes (PMTs) in the telescope depends strongly on the position of the track relative to the telescope (see Chapter 5). The amount of light observed in the telescope thus needs to be combined with position and direction information to estimate the muon energy, without having to rely on a full geometrical reconstruction.

As discussed in Chapter 3, the trigger software simulates the digitisation of the hits by the front-end chips (ARS) of the PMT. It also translates the recorded amplitude (AVC), time (TVC) and position of the digitised hits into calibrated information which can be used for further analysis. The calibrated amplitude is determined using a linear dependency of the recorded AVC value on the number of photo-electrons [25]. The calibrated signal amplitude in the PMT is thus proportional to the number of detected photo-electrons.

In Figure 5.4, the distribution of the estimated total charge of the hits induced in the telescope by the simulated AGN-like muon neutrino spectrum is shown, as a function of the (true) initial muon track energy. The distribution is also shown for a generic  $E^{-1}$  spectrum, for comparison. The muon energy considered in the figure is the energy of the incoming muon at the surface of the default Can volume of ANTARES (see Chapter 2). The total charge of the hits in an event has been estimated by taking the sum of the calibrated hit amplitudes in every PMTs of the telescope. As expected, the distribution shows a correlation between the true muon energy and the digitised charge of the signal. Despite the width of the distribution, the total charge is seen to increase proportionally with the energy up to about  $10^6$  GeV. Above this energy, the distribution becomes flatter due to the signal integration of the front-end chips of the PMT. The ensemble of PMTs which constitute the telescope is seen to saturate when receiving a charge



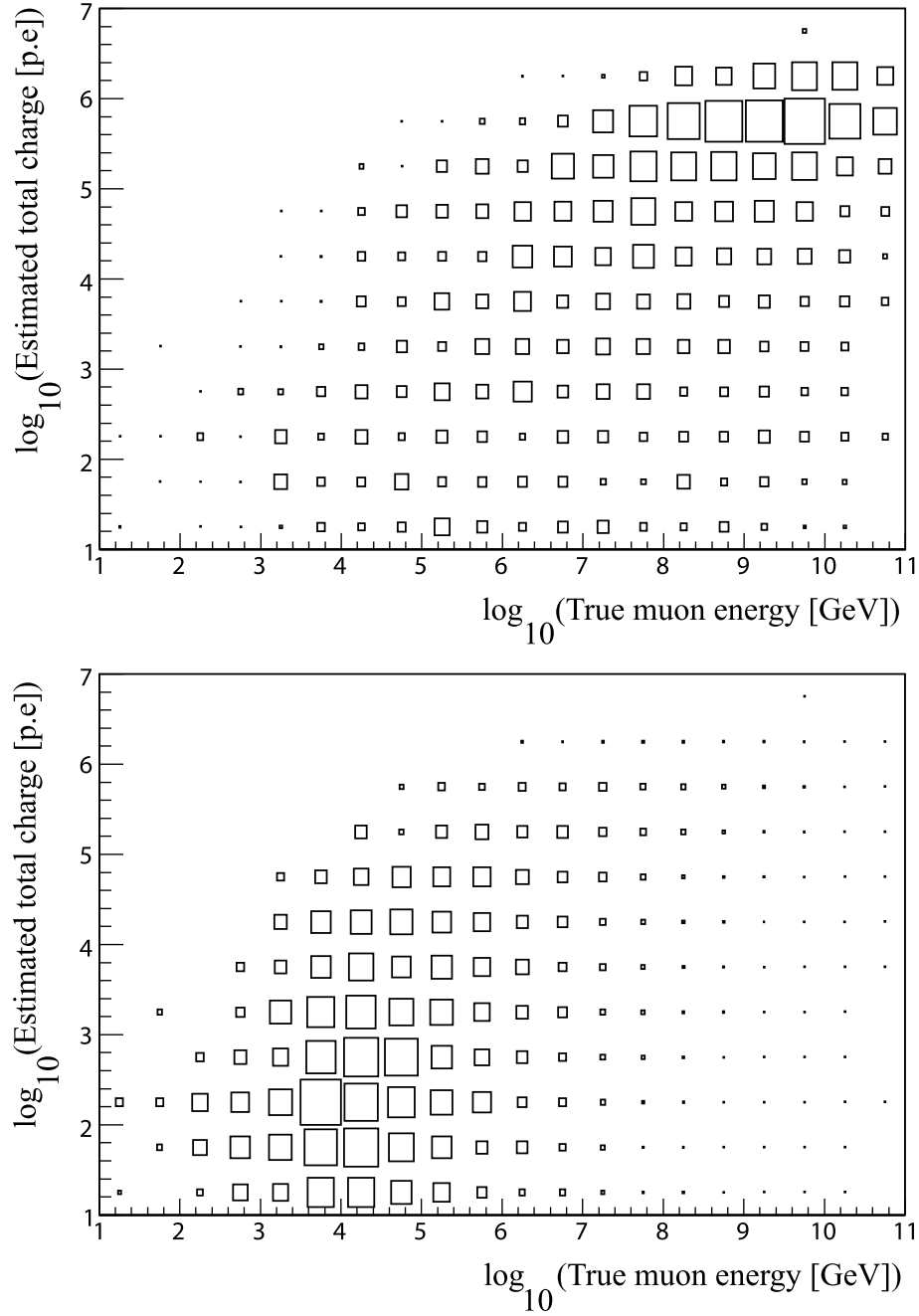


Figure 5.4: Distribution of the total charge of the hits produced by one event as a function of the (true) muon track energy. The energy distribution is assumed to follow an AGN-like spectrum (bottom). The same distribution is also shown for a generic  $E^{-1}$  spectrum (top), for illustrative purposes. Downward-going events simulated with SIRENE are shown at the trigger level.

larger than about  $10^6$  photo-electrons (p.e). The performance of the PMT thus limits the readout of a large charge. However, the true muon energy is still a determining factor in the observed charge. The total charge of the digitised hits is therefore chosen as an estimate of the muon energy, without having to rely on track reconstruction.

### 5.2.2 Uncorrelated background and triggering

ANTARES does not only record hits from astrophysical and atmospheric muons, but also from the decay of  $^{40}\text{K}$  and bioluminescence (see Chapter 2). While hits from high energy muons are related in time and position, as a consequence of the properties of Cherenkov light emission, hits due to  $^{40}\text{K}$  and bioluminescence are uncorrelated. The trigger software is used to separate these isolated hits from the ones created by astrophysical and atmospheric muons. In this work, a background rate of 70 kHz<sup>4</sup> due to  $^{40}\text{K}$  and bioluminescence has been added to the ultra-high energy (UHE) signal and the atmospheric background (see Chapter 5 for details). A three-dimensional trigger (trigger 3D) is used to search for time correlated hits. A hit is in local coincidence if it is within 20 ns of another hit, on a different optical module (OM), at the same storey. These coincident hits are referred to as “L1” events. Only events with a sufficient number of correlated hits are selected for further analysis, while the others are being discarded. This is motivated by the assumption that high energy muons induce multiple hits in the telescope, while uncorrelated background will mainly produce single hits. Since a muon track is defined by five independent parameters, a minimum of five local coincidences (“5L1”) is required. Coinciding hits on the same photo-multiplier tube (PMT) will generally result in a single hit with a large charge of typically 2.5 photo-electrons (p.e.) or more. Consequently, events with hits having a large charge are also included in the aforementioned L1 events.

The 3D trigger is suitable for UHE analysis. Since UHE muons induce large photo-electron hits in the PMTs, the trigger will select them irrespective of the number of local coincidences involved. The minimum of five correlated hits in the telescope has been shown to be sufficient to separate the hits due to atmospheric muons from those from uncorrelated background [21]. This selection will also improve the distinction between hits induced by UHE muons and the uncorrelated background. The resulting event rates are shown in Figure 5.5. Compared with the event rates shown in Figure 5.2, the background has been reduced as hits due to  $^{40}\text{K}$  decay and bioluminescence are now removed. However, at trigger level, no distinction can be made between events from atmospheric muons or cosmic neutrinos. Atmospheric muon bundles can spread over a large area and hit many optical modules (OMs) within a time window of a few nanoseconds [100], [104]. The trigger can therefore wrongly identify them as correlated

---

<sup>4</sup>The average uncorrelated background rate observed in situ.

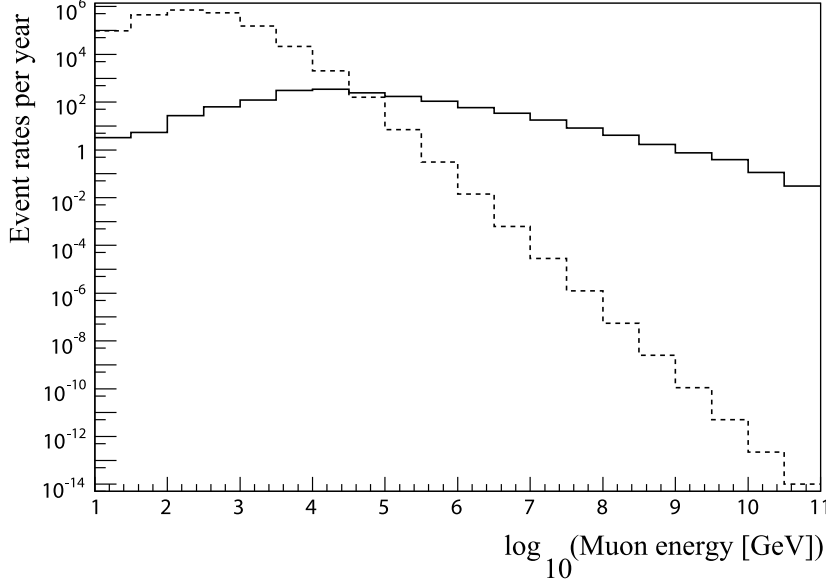


Figure 5.5: *Muon energy distribution at the trigger level induced by downward-going ultra high energy (UHE) astrophysical neutrinos (solid) and cosmic rays interaction in the atmosphere (dashed). SIRENE was used to simulate the UHE signal, while MUPAGE was used to generate the atmospheric muons. Events with a minimum of five local coincidences (at the same storey) or a large amplitude on one of the storeys are shown. The astrophysical neutrino flux corresponds to an AGN-like spectrum. The atmospheric spectrum has been extrapolated for energies above  $10^5$  GeV with an  $E^{-2.7}$  spectrum, following the primary cosmic ray spectrum at UHE.*

hits from a single muon. Further analysis is necessary to improve the separation of the signal and the atmospheric background at the trigger level.

### 5.2.3 First event selection

Differences between the ultra high energy (UHE) signal and the atmospheric muon background can be exploited for data analysis. The main differences rely on the direction from which the muons arrive at the detector, and the energy of the muon which is estimated by the charge of the hits induced in the photomultiplier tubes (PMTs). In Figure 5.6, the distribution of the cosine of the zenith angle as a function of the total charge of the hits in an event is shown, for both the UHE signal and the background events. As can be seen in the figure, downward-going UHE muons concentrate near the horizon ( $\cos \theta \approx 0$ ), whereas the direction of atmospheric muons is mainly vertical ( $\cos \theta \approx -1$ ). Even though the charge induced by atmospheric muons is rather large (up to about  $10^4$  photo-electrons), the hits from UHE muons give an even larger charge (up to about  $10^{6.5}$  photo-

## High Energy Simulations Results

electrons). These observations suggest that the atmospheric background can be rejected by excluding events with vertical directions and relatively low charge values.

### Cut on the zenith angle

In figure 5.7, the distribution of the cosine of the muon zenith angle is shown for both signal and background events, at the trigger level.

As can be seen in the figure, atmospheric muons are peaking in the vertical direction and dominate over the astrophysical neutrino signal over almost the entire zenith angle range, with the exception of horizontal events in the range  $-0.2 \leq \cos \theta \leq 0$ . A loose cut is placed on the zenith angle at  $\cos \theta \geq -0.6$  to reject the atmospheric vertical events while most signal events are kept.

### Cut on the total charge of the hits

In Figure 5.8, the distributions of the total charge of the hits induced by ultra high energy (UHE) signal events and atmospheric background events are shown, at the trigger level. As for the muon energy spectrum, the distribution of atmospheric events has been extrapolated beyond  $10^{4.5}$  photo-electrons (p.e.) with a power-law spectrum  $E^{-2.7}$ , following the primary cosmic ray spectrum. The distribution has thus been estimated up to  $10^{6.5}$  p.e.

As can be seen in the figure, the distribution of UHE muons extends to a larger induced charge in the photo-multiplier tubes (PMTs) of the telescope than that of atmospheric muons. Both signal and background can induce a total charge up to  $10^{6.5}$  p.e. A loose cut is placed at  $10^4$  p.e. to reject events with low charge values which are mostly entirely due to atmospheric background.

## 5.2.4 Expected rates and neutrino flux limit

After selecting events with a charge larger than  $10^4$  photo-electrons (p.e.) and a zenith angle such that  $\cos \theta \geq -0.6$ , the remaining simulated event rates per year have been determined. Figure 5.9 shows the event rates as a function of the estimated total charge of the hits (top) and the cosine of the zenith angle (bottom), after the cuts have been applied. As can be seen in the figure, the selection criteria reduce the number of background events but may require further optimisation.

In order to determine an experimental limit on a flux, the (maximum) number of signal events needs to be known as a function of the number of observed events and expected background, after all selection cuts have been applied. The upper limit on a source flux  $\phi(E_\nu)$  is thus calculated as

$$\phi(E_\nu)_{90\%} = \phi(E_\nu) \frac{\mu_{90}(N_{obs}, N_b)}{N_s} \quad (5.1)$$

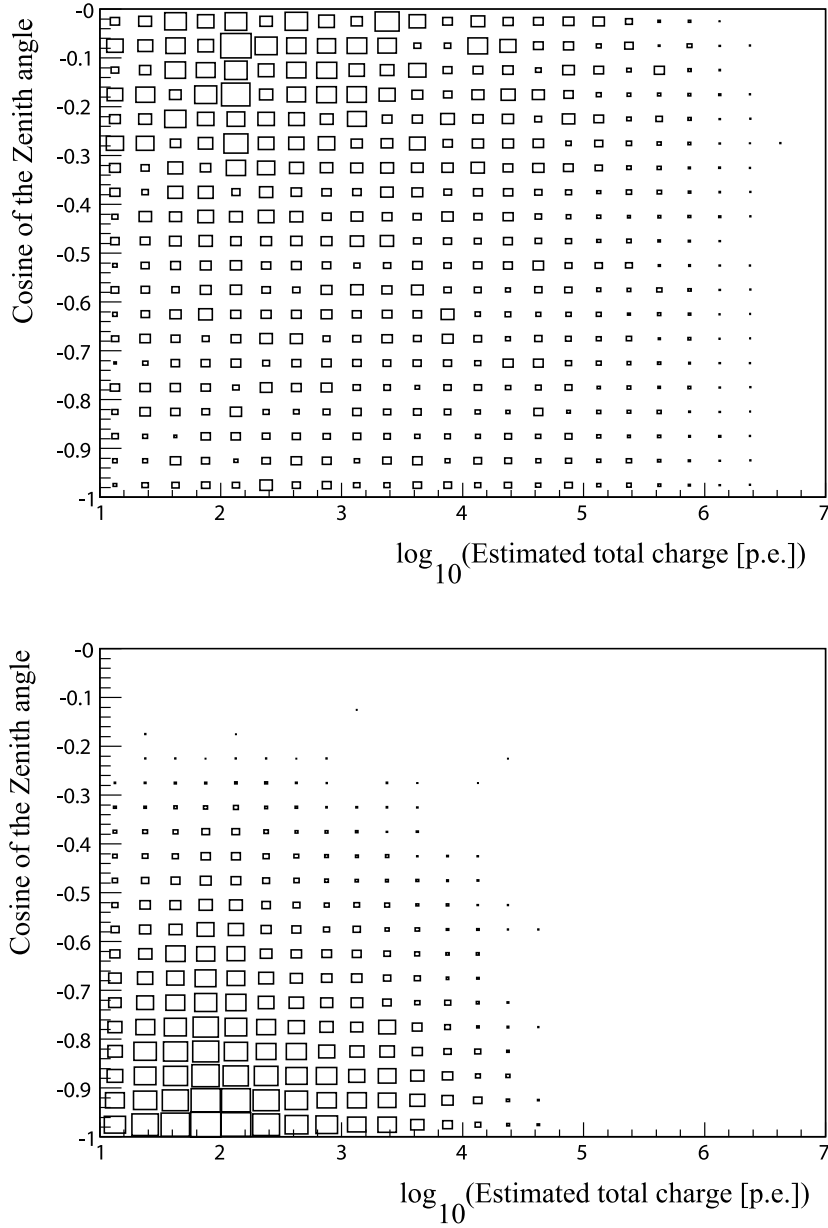


Figure 5.6: Event distribution as a function of the total charge observed in the neutrino telescope and the cosine of the zenith angle for downward-going UHE neutrino-induced muons (top) and atmospheric background muons (bottom), at the trigger level. Signal events were simulated with SIRENE. The atmospheric muon background was simulated with MUPAGE.

## High Energy Simulations Results

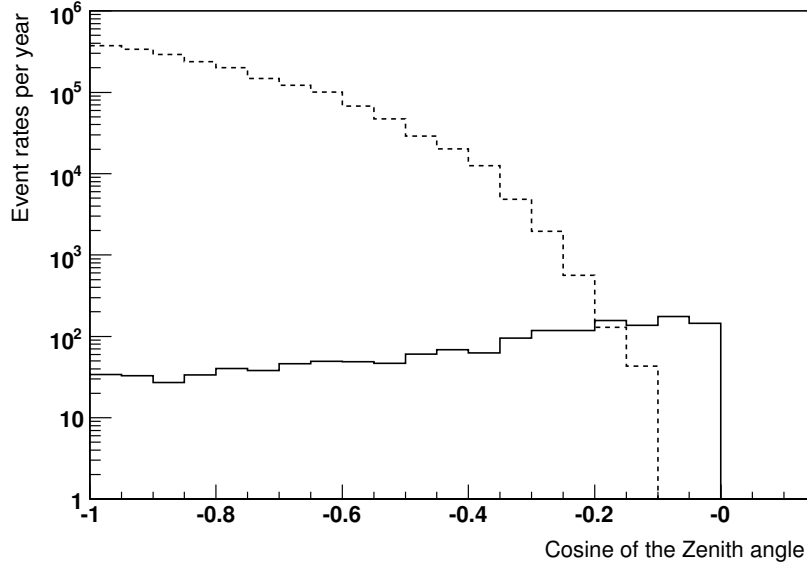


Figure 5.7: Distribution of the cosine of the zenith angle (rates per year) for atmospheric muons (dashed) and muons induced by downward-going UHE astrophysical neutrinos (solid) at the trigger level.

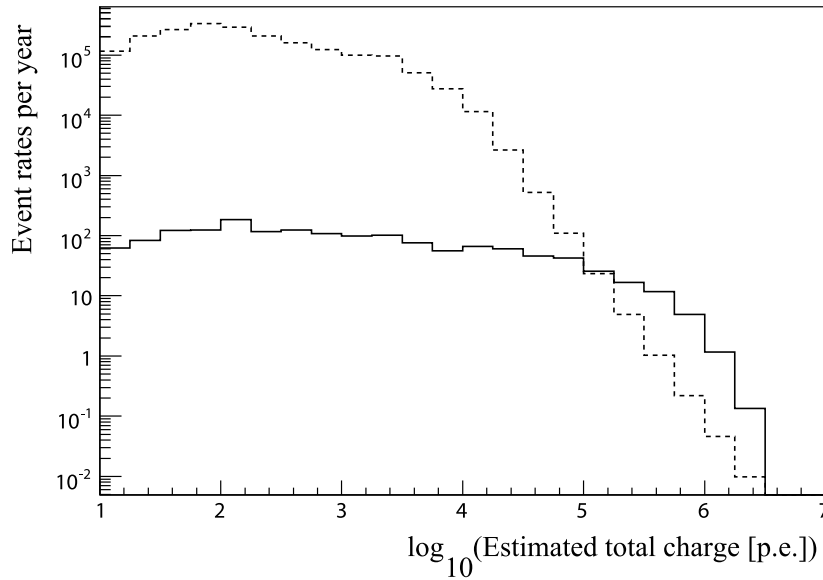


Figure 5.8: Distribution of the total charge (in p.e.) of the digitised signal induced by downward-going ultra high energy (UHE) neutrinos (solid) and atmospheric muons (dashed) at the trigger level. The astrophysical neutrino flux corresponds to an AGN-like spectrum. The atmospheric spectrum has been extrapolated to higher charge values assuming an  $E^{-2.7}$  spectrum, following the primary cosmic ray spectrum at UHE.

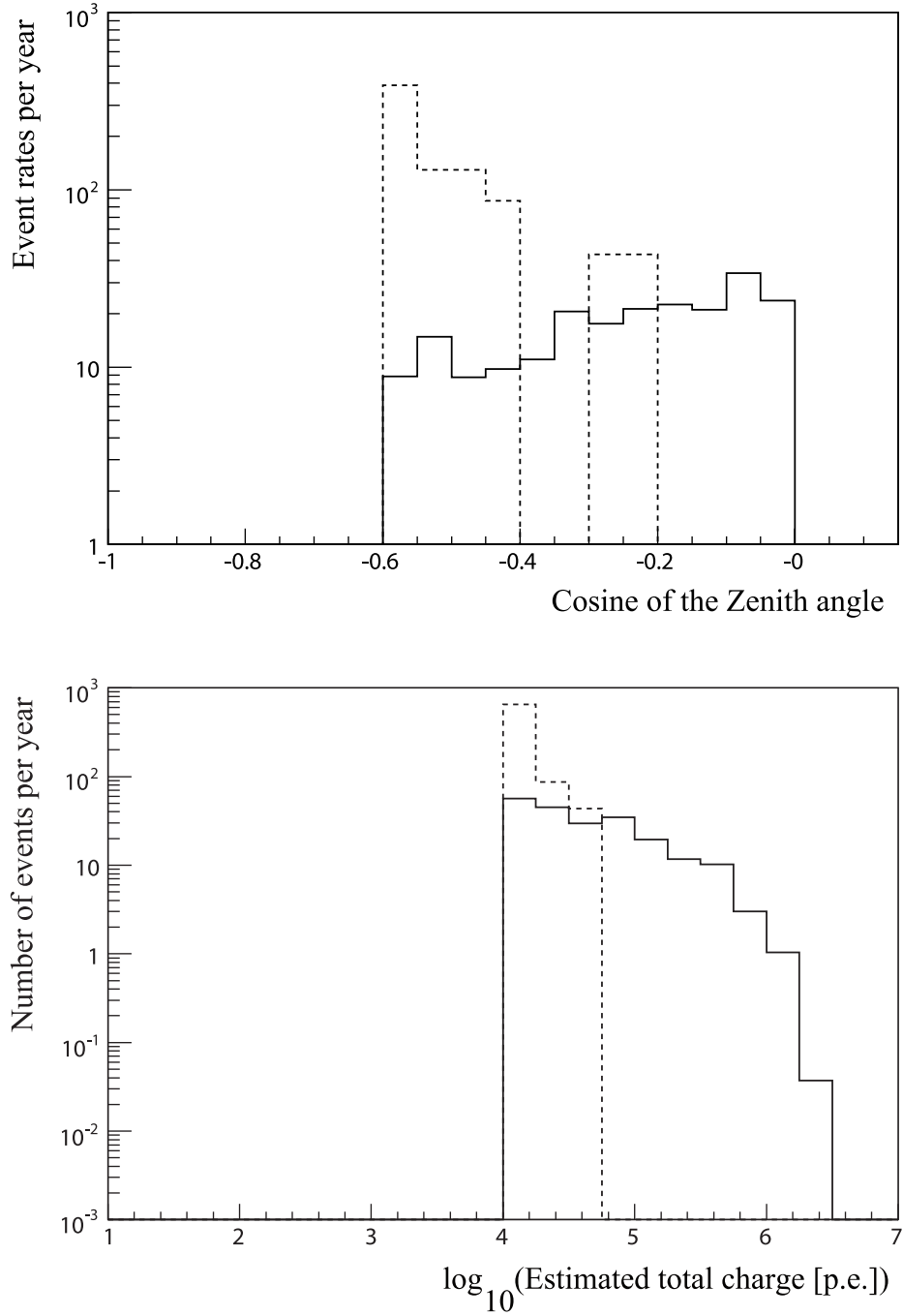


Figure 5.9: Distributions of the cosine of the muon zenith angle (top) and the total charge of the hits (bottom) induced in the telescope by atmospheric muon background (dashed) and cosmic downward-going UHE neutrinos (solid). Only those events which survived both cuts mentioned in the text are shown.

## High Energy Simulations Results

where  $\mu_{90}(N_{obs}, N_b)$  is the 90% confidence interval as a function of the number of observed events  $N_{obs}$  and the expected background  $N_b$ . The variable  $N_s$  is the total number of signal events.

The event rates shown in Figure 5.9 need to be integrated to determine the number of expected signal events  $N_s$  and background events  $N_b$  above a given value of the total charge of the hits and the cosine of the zenith angle. These integrated distributions are shown for the cosine of the muon zenith angle in Figure 5.10 (top) and for the total charge of the hits in Figure 5.11 (top). The simulated background rates are relatively small and their fluctuations can be described by Poisson statistics. For this specific situation, the method proposed by Feldman and Cousins [105] can be used to calculate the average upper limit that would be observed after hypothetical repetition of the experiment. Table XII<sup>5</sup> of reference [105] is used to determine the average upper limit of the signal (which Feldman and Cousins refer to as sensitivity) at the 90% confidence level (CL), that would be obtained over an ensemble of experiments with no true signal ( $N_s = 0$ ), for each value  $N_b$  of the simulated background. The resulting average upper limit at the 90% CL is shown as a function of the muon zenith angle in Figure 5.10 (bottom) and as a function of the total charge of the hits in Figure 5.11 (bottom). As can be seen in the figure, the average upper limit is enhanced towards 2.44 events ( $N_b = 0$ ) at the highest zenith angle and charge values.

### 5.2.5 Model rejection potential

The method proposed by G. Hill and K. Rawlins [106] has been used to optimise the experimental cuts and develop a stronger upper limit on the AGN-like neutrino flux model studied. The method is based on signal and background expectations from Monte Carlo simulations. It is used to place the strongest constraints on theoretical signal models. It is therefore suitable for this analysis.

The final selection values are the ones which minimise the ratio of the average upper limit over the expected signal from the model, i.e. the “model rejection potential” or “model rejection factor”

$$MRF = \frac{\bar{\mu}_{90}(N_b)}{N_s}.$$

The model rejection factor is shown in figure 5.12 as a function of the muon zenith angle and the total charge of the hits, for the simulated signal and background. The model rejection factor reaches a minimum for  $\cos \theta = -0.2$  and a total charge of the hits  $NPE = 10^5$  photo-electrons (p.e). The best constraints on the simulated

---

<sup>5</sup>The table gives upper limits for background rates up to 15. A linear interpolation has been used to determine the 90% upper limit within the range of given background rates. For values of the expected background larger than 15, an extrapolation has been used, assuming the statistical fluctuations are of order  $\sqrt{N_b}$  [55].



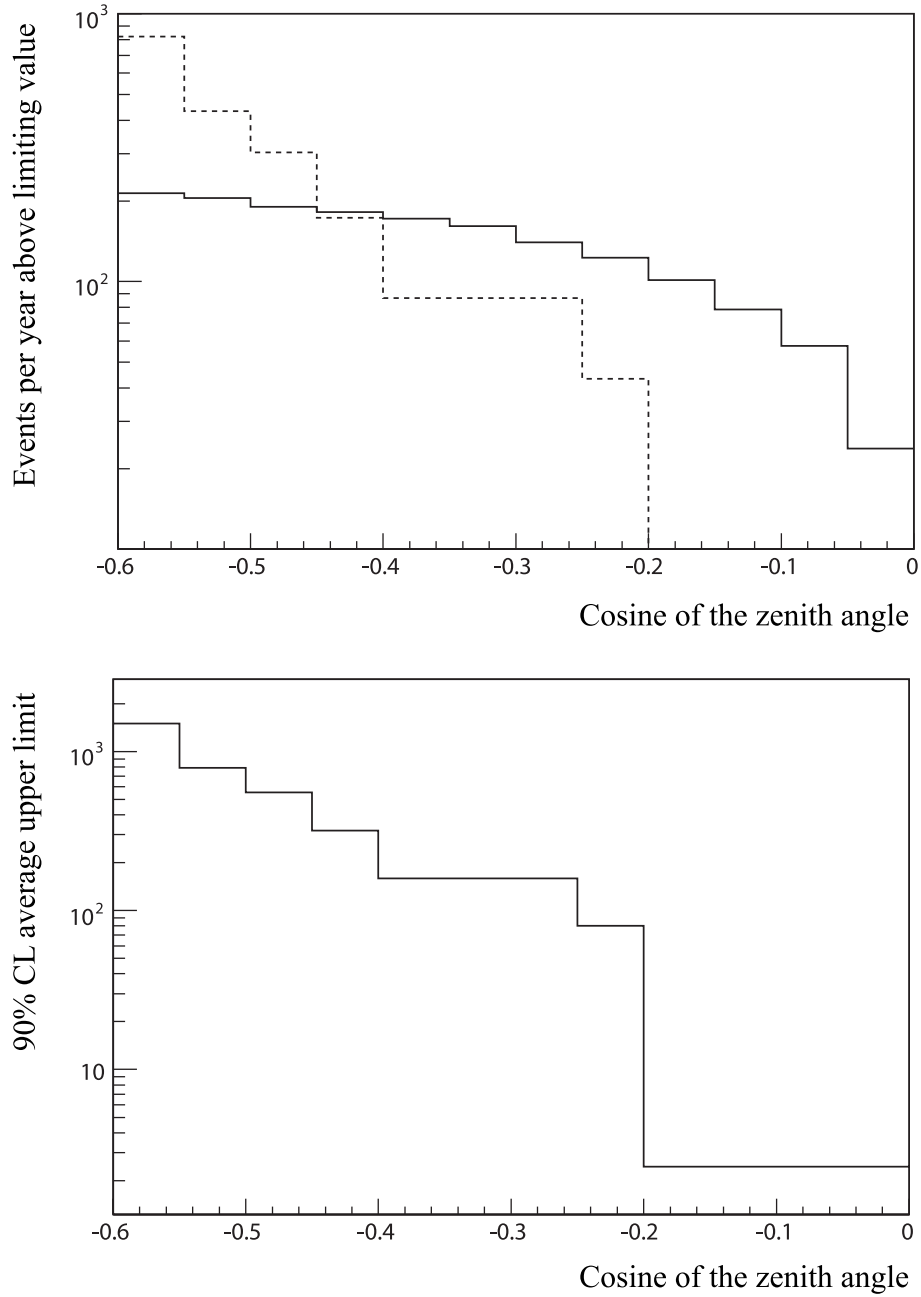


Figure 5.10: Integrated distribution of the cosine of the muon zenith angle for the flux shown in Figure 5.9. Signal (solid) events induced by the simulated AGN-like neutrino flux and atmospheric background (dashed) events are shown in the top figure. The average upper limit is shown in the bottom figure.

## High Energy Simulations Results

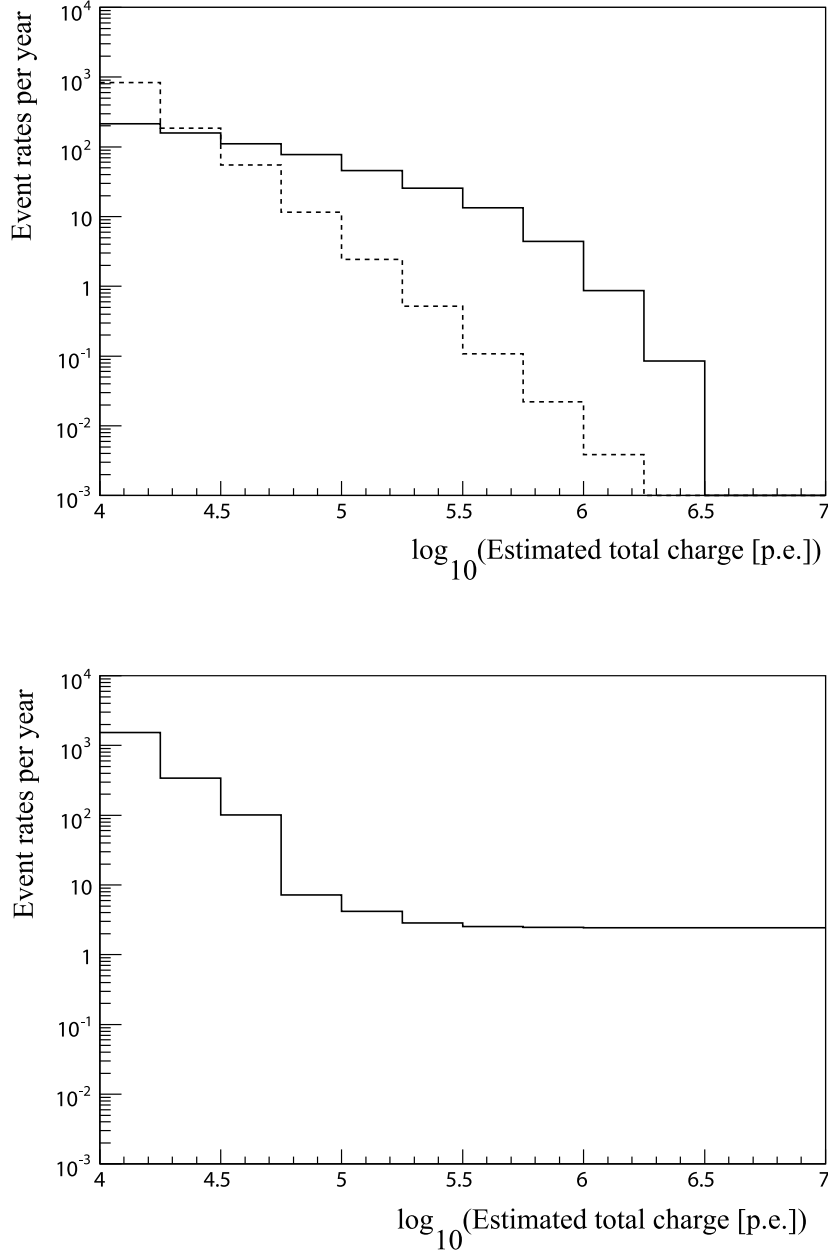


Figure 5.11: Integrated distribution of the estimated total charge of the hits for the flux shown in Figure 5.9. In order to place a more accurate constraint on the simulated neutrino flux, the atmospheric spectrum has been extrapolated to higher values assuming an  $E^{-2.7}$  spectrum. Signal (solid) events induced by the simulated AGN-like neutrino flux and atmospheric background (dashed) events are shown in the top figure. The average upper limit is shown in the bottom figure.

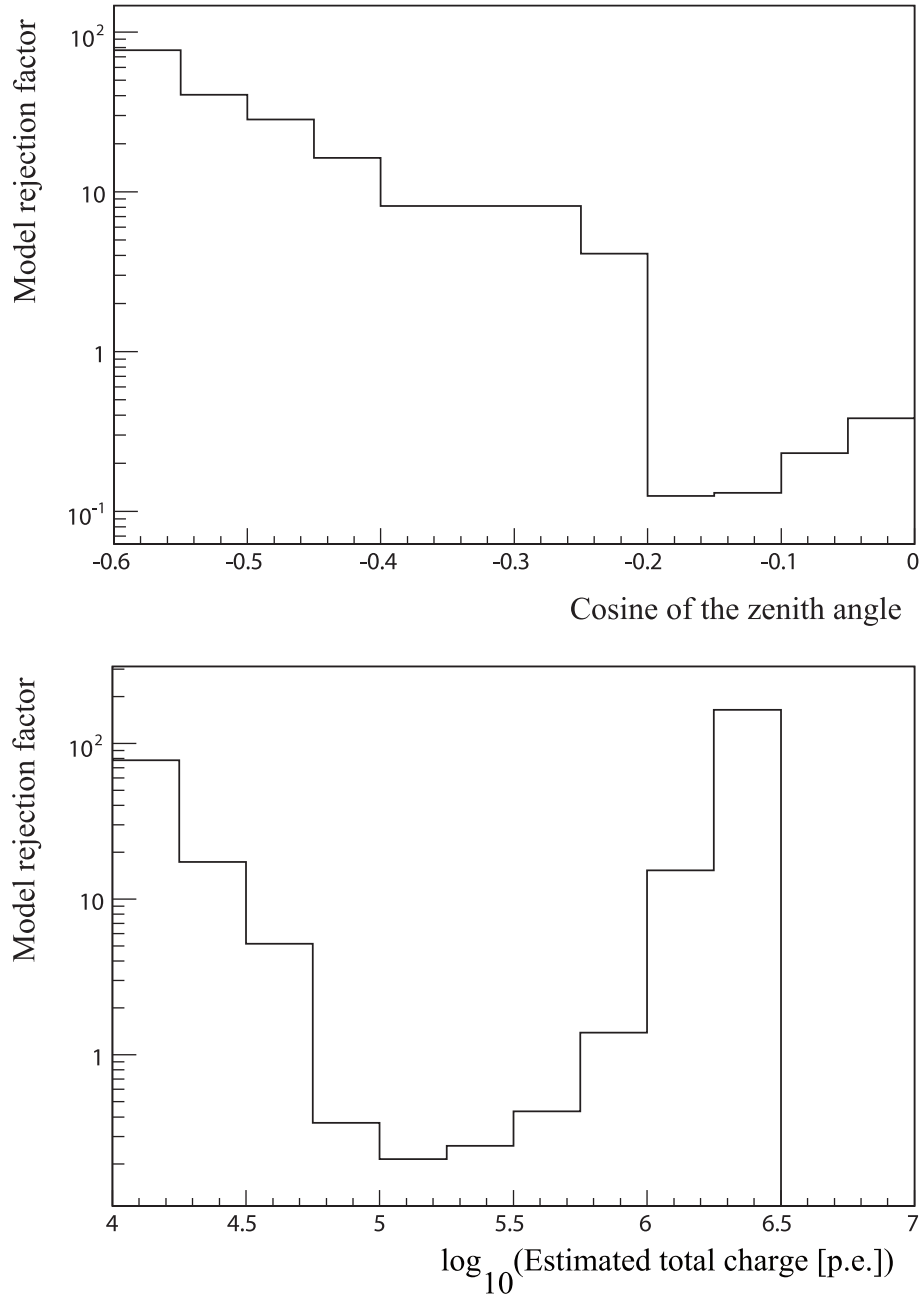


Figure 5.12: *Model rejection factor - as defined in the text - for the diffuse flux of downward-going UHE neutrinos as a function of the muon zenith angle (top) and total charge (bottom) cut variables.*

## High Energy Simulations Results

neutrino flux are therefore found by accepting events with  $\cos\theta \geq -0.2$  and a total charge of the hits  $N_{PE} \geq 10^5$  p.e.

The expected event rates, corresponding to the final event selection criteria defined above are shown in Figure 5.13 as a function of the cosine of the muon zenith angle direction and the total charge of the hits. A total number of  $N_s \approx 20$

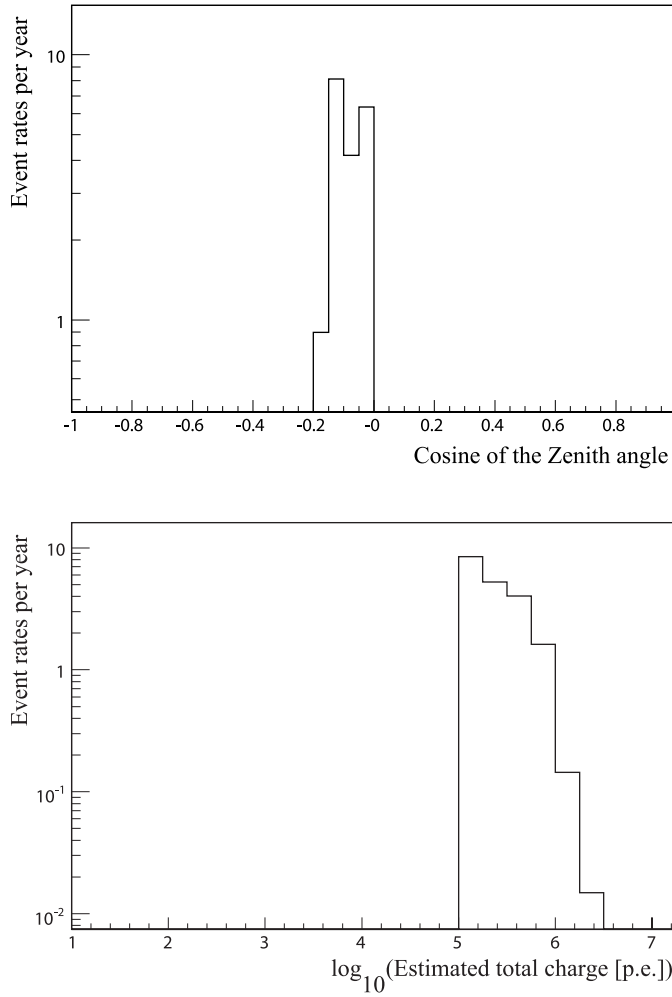


Figure 5.13: *Distributions of the cosine of the muon zenith angle (top) and the total charge (in p.e.) of the digitised signal (bottom) induced by downward-going ultra high energy (UHE) neutrinos, using optimised cut selections - as defined in the text. The astrophysical neutrino flux corresponds to an AGN-like spectrum.*

signal events remain and no background ( $N_b = 0$ ). This corresponds to an average upper limit of 2.44 events for one year and 0.81 events per year for three years of observation with the ANTARES telescope.

### 5.2.6 Average flux upper limits

The average flux upper limit or sensitivity of ANTARES to the diffuse flux of UHE muon neutrinos has been determined by scaling the assumed AGN-like neutrino flux by the ratio of the obtained average upper limit  $\bar{\mu}_{90}(N_b)$  to the expected signal  $N_s$ .

$$\phi(E_\nu)_{90\%} = \phi(E_\nu) \times \frac{\bar{\mu}_{90}(N_b)}{N_s}.$$

The predicted average flux upper limit, regardless of systematic uncertainties is therefore given by

$$E^2\phi \leq 1.2 \times 10^{-7} \text{GeVcm}^{-2}\text{s}^{-1}\text{sr}^{-1} \quad (\text{after 1 year}),$$

$$E^2\phi \leq 4 \times 10^{-8} \text{GeVcm}^{-2}\text{s}^{-1}\text{sr}^{-1} \quad (\text{after 3 years}).$$

It is valid for neutrino energies between  $10^5$  and  $10^{11}$  GeV. It applies to a pure flux of muon neutrinos.

Considering oscillations with a flavor composition at Earth such that  $\nu_\mu : \nu_{e^-} : \nu_\tau = 1 : 1 : 1$ , the equivalent average upper limit for an equally mixed neutrino flavors flux would be about three times the obtained value, that is

$$E^2\phi_{\nu_\mu + \nu_{e^-} + \nu_\tau} \leq 3.6 \times 10^{-7} \text{GeVcm}^{-2}\text{s}^{-1}\text{sr}^{-1} \quad (\text{after 1 year}),$$

$$E^2\phi_{\nu_\mu + \nu_{e^-} + \nu_\tau} \leq 1.2 \times 10^{-7} \text{GeVcm}^{-2}\text{s}^{-1}\text{sr}^{-1} \quad (\text{after 3 years}).$$

### 5.2.7 Comparison with existing bounds

Theoretical upper bounds have been placed on the diffuse flux of neutrinos, based on observations of gamma-rays and cosmic rays. The level of sensitivity obtained for the ANTARES telescope can be compared to the limit predicted by Waxman and Bahcall [107] for diffuse high energy muon neutrinos at

$$E^2\phi = 0.9 - 4.5 \times 10^{-8} \text{GeVcm}^{-2}\text{s}^{-1}\text{sr}^{-1}$$

for energies above  $10^4$  GeV. This bound was calculated with the assumption of a  $\nu_\mu : \nu_{e^-} : \nu_\tau = 1 : 2 : 1$  ratio. The corresponding 90% confidence level (CL) upper limit on an equally mixed flavor neutrino flux is thus given by

$$E^2\phi_{\nu_\mu + \nu_{e^-} + \nu_\tau} = 1.35 - 6.75 \times 10^{-8} \text{GeVcm}^{-2}\text{s}^{-1}\text{sr}^{-1}.$$

The Waxman and Bahcall limit constrains the neutrino flux using measurements of the cosmic ray spectrum above  $10^{19}$  eV. The model assumes that neutrinos are produced in interactions of protons with the ambient photons or matter, in sources which are optically thin for high energy protons to photo-meson and nucleon-meson interactions. The neutrino flux is taken to follow an  $E^{-2}$  dependence, as expected from Fermi acceleration. The Waxman and Bahcall limit is

## High Energy Simulations Results

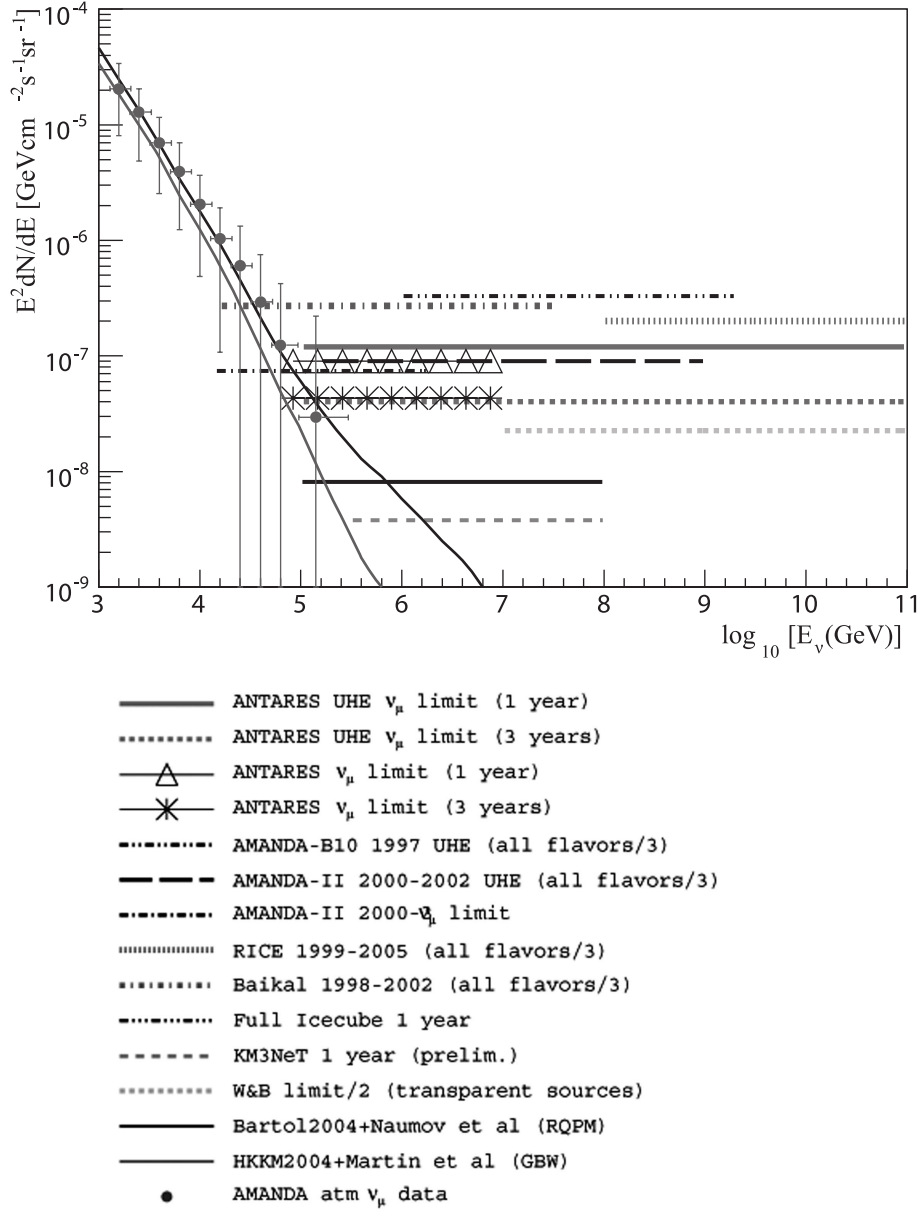


Figure 5.14: Comparison of the calculated upper flux limits for diffuse muon neutrinos as derived from different experiments and model calculations. The limits are given as a function of the logarithm of the neutrino energy. The measured atmospheric muon flux is shown using AMANDA-II data [108] with the central values for different calculations [109]. The Waxman and Bahcall bound is from [107], the ANTARES limit from [99], the AMANDA B10 limit at ultra high energy from [110]. The AMANDA-II limit is from [108] and for ultra energy from [111]. The RICE limit is from [112] and the BAIKAL limit from [113]. The IceCube limit is from [114] and the KM3NeT limit from [79]. The assumption has been made that  $\nu_\mu : \nu_{e^-} : \nu_\tau = 1 : 1 : 1$  at Earth.

interesting as it probes the sensitivity of the current and next generation of neutrino telescopes.

Upper limits have also been reported by several existing neutrino experiments, assuming the same benchmark  $E^{-2}$  dependence. In Figure 5.14, the 90% confidence level (CL) upper limits expected after one and three years of operation with ANTARES, for the diffuse flux of ultra high energy muon neutrinos are shown as a function of the neutrino energy. The most competitive experimental upper limits (at the 90% CL) for diffuse muon neutrinos are shown as well for comparison. The theoretical limit calculated by Waxman and Bahcall is also displayed. The sensitivity of ANTARES expected after one year of operation for diffuse UHE neutrinos is about a factor eight above the Waxman and Bahcall bound. After three years of data taking, the sensitivity is enhanced to about a factor two above the Waxman and Bahcall limit. As can be seen from the figure, the presented analysis predicts a sensitivity after one year of observation which is about a factor four above the upper limit placed by the AMANDA-II [111] telescope on the diffuse flux of UHE muon neutrinos. After three years of operation, the sensitivity of ANTARES improves to about a factor of two below that same upper limit. This upper limit has been determined by AMANDA-II using data from three years (2000 to 2002) with a livetime of 456.8 days. This is currently the most restrictive experimental bound placed by a neutrino telescope on a diffuse neutrino flux at UHE energies.

The upper limit calculated for ANTARES in this work is also about a factor two below the Radio Ice Cherenkov Experiment (RICE) bound [112] after one year of observation. After three years of data taking, the sensitivity of ANTARES increases to a factor of five below the RICE limit. This bound has been determined by RICE using data from seven years (1999 to 2005) with a livetime of 20500 hours that is around 854.1 days. This is currently the best limit at ultra high energies.

It should be noted that the present study is aimed at an order of magnitude estimate and does not account for systematic uncertainties. No full energy nor track geometry reconstruction was included. Nonetheless, a competitive upper limit has been found.

### 5.2.8 Effective detector area

The effective area for neutrinos represents the area of an ideal detector, capable of detecting neutrinos with full efficiency. It describes the performance of a telescope including its efficiency to observe neutrinos. The effective area  $A_{eff}$  is defined as

$$N_{events} = T \int dE_\nu d\theta_\nu \Phi A_{eff}(E_\nu, \theta_\nu)$$

where  $N_{events}$  is the number of events,  $T$  the detector live-time and  $\Phi$  the incoming neutrino flux. The effective area depends on the energy  $E_\nu$  and the zenith

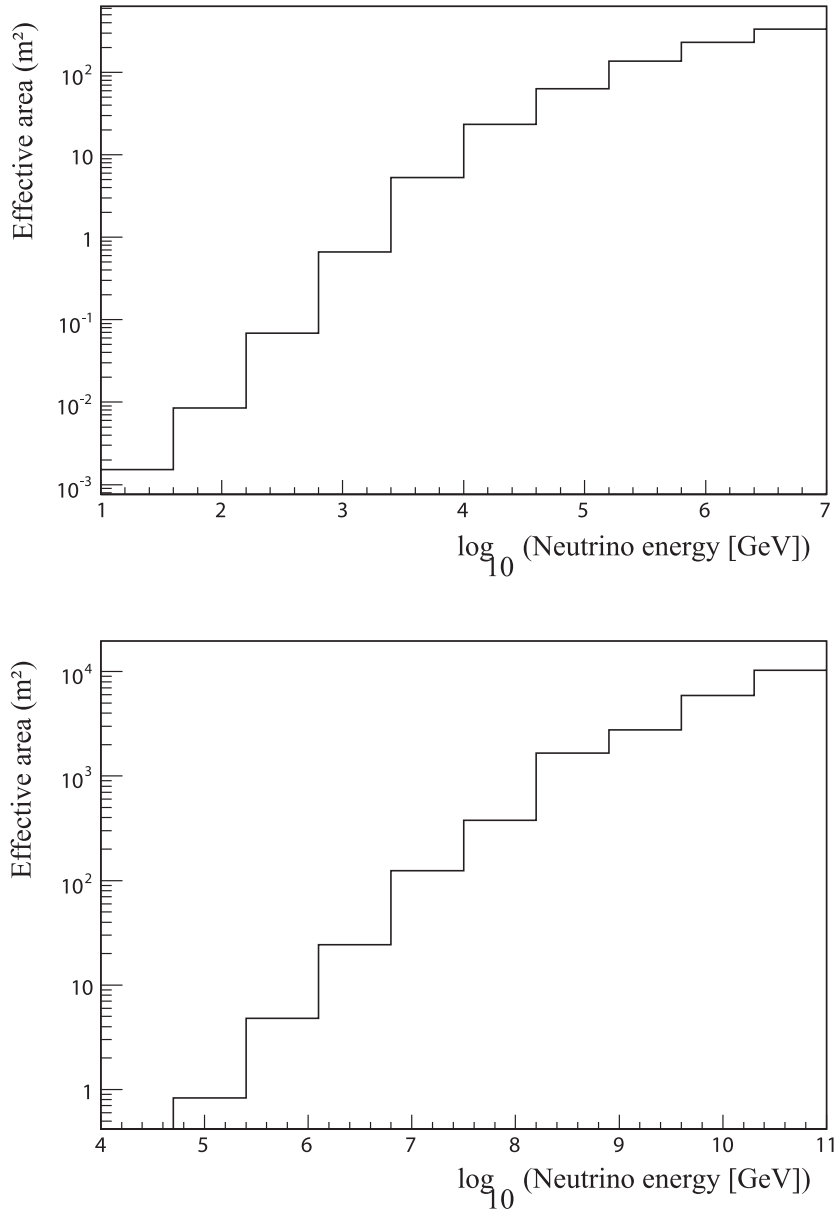


Figure 5.15: Muon neutrino effective area (in square meters) for ANTARES as a function of the neutrino energy (in GeV). The effective area for events which survive the selection cuts for UHE neutrino detection as described in Section 5.3.5 is shown (bottom). The standard effective area for (upward-going) neutrino energies below  $10^7$  GeV is also shown for comparison (top).



angle  $\theta_\nu$  of the neutrinos. In Figure 5.15, the effective area of the ANTARES telescope is shown as a function of the (true) incoming neutrino energy, for those events which could survive the optimised selection cuts described in the previous subsections. The optimised selection criteria lower the effective area at energies below  $10^7$  GeV, as compared with the standard effective area of the ANTARES telescope. However, the effective area is enhanced at higher energies. As can be seen in the figure, the detection area increases with the neutrino energy up to  $10^4$  m<sup>2</sup> at  $10^{11}$  GeV. In the nearly horizontal angular range, a large area is covered by the muon tracks what yields an high detection efficiency. Moreover, high energy events produce a large amount of light which induce hits in the telescope, even when the neutrino interaction occurs far from the telescope.

### 5.3 Discussion

In the presented study, the flux of ultra high energy (UHE) diffuse muon neutrinos from downward-going and horizontal events has been simulated. Using new dedicated software packages and an optimised set of selection criteria, a fairly competitive upper limit for the neutrino event rate has been found. The event rates, however, remain low when using the neutrino telescope ANTARES. It is anticipated that the cubic kilometer sized KM3NeT [79] telescope will lead to an event rate increase with a factor twenty or more, and hence a reduction in the upper limit that probes the Waxman and Bahcall range (cf. Figure 5.14).

## *High Energy Simulations Results*

# Summary and conclusions

Extremely energetic cosmic particles, with energies as high as  $10^{20}$  eV have been observed in extensive air shower arrays [11] [12] [7]. The origin of these ultra high energy cosmic rays is one of the intriguing puzzles of astroparticle physics. In order to solve this problem, the astrophysical objects which are the source of cosmic rays and the processes involved in the production of particles with such extreme energies need to be unraveled.

In the last several years, considerable advances have been achieved in the field of cosmic ray research. Even though uncertainties remain and alternative models can be envisaged [12], evidence may be emerging for a diffuse shock acceleration scenario, involving extragalactic sources [11] [7]. Further information on the origin of ultra high energy cosmic rays can be obtained by searching for ultra high energy neutrinos. Ultra high energy neutrinos originate from the interactions of cosmic rays with ambient photons at the sites where they are produced [2]. Since neutrinos are stable neutral particles which interact very weakly with matter, they can travel across extragalactic distances to reach the Earth without being deflected by the electromagnetic fields of the Universe. Neutrinos thus point back to their sources and may provide essential information on the inner workings of ultra high energy cosmic ray accelerators.

The small interaction probability of neutrinos make them difficult to detect. Neutrino telescopes overcome this issue by observing the products of their interactions through the Cherenkov effect in a transparent medium such as sea water or ice. The main topic of this thesis is to study whether neutrino detectors can be used to search for ultra high energy neutrinos.

A correlation between ultra high energy cosmic rays and the several nearby active galactic nuclei (AGN) has recently been reported [13] which suggests that AGN are likely sources of ultra high energy neutrinos as well. The sensitivity of the ANTARES neutrino telescope to ultra high energy neutrino events above  $10^{16}$  eV (and up to  $10^{20}$  eV) has been estimated in the framework of this thesis. At these ultra high energies, the Earth is opaque to neutrinos and only downward-going and horizontal neutrinos can arrive at the detector. Since neutrino telescopes such as ANTARES are optimized for the detection of upward-going neutrinos in the energy range from  $10^{11}$  to  $10^{16}$  eV, it needs to be investigated whether downward-going neutrinos of energies in excess of  $10^{16}$  eV can be observed. This

## High Energy Simulations Results

is of relevance not only for the ANTARES telescope but also for the future cubic kilometer-scale detector KM3NeT. Moreover, the present study will provide information for the optimisation of the geometry of the KM3NeT telescope and the technologies required.

A non-localised flux of high energy neutrinos has been considered in order to enhance the probability of detection. As muon neutrinos are more easy to detect, only this neutrino flavor has been taken into account in the data analysis. The diffuse flux of muon neutrinos from AGN has been modelled by a generic  $E^{-2}$  spectrum with units of  $10^{-6}\text{GeV}^{-1}\text{cm}^{-2}\text{s}^{-1}\text{sr}^{-1}$  [2].

The performance of ANTARES relies on the timing resolution of the signals recorded in the photo-sensors of the telescope and the proper operation of the various mechanical and electronic components of the telescope. A time calibration method and a diagnostic tool to determine if components are functioning as expected have been developed. The time calibration method has been tested with the MILOM prototype instrumentation line of ANTARES to provide preliminary information on the time calibration of the entire telescope. The method consists of the determination of the time offsets between the responses of the front-end chips of the line to a flash of an optical beacon. All electronics and calibration systems were found to contribute less than 0.5 ns to the overall timing resolution. This result enables us to predict an angular resolution of less than  $0.3^\circ$  for the ANTARES telescope.

The sensitivity of ANTARES to ultra high energy neutrinos has been evaluated in terms of Monte Carlo simulations. Three distinct stages of simulation can be recognised: the neutrino event generation, the propagation of the produced leptons towards the telescope and the detector response simulation. The simulation programs used to simulate events in ANTARES accept neutrino events within a limited range of energies only, i.e. below  $10^{16}$  eV and thus cannot be exploited for the study of ultra high energy neutrino events. Improvements of already existing packages and the development of new programs have thus been required.

The neutrino event generator ANIS [74] was initially designed for use with the AMANDA neutrino telescope but it has been adapted to ANTARES to generate ultra high energy neutrino interactions in the surrounding water and seabed. The produced secondary leptons have been propagated towards and through ANTARES using the lepton propagator MMC [50] which is interfaced with ANIS and can process ultra high energy events. The telescope geometry and the sea water properties at the ANTARES site have been implemented in MMC. The output format of ANIS and MMC has been modified such that the software packages could be integrated into the ANTARES Monte Carlo simulation chain. This enabled a comparison with GENHEN [55], a neutrino event generator that includes lepton propagation. When suitably tuned, both programs were found to require roughly the same amount of CPU time and give comparable event rates. Nevertheless, only ANIS can be used in association with MMC above  $10^{16}$  eV to

generate ultra high energy neutrino events in the telescope.

A fast and flexible detector simulation program for neutrino telescopes has been developed to simulate the hits from Cherenkov photons at ultra high energies. The software package, named SIRENE was primarily designed for the future cubic kilometer-sized detector KM3NeT [79], but it has been applied to ANTARES as the program allows the use of alternative geometries belonging to other neutrino telescopes. SIRENE is capable to model the detector response for neutrino events with energies as high as  $10^{20}$  eV. The program does not only allow the simulation of variable telescope geometries but also of different configurations and characteristics of the photo-multiplier tubes inside the optical modules of the telescope. SIRENE has been integrated into the ANTARES Monte Carlo simulation chain, thus enabling a comparison with the detector simulation package KM3 which is commonly used for ANTARES simulations. The ANTARES event library has been modified to take the characteristics of SIRENE into account.

Both programs were found to give comparable results in the energy range below  $10^{16}$  eV, although differences remain that can be attributed to the tracking algorithms employed and the parametrisation of the muon total cross section. Moreover, in contrast to KM3, SIRENE can be used to process ultra high energy neutrino events. An interface with the trigger software of ANTARES has been developed to simulate the effect of the detector electronics and trigger the events produced by SIRENE. In order to validate the quality of the events simulated by SIRENE, they have been subjected (after digitization) to two distinct track reconstruction programs, known as Aart Strategy and Scanfit, which are available in the ANTARES collaboration. It was found that SIRENE cannot easily be used with either reconstruction algorithm. This can be partly attributed to the probability density functions adopted by both reconstruction programs that correspond to muon energies less than  $10^{14}$  eV. These probability functions are therefore not suitable for simulating ultra high energy neutrino events with SIRENE. Moreover, the reconstruction programs were primarily designed for use with KM3 which involves a specific tracking algorithm that is not especially adequate for SIRENE. Therefore, new probability density functions for describing the ultra high energy range need to be developed and further tuning is required to improve the performance of the reconstruction programs in conjunction with SIRENE. However, the program that is used for energy reconstruction was found to perform well with SIRENE in the energy range below  $10^{16}$  eV. None of the available reconstruction algorithms was found suitable at ultra high energies and a different approach has been envisaged to estimate the ANTARES sensitivity in this domain.

When searching for neutrinos in the ultra high energy domain, the background consists of atmospheric muons which can reach the detector. They result from interactions of cosmic ray primaries in the Earth's atmosphere and can be mis-interpreted as secondary leptons from cosmic neutrinos. The program MU-

## High Energy Simulations Results

PAGE [100] has been used to simulate the atmospheric muons impinging on the ANTARES detector surface. MUPAGE is a parametrisation of the atmospheric muon flux, based on HEMAS [101], simulating single and multiple underwater muons at the depth of the detector. A dedicated data analysis method has been developed in order to reduce the atmospheric muon background while preserving sensitivity to the ultra high energy signal. The method relies on differences between the signal and the atmospheric muon background regarding the energy of the muons and the direction from which they arrive at the detector. The amount of light emitted by the muons and the associated electromagnetic showers provide an indirect measure of the muon energy. As it depends on the position of the track relative to the telescope, it contains position and direction information and can be used to estimate the muon energy without having to rely on a full geometrical reconstruction. To include the simulation of the front-ends electronics, the total charge of the hits has been chosen as an estimate of the muon energy for the data analysis. It was found that the atmospheric background can be rejected by excluding events with low charge values and vertical directions. A model rejection potential method has been applied to optimise the experimental cuts and place the strongest constraints on the simulated AGN-like diffuse neutrino flux. The optimised selection criteria lower the effective area for neutrinos at energies below  $10^{16}$  eV as compared with the standard effective area of the ANTARES telescope. However, the effective area is enhanced at higher energies up to  $10^4 \text{ m}^2$  at  $10^{20}$  eV. The obtained effective area is comparable to the one of the neutrino telescope AMANDA-II for the same flux model and energy range [111].

An estimate of the average flux upper limit that can be obtained with ANTARES for the simulated AGN-like diffuse muon neutrino flux has been placed at the 90% confidence level at

$$E^2\phi \leq 1.2 \times 10^{-7} \text{GeVcm}^{-2}\text{s}^{-1}\text{sr}^{-1} \quad (\text{after 1 year}), \quad (5.2a)$$

$$E^2\phi_{\nu_\mu+\nu_{e^-}+\nu_\tau} \leq 4.1 \times 10^{-8} \text{GeVcm}^{-2}\text{s}^{-1}\text{sr}^{-1} \quad (\text{after 3 years}). \quad (5.2b)$$

This limit is valid for neutrino energies between  $10^{17}$  eV and  $10^{20}$  eV. It was compared with the currently most competitive upper bounds made on the diffuse flux of ultra high energy neutrinos. The upper limit predicted after one year of observation with ANTARES is about on order of magnitude above the theoretical bound calculated by Waxman and Bahcall [107] and about a factor of four above the upper limit placed by the AMANDA-II [111] telescope. The expected sensitivity after three years of operation is enhanced to about a factor of two above the Waxman and Bahcall limit. Compared with the results reported by AMANDA-II, the sensitivity of ANTARES expected after three years of data taking shows an improvement of almost a factor two. These results are encouraging. However, it should be noted that the present study is aimed at an order of magnitude estimate. No full energy nor track geometry reconstruction was included. Nonetheless, a fairly competitive upper limit for the neutrino event rate has been found.

### *5.3 Discussion*

It is anticipated that the cubic kilometer sized KM3NeT [79] project will lead to an event rate increase of about a factor twenty, and hence a substantial reduction in the upper limit allowing to probe the Waxman and Bahcall range.

## *High Energy Simulations Results*



# Appendix A

## Implementation of ANTARES in ANIS

On input the program ANIS uses a steering file which contains all run specific information. Below is an example of such a file for the ANTARES telescope which is situated at depth  $D = 2196.849$  meters. In this example  $N = 10000$  upward-going muon neutrinos and anti-neutrinos (50% each) are generated between 10 GeV and  $10^{12}$  GeV assuming an energy spectrum  $F(E) = E^{-1} \text{GeV}^{-1} \text{cm}^{-2} \text{sr}^{-1} \text{s}^{-1}$ . cross sections are evaluated in the framework of pQCD using the CTEQ5 parton distribution functions (PDFs). The chosen size of the neutrino interaction volume (Final Volume) has been set equal to a cylinder with a radius of  $R = 600$  meters, an upper (detector region) and a lower (target region) heights both equal to  $\text{HAheight} = \text{HBheight} = 600$  meters. This Final Volume encompasses the ANTARES Can ( $R = 266.11$  meters,  $\text{HAheight} = 278.15$  meters and  $\text{HBheight} = 341.47$  meters) for every events in the energy range of interest. It therefore allows to generate all the events which can produce detectable secondaries in the ANTARES telescope, without missing any. To optimize the geometry of the Final Volume, its size is adjusted for each event to the maximum muon range at the considered energy. A detailed description of the various parameters can be found in [74].

```
#####  
# Steering file for running ANIS with the ANTARES telescope      #  
#####  
#  
# The flux information:  
f p 1. 10 1e12 -1. 0. 14  
#  
# The geometry information  
g c 600 600 600 2196.849 1  
# The run information  
r 10000 2 1 1234  
#
```

## *Implementation of ANTARES in ANIS*

```
# the data directory
d /anis.v1.8.2/data
#
# The cross section processes and data.
# Do not change unless you know what you are doing.
s CC cteq5/cteq5_cc_nu.data cteq5/final_cteq5_cc_nu.data 101010 110
s CC cteq5/cteq5_cc_nubar.data cteq5/final_cteq5_cc_nubar.data 10101 110
s NC cteq5/cteq5_nc_nu.data cteq5/final_cteq5_nc_nu.data 101010 110
s NC cteq5/cteq5_nc_nubar.data cteq5/final_cteq5_nc_nubar.data 10101 110
s GR dummy dummy 10000 1
```

The generated events can be re-weighted to any relevant power-law spectrum such as diffuse AGN-like or other ultra-high-energy (UHE) neutrino (and anti-neutrino) flux predictions.

The second value that follows the “r” run parameter in the steering file stands for the output format to be used by ANIS. The AMANDA/IceCube f2000 ASCII format is used for ANTARES as the lepton propagator MMC which is interfaced with ANIS is using this specific format.

## Appendix B

# Implementation of ANTARES in MMC

The various media implemented in MMC are assumed to be concentric spheres centered at the center of the Earth, each having different densities. These spheres are surrounded by a main medium which fills all space. The Earth's radius is assumed to be  $R_T = 6.3713 \times 10^6$  meters, the bedrock lies at  $b_0 = -2475$  meters below sea level at the ANTARES site. No additional bed elevation ( $z_0 = 0$ ) of the rock is assumed. The center (of gravity) of the ANTARES telescope is at a depth  $D = 2.196849 \times 10^3$  meters. The sea water above the detector center has a smaller density ( $1.0291g.cm^{-3}$ ) than the water below ( $1.0404g.cm^{-3}$ ). For ANTARES, three spheres define the Earth which is enclosed inside air. The first sphere with the radius of the Earth defines the sphere for the sea water at the ANTARES site above the telescope center. This sphere extends down to  $z = 2.196849 \times 10^3$  meters. The second sphere contains for the sea water at the ANTARES site below the detector center. Its radius is  $6.3713 \times 10^6 - 2.196849 \times 10^3 = 6.369103151 \times 10^6$  meters. The sphere passes through the center of the telescope which defines the origin of the altitudes  $z = 0$  in the MMC geometry. The third and last sphere is the seabed rock below the detector and consist of standard rock. The radius of the sphere is  $6.3713 \times 10^6 - 2475 = 6.368825 \times 10^6$  meters. The sphere goes through  $z = -278.151$  meters. MMC uses a media definition file in which the rock and sea water surrounding ANTARES are detailed. Such a file can be defined as follows:

```
# media definition file
# include with -mediadef=[this file]
# use the following syntax:
# all          det vcut ecut conti rho medium
# sphere z r det vcut ecut conti rho medium
all           0 0.05 5.e2 1 1.0          Air
sphere 2196.840 6371300 0 0.05 5.e2 1 0.99456 Antares Water
sphere 0 6369103.151 1 0.05 5.e2 1 1.0    Antares Water
```

## Implementation of ANTARES in MMC

sphere -278.151 6368825 0 0.05 5.e2 1 1.0 Standard Rock

A new medium (Antares water) was implemented in MMC with the properties of the Mediterranean sea water at the ANTARES site. In Figure B.1, the distribution of the final energy of the muons that crossed 300 meters of Antares water with a fixed initial energy equal to 100 TeV is shown. Several values of  $\nu_{cut}$  were used to determine which relative energy cutoff would give the most accurate results. For higher  $\nu_{cut}$ , the muon spectra are not continuous, but present a peak at the energy  $E_{peak}$  which is separated from the distribution by at least the value of  $\nu_{cut} \times E_{peak}$ . This is a known behaviour of MMC. In order to be able to use MMC with high  $\nu_{cut}$ , a continuous randomisation feature was introduced. The results when applied to the ANTARES water are shown on Figure B.2. As can be seen on the figure, the distributions have become continuous, but converge faster than those without the continuous randomisation option. In order to bring the number of separate energy loss events to a reasonable value and therefore to increase the running speed, when using MMC with ANTARES we will use a rather high value of the relative energy cutoff ( $\nu_{cut} = 0.05$ ) with the continuous randomisation feature.

The salinity of the water has been measured to be  $38.44 \pm 0.02 \text{ g.kg}^{-1}$  at the ANTARES site whereas it was cited as  $35.0 \text{ g.kg}^{-1}$  in [115] for sea water in general. Therefore the chemical composition of the water at the ANTARES site is the same as the water defined in [115] but with different densities for the elements containing salt. The chemical composition of the sea water at the telescope site is defined in [82]. The values of the density of the main water elements are shown in Table B.1.

Atomic Symbol	Atomic Number (Z)	Atomic Weight (A)	Percent by weight
H	1	1.0	2.0
O	8	15.999	1.00884
$N_a$	11	22.99	$9.43.10^{-3}$
K	19	39.10	$2.09.10^{-4}$
$M_g$	12	24.31	$10.87.10^{-4}$
$C_a$	20	40.08	$2.09.10^{-4}$
$C_l$	17	35.45	$1.106.10^{-2}$
S	16	32.07	$5.82.10^{-3}$

Table B.1: Chemical composition of the sea water at the ANTARES site.

MMC reads and outputs data in the AMANDA ASCII F2000 compliant format to and from the standard input and output so the events can be passed to the detector simulation. The F2k output format can be translated into the ANTARES event ASCII format to process the output of MMC with the ANTARES detector simulation and analyse the Monte Carlo data with the help of the main trigger

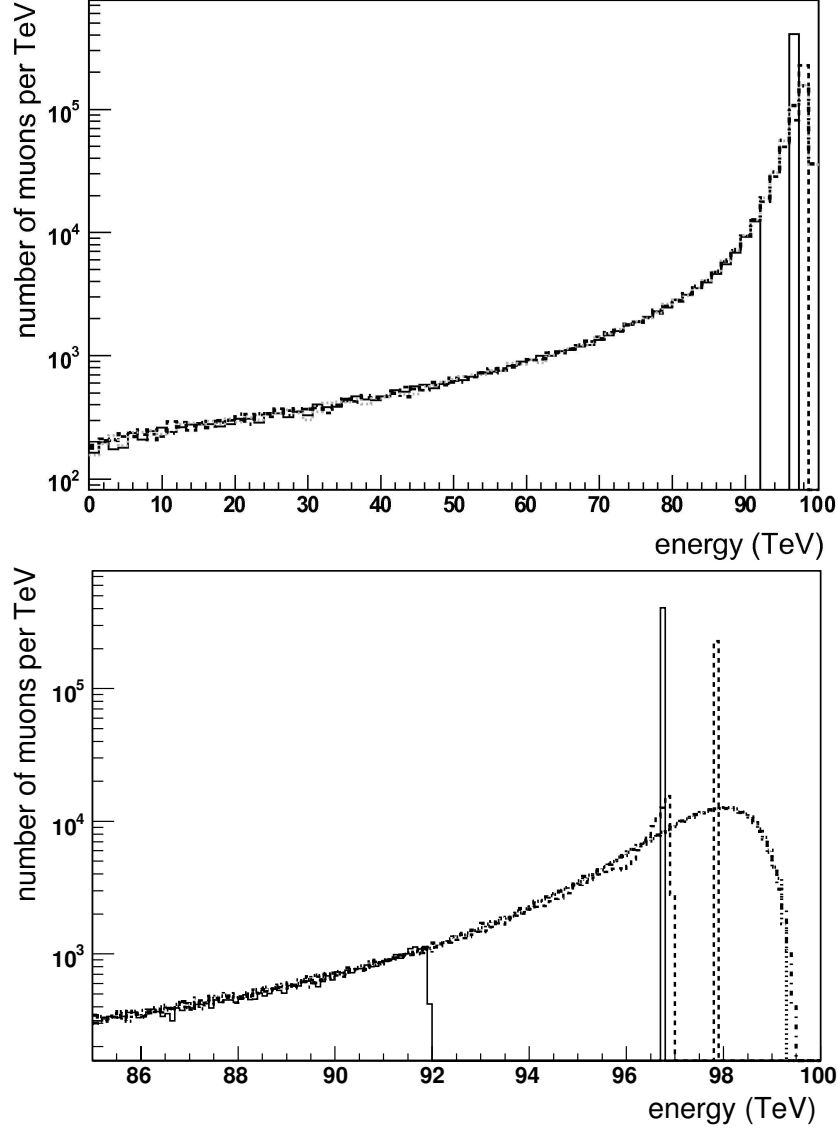


Figure B.1: Comparison of the final energy distributions of  $10^7$  muons with initial energy 100 TeV which were propagated through 300 meters of ANTARES Water, calculated by MMC with an energy cutoff  $v_{\text{cut}} = 0.05$  (solid line),  $v_{\text{cut}} = 0.01$  (dashed),  $v_{\text{cut}} = 10^{-3}$  (dotted) and  $v_{\text{cut}} = 10^{-4}$  (dashed-dotted). On the right is a close-up on the left figure.

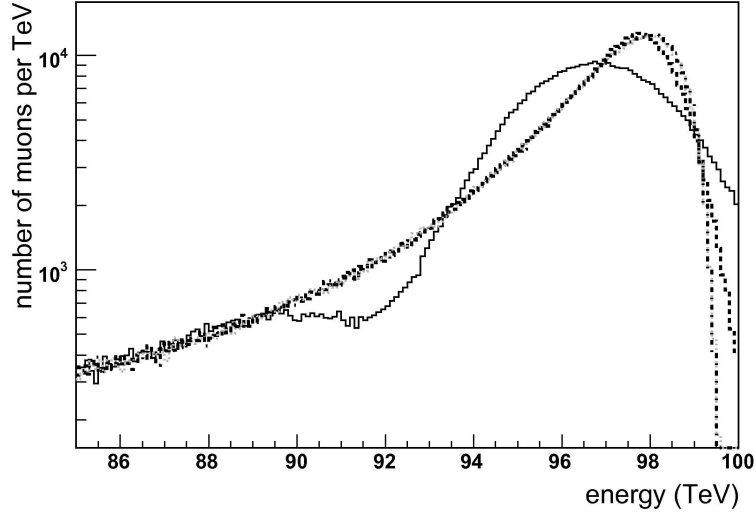


Figure B.2: Same as the right part of Figure B.1 but with the continuous randomisation option which is used to prevent muon spectra to be not continuous for high  $\nu_{cut}$ .

software (see Chapter 3). The ANTARES event ASCII format makes use of tags defined to make the Input/Output (IO) of the Monte Carlo data compatible with the ROOT framework which allows to analyse the data in a more efficient way. A detailed description of the ANTARES event tags which exist for Monte Carlo simulated data can be found in the internal note [65].

# Appendix C

## SIRENE software implementation

SIRENE runs on a UNIX platform and consists of a library of C++ classes <sup>1</sup> that enables the implementation of different sources of Cherenkov photons, different scattering models for the transparent medium surrounding the telescope, and various detector geometries. The program assumes that a neutrino telescope is a collection of modules housing one or more photo-multiplier tubes (PMTs), which allows any neutrino detector geometry, and any configuration of the photo-multiplier tubes inside these modules. Sometimes, for example in the case of ANTARES, these modules are referred to as optical modules (see Chapter 2).

Figure C.1 shows a schematic overview of the detector simulation program SIRENE. The most important C++ classes which compose the program, are shown as well as their hierarchy. These classes are described one by one in the next subsection.

### C.0.1 Classes to build the geometry of a telescope

The geometry of a Cherenkov neutrino telescope is determined by the number of modules housing photo-multiplier tubes, as well as their positions and their characteristics. The type of photo-multiplier tubes, their position and direction within the modules of the telescope and their characteristics have also to be specified. An interface has been developed such that SIRENE may use files produced with GENDET [117] to describe the geometry of the ANTARES telescope. With this convention the reference system is such that the x-axis is directed towards the North, the y-axis towards the West and the z-axis is pointing upward. The origin of the coordinate system is located at the center of gravity of the telescope. To enable the (software) reconstruction of a neutrino telescope, the following classes are implemented.

---

<sup>1</sup>The C++ programming language allows to define program-specific datatypes through the use of classes. Examples of these data types are known as objects and can contain member variables, constants, member functions, and overloaded operators defined by the programmer [116].

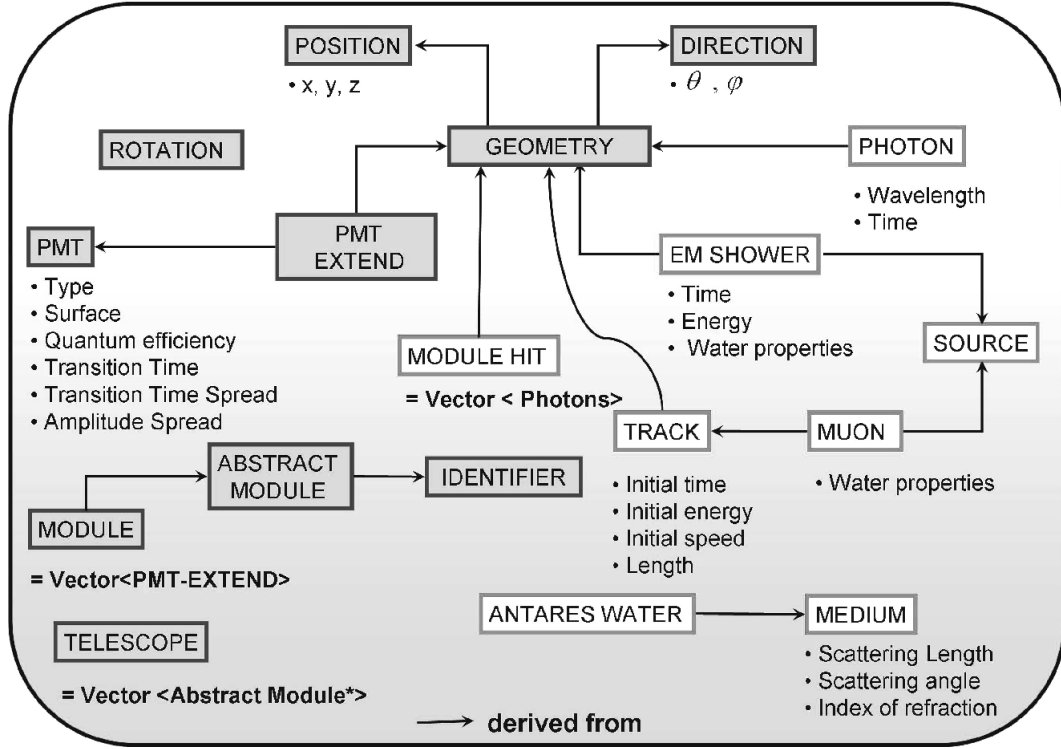


Figure C.1: Schematic overview of the classes of the detector simulation program SIRENE. All currently implemented classes are shown. Dark grey boxes represent classes used for the geometry of the telescope. Light grey boxes represent classes used to represent the tracking of the secondary particles and the produced Cherenkov photons.

**PMT** The class PMT defines a photo-multiplier tube with its main characteristics such as its effective area, time transit (TT), time transit spread (TTS), amplitude spread and the quantum efficiency of its cathode. These parameters can be read from external cards so the program does not need to be recompiled if a different type of PMT has to be used. The default values correspond to the ANTARES PMT purchased from Hamamatsu [91].

**PMT EXTEND** The class PMT EXTEND provides the orientation and position of a photo-multiplier tube inside the module. It is derived from the classes PMT and GEOMETRY.

**ABSTRACT MODULE** The class ABSTRACT MODULE defines a virtual sphere with a given radius. This class is used to track the Cherenkov photons towards the modules of the telescope and constitutes a pure artificial object of the simulation which does not represent a physical object. The radius of the virtual sphere can be chosen such that it envelops one or more modules of the telescope. The surface of the cross section through the center of the virtual sphere is oriented



perpendicular to the direction of the arriving Cherenkov photons. The orientation depends on the position and direction of each source of Cherenkov photons. Once the photons have been tracked towards the modules of the telescope, their position, direction, and arrival time are recorded on this optimally oriented surface. This gives each ABSTRACT MODULE a list of recorded photons inside the volume and on the surface delimited by the virtual sphere (see the definition of the class MODULE HIT). The class ABSTRACT MODULE derives its data from the classes GEOMETRY and IDENTIFIER.

**MODULE** The class MODULE defines a module of the telescope. It consists of a container housing a set of one or more photo-multiplier tubes. The class MODULE is derived from the class ABSTRACT MODULE. The characteristics of the glass and the gel are implemented with their thickness but also their absorption length as a function of the wavelength.

**TELESCOPE** The class TELESCOPE defines a neutrino telescope which consists of positioned virtual spheres called ABSTRACT MODULEs.

**IDENTIFIER** The class IDENTIFIER gives a unique identifier to every module of the telescope.

**POSITION** The class POSITION is an utility class used to define a cartesian vector position in three dimensions.

**DIRECTION** The class DIRECTION is an utility class to define a three dimensional orientation with spherical polar coordinates.

**GEOMETRY** The class GEOMETRY defines the position and the orientation of each object in the telescope. It is derived from the classes POSITION and DIRECTION.

**ROTATION** The class ROTATION is an utility class to define a three dimensional rotation with spherical polar coordinates.

## C.0.2 Classes for the tracking of the particles

An interface has been developed within the ANTARES Monte Carlo generators, producing ASCII format output of SIRENE, such that the program can use input files created with GENHEN or ANIS (and MMC). The program MonteCarloEvent can then be used to translate the output of SIRENE written in the ANTARES ASCII

## *SIRENE software implementation*

event format into the ANTARES ROOT event format for a more efficient storage and processing of the data with the trigger (TriggerEfficiency) and Reconstruction (Aart Strategy, ScanFit) codes. The entire ANTARES library for simulation codes (ANTCC) was changed in order to take the photon weights calculated by SIRENE into account. For the tracking of the secondary particles created at the neutrino interaction vertices and the Cherenkov photons they generate, the following classes are constructed.

**PHOTON** The class PHOTON defines the light emitted by a Cherenkov radiation source. The class PHOTON is derived from the class GEOMETRY.

**SOURCE** The class SOURCE represents the type of Cherenkov light source. Currently, muons and electromagnetic showers are implemented as possible sources, but SIRENE is designed such that new sources can be easily added.

**EMSHOWER** The class EMSHOWER defines a Bremsstrahlung initiated electromagnetic shower. All its energy is deposited over a short distance and it is considered point-like. The class EMSHOWER is derived from the classes GEOMETRY and SOURCE.

**TRACK** The class TRACK is a particle track with a starting time and energy. The class TRACK is derived from the class GEOMETRY.

**MUON** The class MUON defines a muon. A muon is characterised by a straight track losing energy and emitting Cherenkov light. Stochastic losses which produce independent electromagnetic showers are implemented. The class MUON is derived from the classes TRACK and SOURCE.

**MODULE HIT** The class MODULE HIT corresponds to an ABSTRACT MODULE with the list of all the photons that hit the corresponding virtual sphere. The class MODULE HIT is derived from the class GEOMETRY.

### **C.0.3 Classes to model the scattering of the particles**

For the scattering of the Cherenkov photons inside the medium surrounding the instrumented volume of the neutrino telescope, the following classes are implemented.

**MEDIUM** The class MEDIUM defines the properties of the detection medium to include the effect of the medium on light propagation.

**ANTARES WATER** The class ANTARES WATER represents the scattering model and water properties at the ANTARES telescope site. The class ANTARES WATER is derived from the class MEDIUM.

*SIRENE software implementation*

# Acknowledgements

These years in Amsterdam have been a very unique experience both from a professional and a personal points of view. I am very grateful I was given the chance to carry out my doctorate in the ANTARES group at Nikhef. It has really been a pleasure to work in such a good and inspiring environment.

I would like first to thank my promotor Gerard van der Steenhoven and my co-promotor Els de Wolf for their precious advices and guidance during my PhD. You have pushed me to achieve more than I would have never done otherwise. I might repeat myself ( $\times 2$ ) but thank you for your help and support.

I also wish to thank our team leader, Maarten de Jong. Thank you for your time whenever I dropped by your office. I learnt a lot by working with you, especially on the time calibration and the monitoring of ANTARES and my C++ programming skills have dramatically improved.

Thank you very much to Paul Kooijman for helping me develop the software program SIRENE and for being there whenever I had a question on the related physics topics and my study of ultra high energy neutrinos.

I would like to give special thanks to Marek Kowalski and Dmitry Chirkin for allowing me to use the software programs ANIS and MMC. Thank you also to Teresa Montaruli for helping me to learn the GENHEN software program. Your many emails have guided me during my work on ultra high energy neutrino generators and lepton propagators.

I also had the opportunity to visit the ANTARES group at CPPM in Marseille for several months and I would like to thank everyone there for their warm welcome. Thank you especially to Paschal Coyle and John Carr for supervising my research during my stay. I enjoyed a lot working with the instrumentation line and testing the time calibration software in the dark room.

Thank you to all my colleagues and friends at Nikhef for your help, your support and most of all for your good company! Since I joined the ANTARES group, it has been changing over time and I would like to thank each one of you: Garmt, Aart, Bram, Mieke and the new members Jelena, Salvatore, Ana and Patrick. A big hug especially for Gordon, Guus, Eleonora and Dimitris. I wish you all the best and good courage with finishing your PhD-theses! Ronald alias “Mister Wolf”, my officemate, thank you for always “solving my problems” and being such a kind friend. Do not worry, I never was “angry”. I just wanted you

to give me some more MNM's [21]!

Groetjes and tanti bacci to my dear housemates Maaïke and Jacopo. I had the best of time with you and our friends in Amsterdam. I already miss the fabulous pasta dishes of Ristorante La Maison (and La Trattoria di Angelo of course!), the nights of MMORPGs playing, the Fridays at Melkweg, the salsa dancing at Cantinero... and so many more memories!

Miruna and Bram, thank you so much for always being there for me, especially during the last months of my PhD. You really are the dearest of friends.

Je ne saurai terminer sans remercier mes parents et mon frère, Anthony. Aussi loin que mes souvenirs remontent, j'ai toujours voulu devenir astrophysicienne, et c'est grâce à vous si aujourd'hui mon rêve se réalise. Vous m'avez donné le courage et la force d'arriver jusqu'au bout, de croire en moi quoi qu'il arrive. Je vous aime!

My last thought goes to you Petter. You have supported me, encouraged me and comforted me in the most difficult moments, even though I seemed more like a troll than a Swedish alva sometimes. I would have never made it without you. You mean everything to me. Je t'aime plus que tout!

Even though my doctorate has come to an end, I will always keep the Netherlands in my heart. I could thus not end these acknowledgements without this final word: bedankt!

# List of Figures

1	The measured cosmic ray spectrum between $10^{13}$ and $10^{21}$ eV. . . .	3
2	A Hillas plot. . . . .	4
3	The measured cosmic ray energy spectrum between $10^{18}$ eV and $10^{21}$ eV . . . . .	6
1.1	The ANTARES collaboration . . . . .	12
1.2	The Cherenkov effect. . . . .	14
1.3	Sketch of the ANTARES telescope. . . . .	16
1.4	A storey of the ANTARES telescope. . . . .	18
1.5	The ANTARES optical module (OM). . . . .	19
1.6	The Prototype Sector Line (PSL). . . . .	22
1.7	The Mini Instrumentation Line (MIL). . . . .	23
1.8	The Mini Instrumentation Line with one Optical Module (MILOM). . . . .	25
1.9	Downward-going muon event reconstructed using Line 1. . . . .	26
1.10	Sensitivity to point-like neutrino sources with ANTARES 5-Line data. . . . .	27
2.1	Distribution of measured time differences from OMs of the MILOM and the Led Beacon used as reference. . . . .	36
2.2	Raw and Integrated TVC spectra. . . . .	37
2.3	<i>Correlations between ARS time stamp (TS) and Time to Voltage Converter (TVC). . . . .</i>	38
2.4	Time stability of the dynamic ranges of the ARS TVC. . . . .	39
2.5	<i>Diagram showing the data flow between the different modules of PhAntOM. . . . .</i>	40
2.6	<i>Sample picture of the ANTARES Histogram Presenter window. . . . .</i>	42
3.1	Neutrino (or anti-neutrino) deep inelastic scattering (DIS) event . .	48
3.2	<i>Density profile of the Earth as a function of the distance from the center of the Earth. . . . .</i>	49
3.3	Upward-going muon neutrino energy spectrum simulated with GENHEN. . . . .	53
3.4	Telescope geometry as defined in GENHEN. . . . .	55
3.5	Upward-going muon neutrino energy spectrum generated using ANIS. . . . .	60

## LIST OF FIGURES

3.6	Differential neutrino-nucleon cross sections used by ANIS . . . . .	62
3.7	Telescope geometry as defined in ANIS. . . . .	63
3.8	Telescope geometry as defined in MMC. . . . .	66
3.9	Comparison of the lepton propagators MMC and MUM. . . . .	67
3.10	Comparison of the CTEQ6 and the parametrization used in ANIS for neutrino-nucleon cross sections. . . . .	68
3.11	Comparison of upward-going muon neutrino rates simulated with GENHEN and ANIS, assuming a diffuse AGN-like spectrum. . . .	70
3.12	Comparison of atmospheric muon neutrino rates simulated with GENHEN and ANIS. . . . .	71
4.1	Model predictions and measurements of the group velocity of light in sea water at the ANTARES site . . . . .	80
4.2	Representative geometry for tracking the photons in SIRENE. . . .	82
4.3	Coordinates used to describe the detection of Cherenkov light in SIRENE. . . . .	83
4.4	Distribution of the time residuals simulated with SIRENE. . . . .	86
4.5	Distribution of the number of detected Cherenkov photons, simu- lated with SIRENE. . . . .	89
4.6	Distribution of the number of detected Cherenkov photons from electromagnetic showers and muons as a function of the muon en- ergy. . . . .	90
4.7	Distribution of the time residuals between the digitized signal (sim- ulated with SIRENE) and the predicted hit time. . . . .	91
4.8	Comparison of the muon energy distributions simulated with SIRENE and KM3. . . . .	93
4.9	Comparison of the time residual distributions simulated with SIRENE and KM3. . . . .	94
4.10	Distribution of the reconstruction error on the direction of the muon determined using AartStrategy. . . . .	102
4.11	Distribution of the reconstructed error on the position using Aart- Strategy. . . . .	103
4.12	Distribution of the reconstructed error on the muon direction using AartStrategy . . . . .	104
4.13	Distribution of the reconstructed error on the muon direction using Scanfit for events simulated with SIRENE. . . . .	106
4.14	Distribution of the reconstructed muon energy as a function of the true energy for events simulated with SIRENE. . . . .	107
5.1	Distribution of the cosine of the zenith angle for high energy events simulated with ANIS. . . . .	111



## LIST OF FIGURES

5.2	Energy distribution of downward-going ultra-high energy muons simulated using ANIS and atmospheric muons simulated with MUPAGE. . . . .	112
5.3	Distribution of the cosine of the zenith angle for atmospheric muons simulated with MUPAGE. . . . .	113
5.4	Distribution of the total charge of the hits as a function of the true muon energy for downward-going ultra high energy events simulated with SIRENE. . . . .	115
5.5	Energy distribution at the trigger level of ultra-high energy muons simulated with SIRENE and atmospheric muons simulated with MUPAGE. . . . .	117
5.6	Distribution of the total charge of the hits as a function of the muon zenith angle for downward-going ultra high energy muons simulated with SIRENE and atmospheric muons simulated with MUPAGE. . . . .	119
5.7	Distribution of the cosine of the zenith angle for downward-going ultra high energy muons and atmospheric muons at the trigger level.	120
5.8	Distribution of the total charge of the hits induced by downward-going high energy muons and atmospheric muons at the trigger level. . . . .	120
5.9	Distributions of the cosine of the zenith angle and the total charge of the hits for downward-going ultra high energy muons and atmospheric muons after applying cuts on the muon direction and the estimated total charge of the hits. . . . .	121
5.10	Integrated distribution of the cosine of the zenith angle for the flux shown in Figure 5.9. . . . .	123
5.11	Integrated distribution of the estimated charge of the hits for the flux shown in Figure 5.9. . . . .	124
5.12	Model rejection factor for the diffuse flux of downward-going UHE neutrinos as a function of the muon zenith angle and total charge cut variables. . . . .	125
5.13	Distributions of the cosine of the zenith angle and the total charge of the hits for downward-going ultra high energy muons and atmospheric muons, using optimised cuts. . . . .	126
5.14	Comparison of the ANTARES upper limits at ultra high energies with various experimental bounds on diffuse muon neutrino fluxes.	128
5.15	Muon neutrino effective areas for UHE events in ANTARES. . . . .	130
B.1	Final energy distribution of 100 TeV muons propagated through 300 meters of ANTARES Water, simulated with MMC. . . . .	143
B.2	Same as the right part of Figure B.1 but using the continuous randomisation option. . . . .	144

*LIST OF FIGURES*

C.1 Schematic overview of the classes of the detector simulation program SIRENE. . . . .	146
--	-----

# List of Tables

3.1	CPU usage of ANIS and GENHEN . . . . .	69
B.1	Chemical composition of the sea water at the ANTARES site. . . . .	142

## *LIST OF TABLES*

# Bibliography

- [1] A.A. Penzias and R.W. Wilson. *Astrophys. J.*, 142:419, 1965.
- [2] J. Learned and K. Mannheim. High-energy neutrino astrophysics. *Annual Review Nuclear Particle Science*, 50:679–749, 2000.
- [3] C. AMSler et al. *Physics Letters B*, 667:1, 2008.
- [4] E. Fermi. *Phys. Rev.*, 75:1169, 1949.
- [5] A.M. Hillas. *Ann. Rev. Astron. Astrophys.*, 22:425, 1984.
- [6] D.J. Bird et al. *Astrophys. J.*, 424:491, 1994.
- [7] J. Abraham et al. Observation of the suppression of the flux of cosmic rays above  $4 \times 10^{19}$  ev. *Phys. Rev. Lett.*, 101:061101, 2008.
- [8] D.F. Torres and L.A. Anchordoqui. *Rept. Prog. Phys.*, 67:16631730, 2004. astro-ph/0402371.
- [9] K. Greisen. *Phys. Rev. Lett.*, 16:748, 1966.
- [10] G.T. Zatsepin and V.A. Kuzmin. *Pisma Zh. Eksp. Teor. Fiz.*, 4:114, 1966.
- [11] R.U. Abbasi et al. *Phys. Rev. Lett.*, 100:101101, 2008.
- [12] M. Takeda et al. *Astropart. Phys.*, 19:447, 2003.
- [13] J. Abraham et al. Correlation of the highest-energy cosmic rays with the positions of nearby active galactic nuclei. *Astropart. Phys.*, 29:188–204, 2008.
- [14] M. Drees. The top-down interpretation of ultra-high energy cosmic rays. *J. Phys. Soc. Jpn.*, 77:16–18, 2008. Suppl. B.
- [15] Shinozaki, 2006. talk presented at GZK40, Moscow.
- [16] Q.R. Ahmad et al. Direct evidence for neutrino flavor transformation from neutral-current interactions in the Sudbury neutrino observatory. *Phys. Rev. Lett.*, 89:011301, 2002.

## BIBLIOGRAPHY

- [17] M.A. Markov. In *Proc. Annual International Conference on High Energy Physics*, 1960. Proceedings of Annual International Conference on High Energy Physics, Manchester.
- [18] P. Amram et al. Sedimentation and fouling of optical surface at the ANTARES site. *Astropart. Phys.*, 19:253–267, 2003.
- [19] J.A. Aguilar et al. First results of the instrumentation line for the deep-sea ANTARES neutrino telescope. *Astropart. Phys.*, 26:314, 2006.
- [20] M. Ageron et al. Studies of a full scale mechanical prototype line for the ANTARES neutrino telescope and test of a prototype instrument for deep-sea acoustic noise measurements. *Nuclear Instruments and Methods in Physics Research A*, 581:695–708, 2007.
- [21] R. Bruijn. *The ANTARES Neutrino Telescope: Performance Studies and Analysis of First Data*. PhD thesis, Universiteit van Amsterdam, Amsterdam, the Netherlands, March 2007.
- [22] M. Ageron et al. Performance of the first ANTARES detector line, 2008. arXiv:0812.2095.
- [23] J.A. Aguilar et al. Sensitivity to point-like neutrino sources with ANTARES 5-line data, 2008. ANTARES public plot, ANTAPLOT-PHYS-2008-019.
- [24] B. van Rens. *Detection of magnetic monopoles below the Cerenkov limit*. PhD thesis, Universiteit van Amsterdam, Amsterdam, the Netherlands, July 2006.
- [25] M. de Jong. The ANTARES trigger software. ANTARES internal note, ANTARES-Soft/2004-001.
- [26] M. de Jong. The ANTARES data format. ANTARES internal note, ANTARES-Soft/2004-006.
- [27] J.A. Aguilar. *Analysis of the optical beacon system and search for point-like sources in the ANTARES neutrino telescope*. PhD thesis, Universidad de Valencia, Valencia, Spain, December 2007.
- [28] <http://root.cern.ch>. The ROOT Users Guide is available from the ROOT homepage.
- [29] C. Colnard. Time calibration using the optical beacon trigger. ANTARES internal note, ANTARES-Cali/2005-004.
- [30] C. Colnard. The ars tvc calibration. ANTARES internal note, ANTARES-Cali/2005-003.

- [31] C. Colnard. Physics data of ANTARES online monitoring phantom, installation and users manual. ANTARES Internal note, ANTARES-Soft/2004-005.
- [32] C. Colnard. The ANTARES histogram presenter: installation and users manual. ANTARES Internal note, ANTARES-Soft/2004-003.
- [33] Eadie et al. *Statistical Methods in Experimental Physics*. Elsevier Science Ltd, 1983. 2nd Repr edition.
- [34] R. Gandhi et al. Ultrahigh-energy neutrino interactions, 1995. hep-ph/9512364.
- [35] S.L. Glashow. *Phys. Rev.*, 118:316 – 317, 1960.
- [36] S. Jadach et al. *Comput. Phys. Commun.*, 64:275, 1991.
- [37] H. Athar et al. *Phys. Rev. D.*, 62:103007, 2000.
- [38] R. Gandhi et al. Ultrahigh-energy neutrino interactions. *Astropart. Phys.*, 5:81–110, 1996.
- [39] R. Gandhi. Ultra-high energy neutrinos: A review of theoretical and phenomenological issues, 2001. hep-ph/0011176.
- [40] A.M. Dziewonski and D.L. Anderson. *Phys. Earth Planet. Interior*, 25:297, 1981.
- [41] G. Sterman et al. Handbook of Perturbative QCD. *Review of Modern Physics*, 67:157–248, 1995.
- [42] J. Pumplin et al. New generation of parton distribution functions with uncertainties from qcd analysis. *Journal of High Energy Physics*, 012:0207, 2002.
- [43] A.D. Martin et al. Parton distributions for the LHC, 2009. arXiv:0901.0002.
- [44] J. Pumplin et al. New Generation of Parton Distribution with Uncertainties from Global QCD Analysis, 2002. hep-ph/0201195.
- [45] ZEUS collaboration. A ZEUS next-to-leading-order QCD analysis of data on deep inelastic scattering. *Phys. Rev. D*, 67:012007, 2003.
- [46] ZEUS collaboration. An NLO QCD analysis of inclusive cross-section and jet-production data from the ZEUS experiment. *Eur. Phys. J. C.*, 42:1–16, 2005.
- [47] C. Carloganu. Muon Interactions at High Energies. ANTARES internal note, ANTARES-PHYS-98-013.

## BIBLIOGRAPHY

- [48] W.M. Yao et al. *Journal of Physics G*, 33:1, 2006.
- [49] I.A. Sokalski et al. Parametrization of atmospheric muon angular flux underwater. *Phys. Rev. D*, 64:014016, 2001.
- [50] D. Chirkin and W. Rhode. Propagating leptons through matter with muon monte carlo (mmc). arXiv:hep-ph/0407075v2.
- [51] L.B. Bezrukov and E.V. Bugaev. *Sov. J. Nucl. Phys.*, 32:847, 1980.
- [52] H. Olsen and L.C. Maximon. Photon and electron polarization in high-energy bremsstrahlung and pair production with screening. *Physical Review*, 114:887–904, 1959.
- [53] J. Allison et al. Geant4 developments and applications. *IEEE Transactions on Nuclear Science*, 53 No. 1:270–278, 2006.
- [54] A. Labbate et al. Genhen v6: ANTARES neutrino generator extension to all neutrino flavors and inclusion of propagation through the earth. ANTARES internal note, ANTARES-SOFT-2004-010.
- [55] David J.L. Bailey. PhD thesis, Wolfson College, Oxford, UK., 2002.
- [56] A. Kouchner. *Possibilité d’observation, par le télescope ANTARES, de neutrinos de haute énergie associés aux sursauts gamma et validation des techniques de détection à l’aide d’un prototype*. PhD thesis, Université Paris VII, Paris, France, April 2001.
- [57] L. Nyhoff. *FORTRAN 90 for Engineers and Scientists*. Prentice Hall, 1996.
- [58] S. Agostinelli et al. Geant4 - a simulation toolkit. *Nuclear Instruments and Methods A*, 506:250–303, 2003.
- [59] G. Ingelman et al. Lepto 6.5: A monte carlo generator for deep inelastic lepton-nucleon scattering. *Computer Physics Communications*, 101:108–134, 1997.
- [60] G. Barr. PhD thesis, Oxford University, Oxford, UK., 1987.
- [61] H. Plothow-Besch. Pdflib: Proton, pion and photon parton density functions of the nucleus user’s manual, 2000. CERN computer program library entry W5051.
- [62] K. Kuzmin et al. Genhenv6r3: implementation of the glashow resonance and of the music transport code. ANTARES internal note, ANTARES-SOFT-2004-012.



- [63] David J.L. Bailey. Genhen v5r1: Software documentation. ANTARES internal note, ANTARES-SOFT-2002-004.
- [64] B.R. Martin and G. Shaw. *Particle Physics*. Wiley, 1997. Second Edition.
- [65] J. Brunner. Updated tag list for the new ANTARES event format. ANTARES internal note, ANTARES-SOFT-1999-003.
- [66] T. Montaruli and A. Romeyer. Conventional and prompt atmospheric neutrino fluxes. ANTARES internal note, ANTARES-PHYS-2001-015.
- [67] David J.L. Bailey. Genhen v3r1: Further optimisation for large energy ranges. ANTARES internal note, ANTARES-SOFT-2000-6.
- [68] A. Heijboer. *Track Reconstruction and Point Source Searches with ANTARES*. PhD thesis, Universiteit van Amsterdam, Amsterdam, the Netherlands, June 2004.
- [69] P. Lipari and T. Stanev. *Phys. Rev. D*, 44:3543, 1991.
- [70] P. Antonioli et al. A three-dimensional code for muon propagation through the rock: Music, 1997. hep-ph/9705408.
- [71] I. Sokalski. Accuracy of the muon transportation: Propmu, music, mum. ANTARES internal note, ANTARES-Soft-2001-005.
- [72] J. Breitweg et al. *Eur. Phys. J. C*, 7:609, 1999.
- [73] Yu. M. Andreev et al. *Phys.Atom.Nucl.*, 57:2066, 1994.
- [74] A. Gazizov and M.Kowalski. High energy neutrino generator for neutrino telescopes. 2003. Proceedings of the 28th International Cosmic Ray Conference, Tsukuba, Japan.
- [75] M. Dobbs and J.B. Hansen. *Comput. Phys. Commun.*, 134:41, 2001.
- [76] A.Z. Gazizov and S.I. Yanush. *Phys. Rev. D*, 65:093003, 2002.
- [77] A. Donnachie and P.V. Landshoff. *Phys. Lett.B*, 518:63–71, 2001.
- [78] P. Lipari. *Astropart. Phys.*, 1:195, 1993.
- [79] U. Katz. KM3NeT: Towards a km3 mediterranean neutrino telescope. 2005. Proceedings of the VLVnT2 Workshop, Catania, Sicilie.
- [80] Y.S. Tsai. *Rev. Mod. Phys.*, 49:421, 1977.
- [81] B.D. Hartmann. *Reconstruction of Neutrino-induced Hadronic and Electromagnetic Showers with the ANTARES Experiment*. PhD thesis, Universitat Erlangen-Nurnberg, Erlangen, Germany, June 2006.

## BIBLIOGRAPHY

- [82] J. Brunner. Cherenkov light from the electromagnetic and hadronic showers. ANTARES internal note, ANTARES-Software-2002-015.
- [83] R. Mirani. Parametrisation of em-showers in the ANTARES detector-volume. Master's thesis, Universiteit van Amsterdam, 2002.
- [84] J. Brunner. Geasim. <http://antares.in2p3.fr/internal/software/geasim.html>.
- [85] S. Bottai and L. Perrone. Simulation of the muons propagation for geant3. *Nucl.Instrum.Meth. A*, 459:319–325, 2001.
- [86] J.A. Aguillar et al. Transmission of light in deep sea water at the site of the ANTARES neutrino telescope. *Astropart. Phys.*, 23:131–155, 2005.
- [87] X. Quan and E.S. Fry. *Applied Optics*, 34 Iss. 18:3477–3480, 1995.
- [88] L.A. Kuzmichev. On the velocity of light signals in the deep underwater neutrino experiments, 2000. hep-ex/0005036.
- [89] F. Hubaut. *Optimisation et caractérisation des performances d'un télescope sous-marin à neutrinos pour le projet ANTARES*. PhD thesis, Université de la Méditerranée, Marseille, France, April 1999.
- [90] S. Navas and L. Thompson. Km3 user guide and reference manual. ANTARES internal note, ANTARES-SOFT-2002-006.
- [91] P. Amram et al. The ANTARES optical module. *Nucl.Instr. and Methods A*, 484:369, 2002.
- [92] P. Kooijman. On the angular acceptance of the optical module. ANTARES internal note, ANTARES-PHYS-2007-002.
- [93] J.A. Aguilar et al. Study of large hemispherical photomultiplier tubes for the ANTARES neutrino telescope. *Nuclear Instruments and Methods in Physics Research A*, 555:132–141, 2005.
- [94] J.D. Zornoza. Effect of the ar saturation on the energy reconstruction. ANTARES internal note, ANTARES-SOFT-2003-003.
- [95] W.J. Metzger. *Statistical methods in data analysis*. Katholieke Universiteit Nijmegen, Nijmegen, The Netherlands, 2001. HEN-343.
- [96] M. de Jong. Partial linearisation of the track fit problem. ANTARES internal note, ANTARES-Soft/2007-001.
- [97] A. Romeyer. *Etude de la sensibilité du détecteur ANTARES à un flux diffus de neutrinos cosmiques de haute énergie*. PhD thesis, Université Paris VII, Paris, France, April 2003.

- [98] A.Oppelt. *Etude de la résolution angulaire du télescope à neutrinos ANTARES*. PhD thesis, Université de la Méditerranée, Aix-Marseille II, France, April 2001.
- [99] J.D. Zornoza. *Sensitivity to diffuse fluxes and energy spectrum reconstruction in the ANTARES neutrino telescope*. PhD thesis, Universidad de Valencia, Valencia, Spain, January 2005.
- [100] G. Carminati et al. Mupage: A muon generator for parametric formulas. ANTARES internal note, ANTARES-Phys/2006-003.
- [101] G. Battistoni et al. *Astropart. Phys.*, 3:1575, 1995.
- [102] J. Ranft. *Phys. Rev. D*, 51:64, 1995.
- [103] J. Horandel. *Astrop. Phys.*, 19:193, 2003.
- [104] S.P. Ahlen et al. *Nuclear Physics B*, 370:432, 1992.
- [105] G.J. Feldman and R.D. Cousins. *Phys. Rev. D*, 57:3873–3889, 1998.
- [106] G.C. Hill and K. Rawlins. Unbiased cut selection for optimal upper limits in neutrino detectors: the model rejection potential technique, 2002. astro-ph/0209350.
- [107] E. Waxman and J. Bahcall. *Phys. Rev. D*, 59:023002, 1999.
- [108] K. Hoshina. Diffuse high-energy neutrino searches in amanda-ii and icecube: Results and future prospects. In *Journal of Physics: Conference Series* 120 (2008) 062007. Proceedings of TAUP 2007.
- [109] M. Honda and T.K. Gaisser. *Ann. Rev. Nucl. Part. Sci.*, 52:153, 2002.
- [110] M. Ackermann et al. Flux limits on ultra high energy neutrinos with amanda-b10. *Astropart. Phys.*, 22:339–353, 2005.
- [111] M. Ackermann et al. Search for ultra-high energy neutrinos with amanda-ii. *Astrophysical Journal*, 675:1014–1024, 2008.
- [112] I. Kravchenko et al. Rice limits on the diffuse ultrahigh energy neutrino flux. *Physics Review D*, 73:082002, 2006.
- [113] V. Aynutdinov et al. Status and new results from the baikal detector. Proceedings of Ninth Int. Conf. on Topics in Astroparticle and Underground Physics (TAUP 2005).
- [114] J. Arhens et al. Sensitivity of the icecube detector to astrophysical sources of high energy muon neutrinos. *Astropart. Phys.*, 20:507–532, 2004.

## BIBLIOGRAPHY

- [115] A. Okada. *Astropart. Phys.*, 2:393, 1994.
- [116] B. Stroustrup. *C++ Programming Language, The (3rd Edition)*. Addison-Wesley Professional, 1997.
- [117] F. Cassol. Gendet 1.0: a program to generate detector files. ANTARES internal note, ANTARES-SOFT-1999-007.